DISSERTATION
SUBMITTED TO THE
COMBINED FACULTIES FOR THE
NATURAL SCIENCES AND MATHEMATICS OF THE
RUPERTO-CAROLA UNIVERSITY OF HEIDELBERG, GERMANY
FOR THE DEGREE OF
DOCTOR OF NATURAL SCIENCES

Put forward by

Rohin Thampilali Narayan
Born in: Calicut, India

Oral examination: 5th November 2014

Feasibility Study for the Measurement of $pp \rightarrow Z(e^+e^-) + b\bar{b}$ in Proton-Proton Collisions at $\sqrt{s} = 8\,\text{TeV}$ using a Soft Electron Tagger with the ATLAS Experiment at LHC

Referees: Prof. Dr. André Schöning
Prof. Dr. Hans-Christian Schultz-Coulon

Abstract

In this thesis, data from proton-proton collisions at a center of mass energy of $\sqrt{s} = 7\,\text{TeV}$ and $\sqrt{s} = 8\,\text{TeV}$ delivered by the Large Hadron Collider and recorded by the ATLAS experiment in the year 2011 and 2012 are used to develop a timing monitoring framework for the ATLAS Level-1 Calorimeter trigger system, to develop a soft electron tagger and carry out a feasibility study for the measurement of $pp \to Z(e^+e^-) + b\bar{b}$ process respectively.

The Level-1 Calorimeter trigger is a hardware based trigger with a decision latency of up to 2.5 μs. It performs bunch-crossing identification and coarse energy measurement to make a trigger decision. These operations depend on precise timing adjustments which are done to achieve a correct sampling of the signal peaks. For an energy measurement of better than 2 % in the trigger, the peak has to be sampled within ±5 ns. Software has been written to monitor the signal peak sampling offsets for all 7168 channels. This was done by measuring the signal peak location to the nanosecond level and monitoring this value as a function of time to verify the signal stability.

Conventional jet based b-tagging methods introduce jet energy scale uncertainties in measurements. Alternatively electrons from semileptonic decays of b-quarks can be used for b-tagging, avoiding these uncertainties. The new soft electron tagger developed in this work extensively uses the precision capabilities of the ATLAS Inner Detector and electromagnetic calorimeter system. Signal and background sources identified with Monte Carlo samples were trained with a multivariate boosted decision tree classifier, through supervised learning. The electron identification responses of signal samples were verified by statistically extracting signal distributions from $J/\psi \to e^+e^-$ and $Z \to e^+e^-$ enriched data samples. Efficiency and systematics of the new soft electron tagger were also estimated using $J/\psi \to e^+e^-$ enriched data samples.

A feasibility study for the measurement of $pp \to Z(e^+e^-) + b\bar{b}$ process using the soft electron tagger also has been carried out. Along with the newly developed soft electron tagger, charge combinations as well as kinematic distributions of soft-electron pairs have been used to create regions which are enhanced in the signal with a relatively large signal to background ratio.

Zusammenfassung

Die vorliegende Arbeit beschreibt zum einen die Entwicklung eines Timing Überwachungs Frameworks für den Level-1-Kalorimetertrigger des ATLAS-Experiments, sowie Studien zur Durchführbarkeit einer Messung des Prozesses $pp \to Z(e^+e^-) + b^+b^-$ mit Hilfe eines Taggers für Elektronen mit niedrigem Transversalimpuls aus semileptonischen Zerfällen der b-Quarks. Dazu werden Daten des ATLAS-Experiments ausgewertet, die bei Proton-Proton-Kollisionen mit einer Schwerpunktsenergie von $\sqrt{s} = 7\,\mathrm{TeV}$ und $\sqrt{s} = 8\,\mathrm{TeV}$ in den Jahren 2011 und 2012 am LHC aufgenommen wurden.

Der Level-1-Kalorimetertrigger ist ein Hardwaretrigger mit einer Latenz von 2.5 µs. Bei jeder Strahlkreuzung wird eine grobe Energiemessung durchgeführt, welche zur Triggerentscheidung beiträgt. Dazu ist es wichtig, dass das Timing des Triggers sehr exakt ist, da ansonsten nicht das Maximum der Energie berücksichtigt wird. Um eine Genauigkeit von 2% in der Energie zu erreichen, muss die Energiespitze mit einer Genauigkeit von ±5 ns gesamplet werden. Die Kalibration der Verzögerungen aller 7168 Kalorimetertrigger-Kanäle muss daher auf Nanosekundenniveau überwacht werden, um mögliche Zeitliche Instabilitäten zu erkennen.

Konventionelle Methoden des b-Taggings leiden unter der Unsicherheit der Jet-Energiebestimmung. Ein in dieser Arbeit neu entwickelter Elektronentagger wird benutzt um den semileptonischen Zerfall von b-Quarks zu erkennen. Dazu wird ausgenutzt, dass sowohl der Spurdetektor wie auch das elektromagnetische Kalorimeter des ATLAS-Detektors mit hoher Präzision kalibriert werden können. Mit Hilfe von für Signal- und Untergrundprozesse charakteristischen Verteilungen, z.Bsp. des elektromagnetischen Schauers, wird ein Boosted-Decision-Tree aufgebaut. Die dazu verwendeten Monte-Carlo-Simulationen werden mit Elektronen aus J/Ψ und Z-Zerfällen aus Daten validiert. Weiterhin werden so Effizienzen und systematische Unsicherheiten des Elektronentaggers abgeschätzt.

Die Durchführbarkeit einer Messung des Prozesses $pp \to Z(e^+e^-) + b\bar{b}$ mit Hilfe des Elektronentaggers wurde untersucht. Zusammen mit der Entscheidung des Taggers erlauben Schnitte auf die Kinematiken und Kombinationen der Ladungszahlen der gefundenen Elektronenpaare Signalereignisse verstärkt zu selektieren, was zu einem verbesserten Signal-zu-Untergrund-Verhältnis führt.

Contents

Appendices

Chapter 1

Introduction

Perhaps one of the most distinguishing feature of our species is its ability to think about the origin of the Universe, its constituents structure and even the existence of ourselves. Philosophers across civilizations have pondered about these questions for a couple of millenia, and tried to give various answers. However the tradition of exploring and understanding the nature has been correctly formulated only pretty recently in the history of human civlization. It looks like the correct epistemic method to attack these questions is by using the *scientific method*. Theoretical models validated by experiments started revealing a rich and seemingly ordered structure of the universe we are living in.

Guided by mathematical principles of symmetry and conservatively probing the validity of the theoritical models constructed from those symmetries, an approach known as *Radical Conservatism* [1], we have been probing the fundamental constituents of matter for a better part of the last century. Following the footsteps of Rutherford who pioneered scattering experiments which revealed the structure of atomic nuclei, many scattering experiments have been carried out with increasing energies to probe deeper into the structure of matter. These experiments reveal a rich structure described by a theory called the Standard Model of particle physics. It describes all the known interactions except gravity. The experiments at the Large Hadron Collider (LHC) are the most recent entries into the list of scattering experiments which collide proton beams at the highest energies in a controlled environment.

However the Standard Model is far from being complete. There are certain problems within the Standard Model and the theory breaks when extrapolated to a higher energy scale. Thus there is enough reason to believe that the Standard Model is an effective theory valid at a low energy approximation. Many new physics models have been proposed to extend the Standard Model. Most of these models predict the production of particles that are heavier than the most massive Standard Model particles. If these new particles are produced during collisions at LHC, they will decay into known Standard Model particles. Some of the signatures for these new particle decays looks like the known standard model decays. These kinds of processes are called background. A very good understanding of these background processes is required to increase the chances of observing New Physics.

Of particular interest is the Standard Model process with an electroweak neutral gauge boson and two b-quarks in the final state. This process is sensitive to the gluons distributions in the colliding particles, the protons. A precise measurement of this processes constraints the uncertainties in gluon distributions. A stream of collimated particles in the detector, also called b-jets is the signature for the production of b-quarks. The standard method of identifying these objects introduce significant uncertainties like the b-jet identification and jet energy scale uncertainties. Alternatively, it is also possible to identify the b-quarks through the semileptonic decay of the B-hadrons. This thesis focuses on developing a *semileptonic* b-tagger to identify b-quark final states. The focus is on selecting event topologies in which the electroweak neutral gauge boson decays into isolated electron positron pairs and the both b-quarks in the final state decays semileptonically into another not so well isolated electron positron pair.

The thesis is structured as follows. In Chapter 2 & 3, the theoretical background required for this work is described. In chapter 4 & 5, a brief description of the accelerator as well as the ATLAS detector and trigger is given. Chapter 6 describe the standard electron reconstruction and identification in ATLAS. Chapter 7 describes the method of the new soft electron tagger. The variables used in the tagger has been validated in data using tag & probe and sideband subtraction methods. The efficiency and systematics of the tagger also has been estimated. Finally chapter 8 describes the feasibility for the measurement of the associated production of electroweak neutral gauge boson and two b-quarks through a fully leptonic method.

Chapter 2

The Standard Model of Particle Physics

Our current understanding of particle physics is based on a theory called Standard Model [2] [3] which explains various interactions observed in nature. In this chapter a brief review of the Standard Model is given.

The Standard Model describes most of the known interactions in the universe. It describes the electromagnetic interactions which we directly experience through our senses, Weak interactions which are responsible for the decay of radioactive nuclei, It also describes the Strong interactions which are responsible for nuclear interactions. The Standard model evolved through a series of strides in experimental break throughs and theoretical insights. Even though the best known theory of gravitation, the general theory of relativity has not been successfully incorporated in the Standard Model, it has been fairly successful till date in describing particle intractions.

Particles which obey Bose-Einstein statistics (bosons) and Fermi-Dirac statistics (Fermions), constitute the Standard Model. The integer spin bosons mediate particle interactions, while the spin 1/2 fermions makes up the matter. The fermions in the Standard Model are classified into two categories, the quarks and the leptons. Quarks can exist only in bound states while the leptons can exist freely. The particles in the Standard Model are arranged in three generations. All the stable atoms and molecules that we see around are made up of the first generation particles in the Standard Model.

The fermions in the Standard Model interact with each other via exchanging force particles, the gauge bosons. Each interaction is mediated through the exchange of distinct gauge boson.

All electrically charged particles interact via the electromagnetic interaction by exchanging force particle, the photon. The photon is a spin 1 massless boson with no electric charge. Since the photon is electrically neutral there are no self interactions and since it is massless the range of electromagnetic force is infinite. At the quantum level, the electromagnetic interaction is described by a theory called Quantum Electrodynamics.

Quarks carry a so called “color charge” and interact via Strong interaction. Strong interactions are mediated by force carriers called gluons. The gluons themselves carry color charge and hence self interactions are possible. Even though the force particle is massless, the range of strong force is very limited due to reasons that will be explained in the following section. The strong force is the strongest of all known interactions. It is responsible for binding the quarks inside the atomic nuclei.

The weak interaction is weaker than strong and electromagnetic interactions. It acts on all the particles in the Standard Model. The force carriers, the $W^{\pm}$ and the Z boson are massive and hence the range of the force is limited. The weak force is responsible for radioactive decay of atomic nuclei.

2.1 Quarks and Leptons

Quarks are the fundamental particles which undergoe strong interactions. In the standard model there are 6 of them arranged in 3 generations. The first generation consists of up and down quarks. The up quark has a fractional electric charge of +2/3e and the down quark has a charge of -1/3e ("e" is the charge of the electron 1.6021×10^{-19} C). Similarly the other up type quarks, the top and charm have a charge +2/3e and the other down type quarks, strange and bottom have a charge -1/3e each.

The leptons are also organized into three families. There are six types of leptons electrons, muons, tauons and their respective neutrinos (electron neutrino, muon neutrino, tau neutrino).

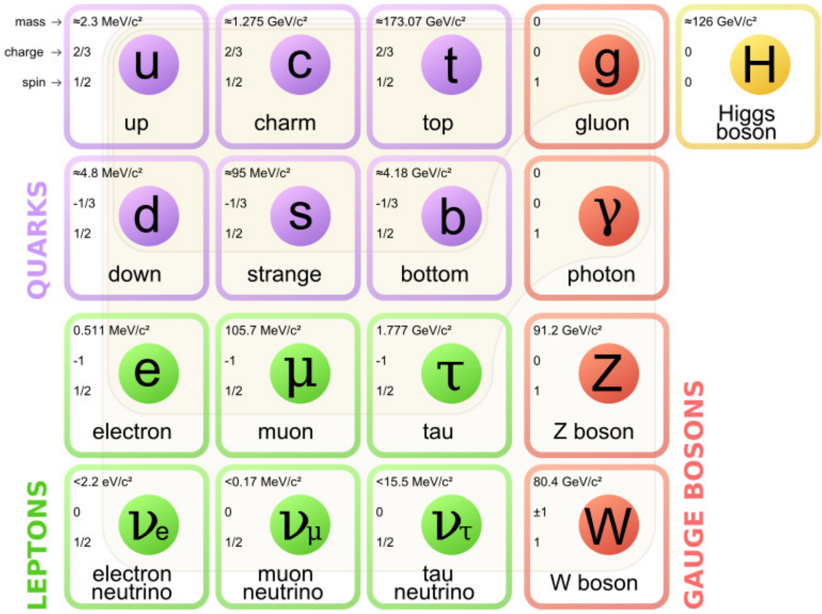

Figure 2.1: Fundamental particles in the standard model. The spin quantum number, electric charge of the particles are listed with their masses [4].

The generation structure of quarks and leptons is shown in Figure 2.1. The first generation particles like up, down quarks and electrons form the ordinary matter. The higher generation particles are not stable and they decay into the first generation particles. All the particles listed in Figure 2.1 also have their anti particles. These particles differ from their particle counterparts only in their quantum numbers.

Quarks and anti-quarks do not exist free in nature and they only exist in bound states with another one or two quarks. Three quark bound states are called baryons. Protons (uud) and neutrons (ddu) are typical examples. Two quark bound states are called mesons. Particles like π^+ (u$\bar{\text{d}}$) and its anti particle π^- ($\bar{\text{u}}$d) are mesons.

In the following section we briefly review the mathematical formalism of Standard Model. The review is based on [5].

2.2 Gauge Theories

In classical mechanics the dynamics of a system of interacting particles can be described using the Lagrangian of the system. The Lagrangian L is defined as

$$L = T - V, \tag{2.1}$$

where T is the kinetic energy and V is the potential energy of the system.

The evolution of the system is described by the Euler-Lagrange equation

$$\frac{d}{dt}\left(\frac{\partial L}{\partial \dot{q}_i}\right) - \frac{\partial L}{\partial q_i} = 0, \tag{2.2}$$

where $\{q_i, \dot{q}_i\}$ are the generalized coordinates ($\dot{q}_i = dq_i/dt$). In quantum field theory, the discrete generalized co-ordinates are replaced with continuous systems, the fields $\phi \equiv \phi(\mathbf{x}, t)$. The Lagrangian becomes

$$L \equiv L(\phi, \frac{\partial \phi}{\partial x_\mu}, x_\mu), \tag{2.3}$$

where ϕ is the field.

It can be shown that the Dirac equation, the relativistic wave equation for a spin 1/2 particle, for instance the electron can be obtained by applying the following Lagrangian in the Euler-Lagrange equation.

$$L = i\psi\gamma_\mu\partial^\mu\psi - m\bar{\psi}\psi, \tag{2.4}$$

The electron is described by the complex field $\psi(x)$. Clearly the Lagrangian is invariant under the phase transformation

$$\psi(x) \rightarrow e^{i\alpha}\psi(x), \tag{2.5}$$

Transformations of these kind are called gauge transformations since the "gauge" of the system is changed in the operation. The set of all transformations of the kind $U(\alpha) \equiv e^{i\alpha}$, where α spans the set of all real numbers, forms a unitary Abelian group called U(1) group. By virtue of Noether's theorem it can be shown that such a gauge symmetry results in the conservation of electric charge. Thus the U(1) gauge symmetry of electromagnetic interactions conserves the electric charge.

However under a "local gauge transformation" where α depends on space-time co-ordinates,

$$\psi(x) \to e^{i\alpha(x)}\psi(x), \tag{2.6}$$

the Lagrangian is not an invariant. However nothing forbids the addition of extra terms to make the Lagrangian invariant. In case of the Lagrangian of Quantum Electrodynamics, these additional fields represent the photon field, the force carrier of the electromagnetic interaction.

Thus demanding a local gauge invariance generates the field particles of a given interaction.

2.2.1 Strong Interaction

Strong interaction is described by a gauge theory called quantum chromodynamics (QCD). The gauge group of the theory is $SU(3)_c$ (subscript 'c' denotes "color"). Since not all generators of the group commute with each other the group is non Abelian. QCD describes the bound states of quarks mediated by the massless field particles, ie. through gluon coupling to color charges. Unlike in QED the gauge boson also carries a color charge and hence gluon self interactions are possible. Three types of color charges exist, "red", "green" and "blue". Eight gluons are needed to maintain the local gauge invariance under $SU(3)$.

The strength of the strong force is expressed through the coupling α_s. The coupling increases as the distance between the interacting particles increases and decreases as the distance decreases similar to how a glue acts. Therefore the field particles of the interaction which is responsible for holding the nucleons together is called "gluon". This would mean that only colorless particles are observed in nature, a phenomena called "color confinement". Color confinement restricts the range of strong interaction to 10^{-15} m although the gauge boson of the interaction is massless.

At small distances of interacting quarks, the QCD coupling becomes small, a phenomena known as asymptotic freedom. This behaviour allows for the perturbative calculation of interactions at high energy scales or small length scales. The cut off scale at which the perturbative regime of QCD stops is called λ_{QCD} which is typically of the order of 200-300 MeV. Beyond this regime the quarks and gluons leave the quasi free regime to QCD bound states generally called hadrons. Perturbative QCD is not applicable in describing such systems.

2.2.2 Electroweak Interaction

The first hints of weak interaction came from the observation that lifetimes of pions and muons are longer than those particles which decay through electromagnetic or strong interactions. The Weak interactions are also responsible for the nuclear β-decay. Fermi theory of β-decay predicts the existence of a charge current responsible for the decay. This was experimentally verified through neutrino-electron scattering experiments. Later the Gargamelle experiment reported the existence of a weak neutral current [6] and this was also successfully incorporated into the theory.

The weak interaction is the only known interaction which can change the flavor of the quarks. It is also known to violate parity and the combined operation of charged conjugation and parity (CP). The gauge bosons of the theory are the heaviest compared to other known interactions, hence the range of the interaction is very small.

The weak interaction couples to two quantum numbers, weak isospin (I_W) and hypercharge (Y). Hyper charge is given by the Gellmann-Nishijima formula

$$Y = 2(Q - I_{w3}), \tag{2.7}$$

where I_{w3} is the third component of weak isospin and Q is the electric charge of the particle.

Left handed particles, that is particles which have negative chirality have $I_{w3} = 1/2$. In general these particles can be grouped into weak isosopin doublets $I_{w3} = \pm 1/2$. Right handed particles, which have positive helicity have $I_{w3} = 0$ and forms a singlet state and do not undergo weak interactions. Local gauge invariance under the $SU(2)_L$ symmetry group rotates a particle in isospin space and transforms it into its doublet partner.

In order to keep the weak Lagrangian invariant under $SU(2)_L$ three additional gauge fields are introduced in the Lagrangian, namely $\{W_1, W_2, W_3\}$. The physical field responsible for charge current interaction is a linear combination of the first two fields.

$$W^{\pm} = \frac{1}{\sqrt{2}}(W_{\mu}^{1} \mp iW_{\mu}^{2}), \tag{2.8}$$

An additional $U(1)_Y$ gauge transformation is introduced to explain the weak neutral current interaction. Now the Lagrangian has to be invariant under the combined transformation $SU(2) \times U(1)$. This is achieved by the introduction of neutral field B which couples to the weak hypercharge Y.

The physical fields that correspond to the neutral current gauge boson Z^0 and A, the photon of the electromagnetic field are given by the linear combination of the W_3

field and weak hypercharge field B.

$$Z^0 = W_3 \cos\theta_W - B \sin\theta_W \tag{2.9}$$

$$A = W_3 \sin\theta_W + B \cos\theta_W, \tag{2.10}$$

the weak mixing angle θ_W, or the Weinberg angle is a parameter that has to be determined experimentally.

The weak eigenstates of quarks are not the same as the mass eigenstates. As a result the quark flavors can undergo mixing. An up quark can be converted to a down quark and otherwise. The flavor change is mediated through charge current interactions. Neutral current mediated flavor changes are not observed in nature. The transition probability between different quark flavors is described by the Cabibo-Kobayashi-Maskawa matrix (CKM-matrix).

$$\begin{pmatrix} d' \\ s' \\ b' \end{pmatrix} = \begin{pmatrix} V_{ud} & V_{us} & V_{ub} \\ V_{cd} & V_{cs} & V_{cb} \\ V_{td} & V_{ts} & V_{tb} \end{pmatrix} \begin{pmatrix} d \\ s \\ b \end{pmatrix}$$

2.3 Electroweak Symmetry Breaking and Higgs Mechanism

In the $SU(2)_L \times U(1)_Y$ gauge description of electro-weak interaction, all the gauge bosons need to be massless to preserve the gauge symmetry. However, this description is not true since W and Z bosons are indeed observed to be massive. The introduction of explicit mass terms in the Lagrangian causes divergences in the theory. The problem is solved by introducing an isosopin doublet with weak hypercharge Y=1.

$$\varphi = \begin{pmatrix} \varphi^+ \\ \varphi^0 \end{pmatrix} \quad \text{with} \quad \begin{aligned} \varphi^+ &= (\varphi_1 + i\varphi_2)/\sqrt{2} \\ \varphi^0 &= (\varphi_3 + i\varphi_4)/\sqrt{2}, \end{aligned} \tag{2.11}$$

with the choice of a covariant derivative

$$D_\mu = \partial_\mu + ig\frac{\tau_a}{2}W_\mu^a, \tag{2.12}$$

where W_μ^a's are the three gauge fields,τ_a's are the generators of $SU(2)$ group and g is the coupling constant, the following Lagrangian is guaranteed to be invariant under SU(2) local gauge transformations.

$$L = (D_\mu\varphi)^\dagger(D^\mu\varphi) - V(\varphi) - \frac{1}{4}W_{\mu\nu}W^{\mu\nu}, \tag{2.13}$$

where $V(\varphi)$ is the potential given by

$$V(\varphi) = \mu^2\varphi^\dagger\varphi + \lambda(\varphi^\dagger\varphi)^2$$

For $\lambda > 0$ and $\mu^2 < 0$, the potential has a minimum at

$$|\phi| = -\frac{\mu^2}{2\lambda} \tag{2.14}$$

This set of all points at which $V(\phi)$ is minimum is invariant under $SU(2)$ transformations. The potential is minimum with the following choice of components.

$$\phi_1 = \phi_2 = \phi_4 = 0 \quad , \quad \phi_3^2 = -\frac{\mu^2}{\lambda} \equiv v^2 \tag{2.15}$$

The Lagrangian description of the system is not expected to change by choosing a particular value of the field, in this case the ground state. However it is observed that the Lagrangian looses reflection symmetry when the field is expanded around the stable vacuum. Thus the symmetry is "spontaneously broken". The ground state of the field $\phi(x)$ or the "vacuum expectation value" is given by

$$\phi_0 = \sqrt{\frac{1}{2}}\begin{pmatrix} 0 \\ v \end{pmatrix} \tag{2.16}$$

Excitations from the ground state gives rise to the physical Higgs field

$$\phi(x) = \sqrt{\frac{1}{2}}\begin{pmatrix} 0 \\ v + h(x) \end{pmatrix}$$

Out of the four scalar fields introduced the Higgs field h(x) is the only remaining one.

The gauge boson masses generated can be determined by substituting the vacuum expectation value into the Lagrangian. The term that we are interested in is $(ig/2\tau W_\mu \phi)^\dagger (ig/2\tau W^\mu \phi)$.

$$\begin{aligned}\left|ig\frac{1}{2}\tau W_\mu \phi\right|^2 &= \frac{g^2}{8}\left|\begin{pmatrix} W_\mu^3 & W_\mu^1 - iW_\mu^2 \\ W_\mu^1 + iW_\mu^2 & W_\mu^3 \end{pmatrix}\begin{pmatrix} 0 \\ v \end{pmatrix}\right|^2 \\ &= \frac{g^2 v^2}{8}\left[(W_\mu^1)^2 + (W_\mu^2)^2 + (W_\mu^3)^2\right],\end{aligned}$$

However $(W_\mu^1)^2 + (W_\mu^2)^2$ is the product of physical fields $2W_\mu^+ W_\mu^-$. Therefore

$$\left|ig\frac{1}{2}\tau W_\mu \phi\right|^2 = \left(\frac{1}{2}vg\right)^2 W_\mu^+ W_\mu^- + \frac{g^2}{8}(W_\mu^3)^2$$

Comparing the first term with the mass term expected for a boson we have

$$M_W = \frac{1}{2}vg$$

Similarly the photon mass (which is zero) and Z-boson mass can be deduced from an $SU(2)_L \times U(1)_Y$ gauge invariant Lagrangian. The mass of the Z-boson can be shown to be

$$M_Z = \frac{1}{2} v \sqrt{g^2 + g'^2}$$

where g' is the strength of the coupling to $U(1)_Y$ group.

The fermions acquires mass through Yukawa coupling to the Higgs field. For example, to generate the electron mass an $SU(2) \times U(1)$ gauge invariant term is introduced to the Lagrangian

$$L' = -\lambda_e \left[(\bar{\nu}_e, \bar{e})_L \begin{pmatrix} \phi^+ \\ \phi^0 \end{pmatrix} e_R + \bar{e}_R(\phi^-, \bar{\phi}^0) \begin{pmatrix} \nu_e \\ e \end{pmatrix}_L \right] \tag{2.17}$$

After spontaneously breaking the symmetry

$$\phi = \sqrt{\frac{1}{2}} \begin{pmatrix} 0 \\ v + h(x) \end{pmatrix}$$

Therefore

$$L' = -\frac{\lambda_e}{\sqrt{2}}(\bar{e}_L e_R + \bar{e}_R e_L)v - \frac{\lambda_e}{\sqrt{2}}(\bar{e}_L e_R + \bar{e}_R e_L)h$$

The standard mass term of a fermion is given by

$$m\bar{\Psi}\Psi = m\bar{\Psi}_L\Psi_R + m\bar{\Psi}_R\Psi_L$$

Comparing the above two expressions we identify the electron mass to be,

$$m_e = \frac{\lambda_e v}{\sqrt{2}} \tag{2.18}$$

The ATLAS and CMS collaborations at the LHC have detected a new particle which is compatible with the Standard Model Higgs boson [9] [10]. All properties of this new particle measured until now are within the expectation of the Standard Model Higgs boson. In Figure 2.2b, the resonance peak of the Higgs boson decaying into two photons is shown. The measured mass of the Higgs boson has been found to be $125.36 \pm 0.37(\text{stat}) \pm 0.18(\text{syst})\,\text{GeV}$ [11].

2.4 Theories Beyond Standard Model

Standard Model is an extremely successful theory. The agreement between Standard Model predictions and measurements is shown in Figure 2.3. However, the Standard Model is not a complete theory. There are problems in the theory.

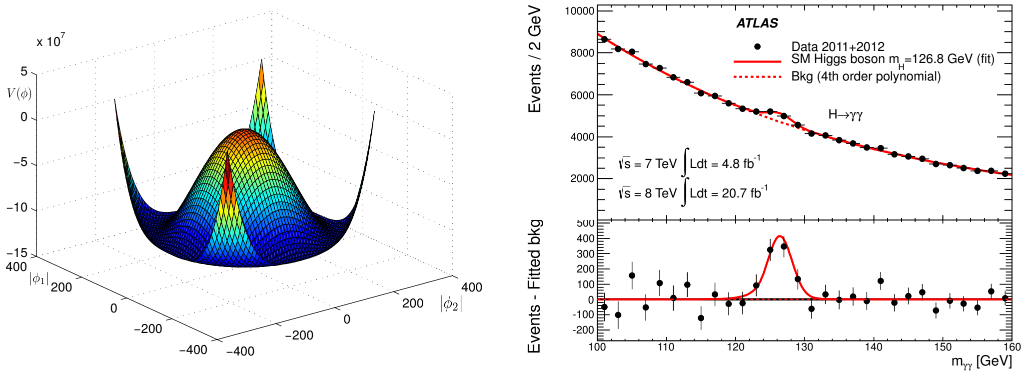

(a) (b)

Figure 2.2: (a) The Higgs potential for $\mu < 0$, $\lambda > 0$, Higgs-boson mass of 126.8 GeV and a vacuum expectation value of 246 GeV. Adapted from [7] (b)The Higgs signal observed in the diphoton channel. The fit is consistent with a Higgs hypothesis with mass 126.8 GeV [8].

In the Standard Model, the neutrinos are massless, however neutrino oscillations, a phenomenon in which the flavor eigenstates evolve in time into another flavor eigenstate has been observed. This suggests a non-zero neutrino mass.

So far gravity has not been included in Standard Model. Attempts to develop a renormalizable quantum field theory of gravity were all unsuccessful. The Standard Model is also not able to predict the baryonic asymmetry in the universe. The universe is primarily made up of matter particles compared to anti-matter particles. The Standard Model offers no explanations for this asymmetry.

Cosmological models shows that our universe consists of only 4% matter that is made up of Standard Model particles. The remaining is thought to be 27% dark matter and 69% dark energy or *cosmological constant*. Quantum field theories predict the existence of zero-point energy or vacuum energy of space. It also observed in phenomena like Casimir effect. The vacuum energy should contribute to the *cosmological constant* term in the Einstein field equations of general relativity. However the measured value of cosmological constant differ significantly from the vacuum energy measurements by a staggering 120 orders of magnitude [13].

Galaxy rotation curves confirm the presence of dark matter aggregates which only interact gravitationally with ordinary matter. However the Standard Model offers no candidates for this kind of elusive particles which probably only interact very weakly with ordinary matter.

Another problem is the *hierarchy problem*. Loop corrections to the Higgs boson

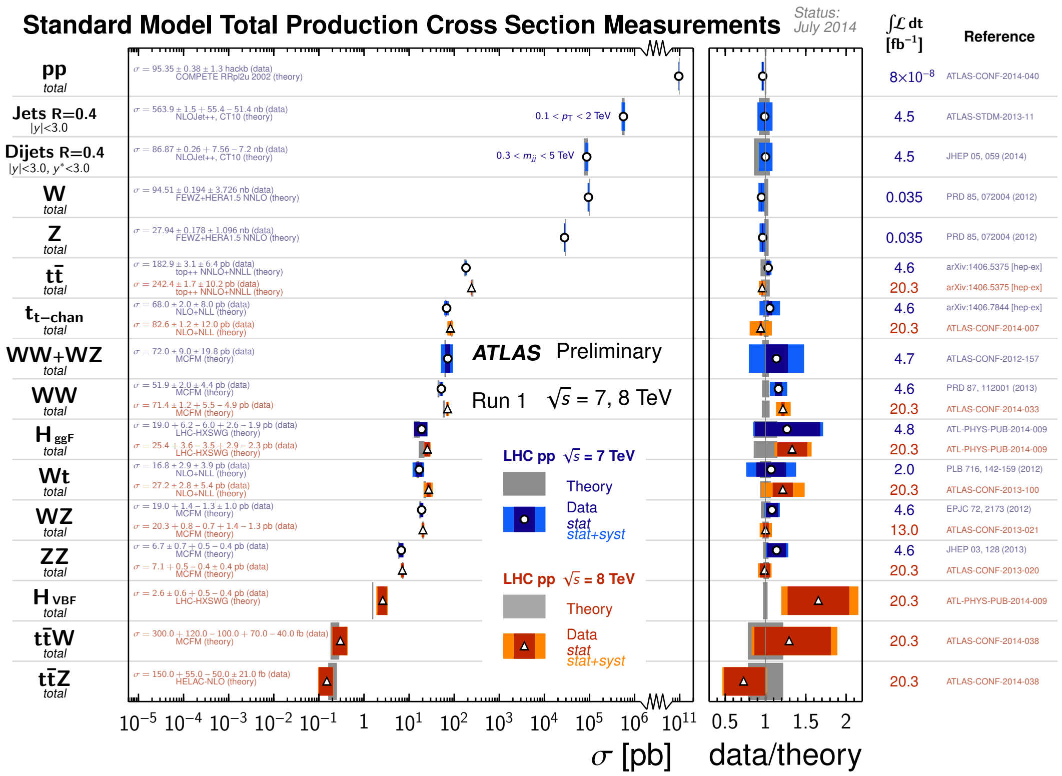

Figure 2.3: Standard Model cross sections predicted by theory and measured by the ATLAS experiment. The plot shows that the measured cross sections, within the uncertainties do not deviate significantly from the predictions [12].

mass is given by

$$\Delta m_H^2 = -\frac{|\lambda_f|^2}{8\pi^2}\Lambda_{\mathrm{UV}}^2 + \ldots \tag{2.19}$$

where λ_f is the Yukawa coupling of a fermion f and Λ_{UV} is the maximum energy scale up to which the theory is valid. This is usually considered to be the Planck Scale (10^{19} GeV). It is clear that loop corrections to Higgs boson mass are extremely large contrary to the observed higgs mass that is at electro-weak scale. There is no solution for this problem in the Standard Model

One of the prominent beyond standard model theory is based on a symmetry called "supersymmetry". According to this theory, each fermion in the standard model has a corresponding bosonic super partner and each boson has a corresponding fermionic super partner. Except for the spins, all other quantum numbers are the same. Since no super parners of comparable masses has been observed, the symmetry is not an exact symmetry. If it exist, it must be a broken symmetry. Super symmetry naturally solves the hierarchy problem as the bosonic and fermionic contributions to Higgs boson mass cancel each other.

Since the energy scales probed by the Large Hadron Collider are the highest until now, supersymmetric models can be tested even beyond the electroweak scale. In many super symmetric models the lightest super symmetric particle is stable and neutral and interacts very weakly with ordinary matter, making it an ideal candidate for Dark Matter.

Searches for several super symmetric models have been carried out at the LHC at 7 TeV and 8 TeV center of mass collision energies. However, all the results have been negative so far.

Chapter 3

Physics at the LHC

The measurements in this thesis are based on proton-proton collisions. The proton is a composite particle made up of two up quarks and one down valence quarks, which are bound together by the strong interaction. Proton-proton collisions are effectively collisions between the proton constituents at high collision energies. In this chapter a brief review of the structure of the proton and physics at hadron colliders is given. The physics of the associated production of Z-bosons with b-quarks and their final state is also reviewed in the later sections of the chapter.

3.1 Structure of the Proton

The study of collision processes by observing the energy, angular and multiplicity distribution of scattered products of the collision has been successfully employed in understanding the nature of matter and its interactions at small scales, ever since Rutherford's α-scattering experiment.

In classical Coulomb scattering experiments, particles like protons were considered to be point like. In later experiments with increased energies, a deviation from point like behavior was observed and the size and structure of the proton became apparent.

The structure of the proton was revealed by the scattering of a lepton off a proton. These experiments are called "deep inelastic scattering" (DIS) experiments. A typical process would be $eP \to e'X$, where e and e' are the incident and outgoing electrons, P is the proton and X denotes all the final state hadrons. The kinematics of the scattering depends on the momentum transfer $q = k - k'$ from the electron to the proton and the invariant mass of the hadronic final state. The variables that describe DIS are the following.

$$Q^2 \equiv -q^2 \tag{3.1}$$

$$\nu = P \cdot q \tag{3.2}$$

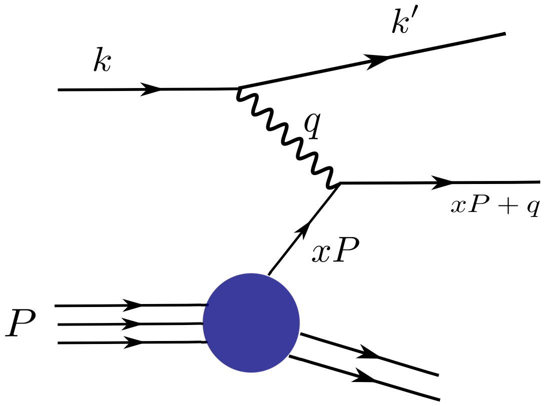

Figure 3.1: Schematic representation of Deep Inelastic scattering. An electron with four momentum k interacts with hadron with momentum P.

and

$$x = \frac{Q^2}{2M\nu} \tag{3.3}$$

$$y = \frac{q \cdot P}{k \cdot P} \tag{3.4}$$

where Q^2 is the negative square of momentum transfer q. ν is the energy transferred to the hadron in its rest frame. x is the fraction of momentum carried by the parton, also known as Bjorken-x and y is the fraction of energy lost by the electron in the nucleon rest frame.

The inelastic electron-proton scattering cross section can be written as

$$\frac{d^2\sigma}{dx\, dQ^2} = \frac{4\pi\alpha^2}{xQ^4}\left[(1-y)F_2(x,Q^2) + xy^2F_1(x,Q^2)\right] \tag{3.5}$$

where F_1 and F_2 are the structure functions of the proton.

The structure of the proton (or in general any hadron) is described by the parton model. According to the parton model hadrons are collection of quasi-free, point like particles called partons. Hadron-hadron collision cross sections are modelled as the sum of the cross sections of individual partons distributed within each hadron that participate in the collision.

In the naive parton model, the proton consists of point like massless partons which do no interact with each other. Each of them carry a momentum $p_i^\mu = x_i P_i^\mu$. The transverse momenta of individual partons are neglected.

According to this model, the structure functions hold the relation:

$$2xF_1(x) \equiv F_2(x) = \sum_i e_i^2 f_1(x) + \mathcal{O}(\alpha(Q)), \tag{3.6}$$

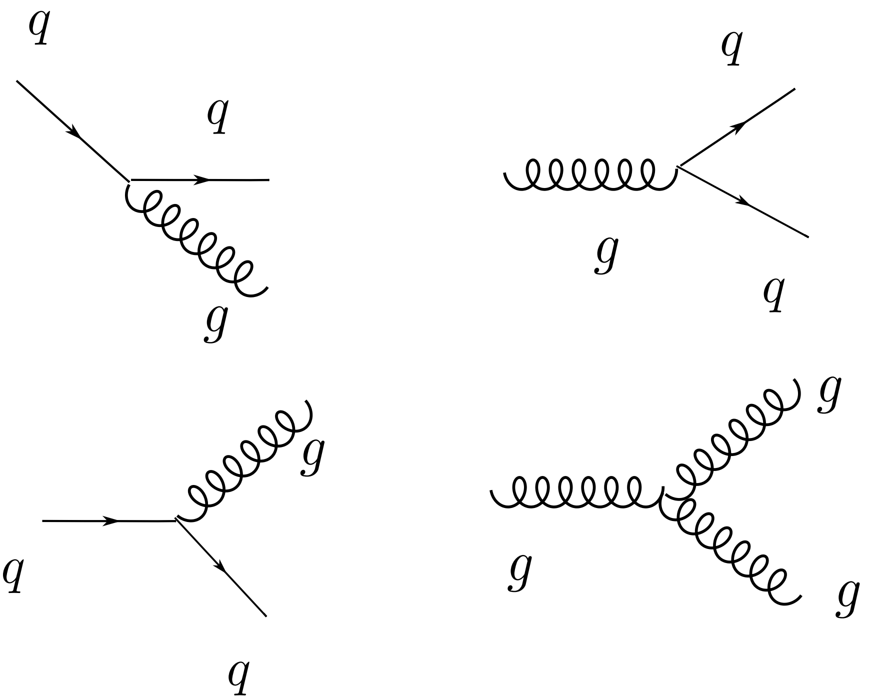

Figure 3.2: Splitting graphs responsible for violation of Bjorken scaling.

where $f_1(x)$ are the parton distribution function and e_i is the parton charge. To the first order, the structure functions are independent of Q^2, a property known as Bjorken scaling. Even though the parton model offers a very good description of the proton, experiments suggest that only half of the momentum is carried by charged particles. The remaining neutral component can be attributed to the gluons.

3.1.1 Parton Distribution Functions

Parton distribution functions (PDFs) are defined as the probability of finding a particle within a longitudinal momentum fraction x and $x + dx$, at a given energy scale Q^2. Parton distribution functions cannot be obtained from perturbative calculations. Hence they need to be obtained from fits to the data. In the Figure 3.3, HERA PDF's are shown. Here the PDF is parameterized at a factorization scale of 1.9 GeV and evolved to 10 GeV. To make any meaningful predictions about the hard processes, a precise knowledge of the PDF's are essential.

In the QCD improved parton model, the gluon radiation gives small transverse momenta to the quarks. As a result the structure function is modified.

$$\frac{F_2(x, Q^2)}{x} = e^2 \int_x^1 \frac{dy}{y} f(y) \left[\delta\left(1 - \frac{x}{y}\right) + \frac{\alpha}{2\pi} P_{qq}\left(\frac{x}{y}\right) \ln \frac{Q^2}{m^2} \right]. \tag{3.7}$$

where $P_{qq}(z)$ is the splitting function, which represents the probability that a parent

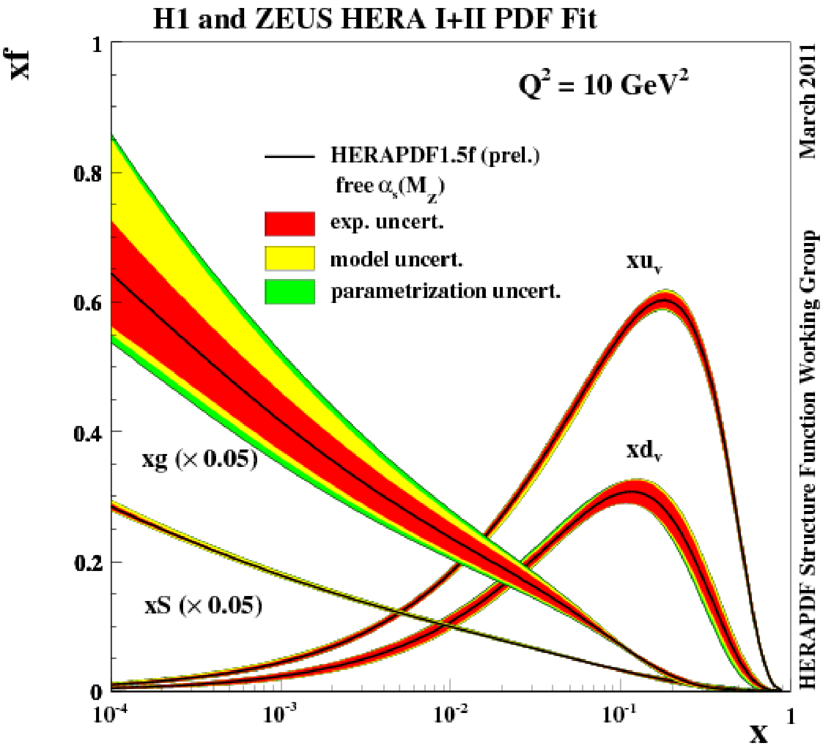

Figure 3.3: The parton distribution functions from HeraPDF [14] at $Q^2 = 100\,\mathrm{GeV}$ as a function of momentum transfer x. Gluon and sea quark distributions are scaled down by a factor of 20.

quark emits a gluon with a momentum $(1 - z)$. The feynman graphs for the splitting is shown in Figure 3.2. The term $f(y)$ is the parton distribution function, which is the probability of finding a parton with a longitudinal momentum fraction between x and $x + dx$.

The parameter m is a cut-off parameter. A cut-off scale μ, called factorization scale is introduced to avoid singularities as $m \to 0$. The parton distribution function can now be written as

$$f(x, Q^2) = f(x, \mu^2) + \frac{\alpha_s}{2\pi} \int_x^1 \frac{dy}{y} f(y, \mu^2) P_{qq}\left(\frac{x}{y}\right) \ln \frac{Q^2}{\mu^2} + O(\alpha_s^2) \tag{3.8}$$

The evolution of the parton distribution function as a function of Q^2 at a known x and a particular choice of factorization scale μ, the dynamics, is described by the Dokschitzer-Gribov-Lipatov-Altarelli-Parisi (DGLAP) equation

$$\frac{\partial f(x, \mu^2)}{\partial \ln \mu^2} = \frac{\alpha_s}{2\pi} \int_x^2 \frac{dy}{y} f(y, \mu^2) P_{qq}\left(\frac{x}{y}\right) + O(\alpha_s^2) \tag{3.9}$$

As Q^2 increases, more splittings are resolved resulting in low momentum quarks. As a result, the quark distributions increases at low values of x with increasing Q^2. This Q^2 dependance is manifested as scaling violations in the structure function distribution shown in Figure 3.4.

3.1.2 Proton-Proton Collisions

At high energy hadron colliders two types of processes can be distinguished, the hard process which can be calculated precisely using perturbative QCD and soft processes which cannot be well described by QCD. Phenomenological models exists to describe the soft processes. Even though our interest is in the hard process, it is invariably followed by the soft processes.

The QCD factorization theorem separates the short-distant process like hard scattering, initial and final state radiations from long-distant properties like hadronization evolution of parton distribution functions. According to the factorization theorem the cross section for two interacting protons can be written as the convolution of cross sections of the partonic content of the proton.

$$\sigma(s) = \sum_{i,j} \int dx_1\, dx_2 f_i(x1, \mu^2) f_j(x_2, \mu^2) \hat{\sigma}_{ij} \left(\hat{s}, \alpha_S(\mu^2), \frac{Q^2}{\mu^2} \right), \tag{3.10}$$

where μ is the factorization scale, $\hat{\sigma}_{ij}$ is the partonic cross section for partons i,j and f_i are the parton distribution functions. μ can be thought of as the scale which separates long and short distance physics. A parton with transverse momentum less than μ is considered to be the part of the hadron structure and it is absorbed in the parton distribution function. Partons above this scale participate in the hard scattering with a cross section $\hat{\sigma}$. The choice of the scale μ depends on the process that is considered.

3.2 Associated Production of Z-bosons with b-quarks

Electroweak gauge bosons in association with one or more b-quarks are produced at LHC with large cross section. These processes are background to many New Physics searches at LHC, For example, the Higgs boson decay process $H \rightarrow Z^* Z^* \rightarrow$ where the two virtual Z-bosons decay into leptons is an important signature for Higgs measurement. The process $pp \rightarrow Zb\bar{b}$ with the leptonic decay of the Z-bosons and the semileptonic decay of the b-quarks constitute a large fraction of background for this process. Therefore a very good understanding of these processes are required to increase the chances of observing New Physics signals. The leading order Feynman graph contributing to the production of Z boson with associated b quarks are given in Figure 3.5.

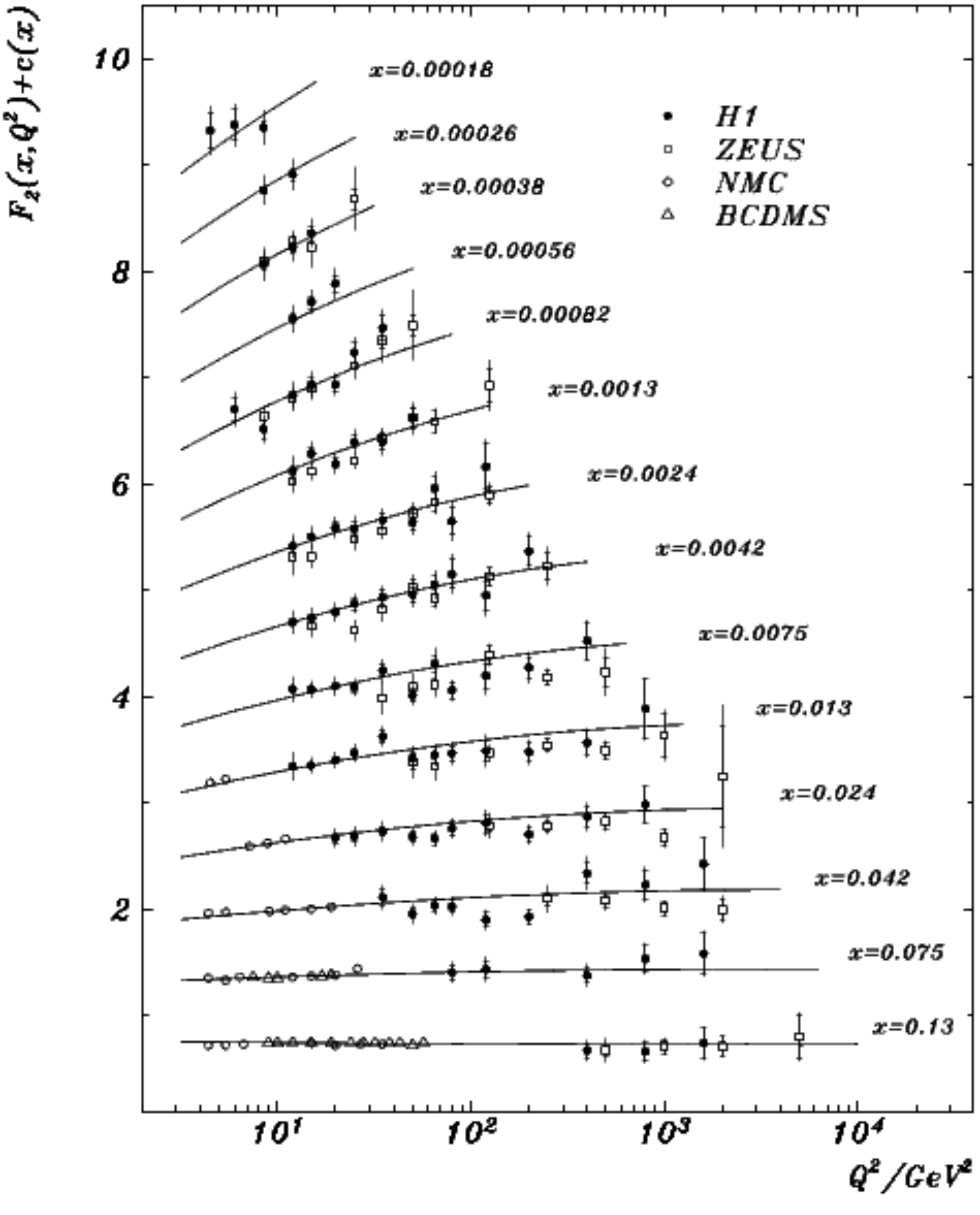

Figure 3.4: Structure function F_2 measured as a function of Q^2 at Hera experiments H1 and ZEUS and CERN experiments NMC and BCDMS. At low x values the structure function shows a strong Q^2 dependence indicating violation of Bjorken scaling [15].

There are basically two different schemes for the cross section calculation of the

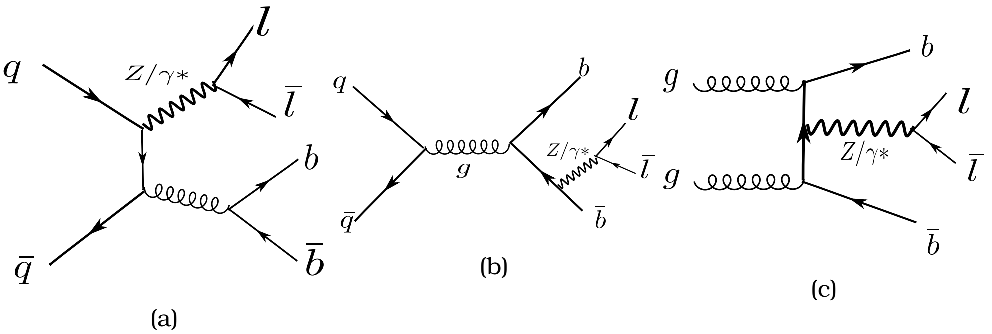

Figure 3.5: Leading order diagrams for the production of Z-boson in association with two b-quarks.

process, the fixed flavor scheme and variable flavor scheme. In the fixed-flavor scheme the quark flavors are kept fixed irrespective of the energy scales involved. In this scheme there are three flavor (u,d,s), four flavor (u,d,s,c) as well as five flavor (u,d,s,c,b) schemes available.

In the variable flavor scheme, the number of quark flavors considered is given by a step function as a function of the energy scale. At hard scales above the mass of the heavy quarks the heavy-flavor PDF's are used in the calculation of the process.

For the calculation of $Z + b\bar{b}$ process, the four flavor as well as the five flavor number schemes can be used. In the four flavor scheme, the b-quarks are generated dynamically by gluon splitting ($g \rightarrow b\bar{b}$).In the five flavor scheme, since the Z-mass scale is well above the production threshold of b-quarks, initial states with all the flavors up to b-quarks are parameterised and evolved in Q^2. A collinear $g \rightarrow b\bar{b}$ splitting is assumed with one of the b-quark escaping down the beam line and the other quark participating in the hard scattering. The b-quarks are treated as originating from the proton sea. The leading order and next to leading order QCD calculations differ from each other due to poorly constrained b-PDF's [16]. The b-quark distribution functions can be derived perturbatively from the DGLAP evolution equation. The process $gb \rightarrow Zb$ is sensitive to gluon density of the proton.

The life-time of the Z-boson is about 10^{-25} s. It decays into fermion anti-fermion pairs. The decay into top-quark pairs is heavily suppressed due to the high mass of the tops. The branching ratio of Z-boson decays is listed in Table 3.1. Even though the branching fraction for Z-boson decays into hadrons are higher, the lepton final states with electrons and muons offer a very clean signature at hadron colliders.

3.2.1 B-hadron Production

The schematic representation of B-hadron production is shown in Figure 3.6. In this scheme, the two quarks from the incoming protons interact in the hard scattering and produces a gluon. This gluon emits two b-quarks of which one radiates a Z-boson.

Final state	BR %
e^+e^-	3.363 ± 0.004
$\mu^+\mu^-$	3.366 ± 0.007
$\tau^+\tau^-$	3.367 ± 0.008
neutrinos	20.06
hadrons	69.91

Table 3.1: Branching ratios of the Z-boson [17].

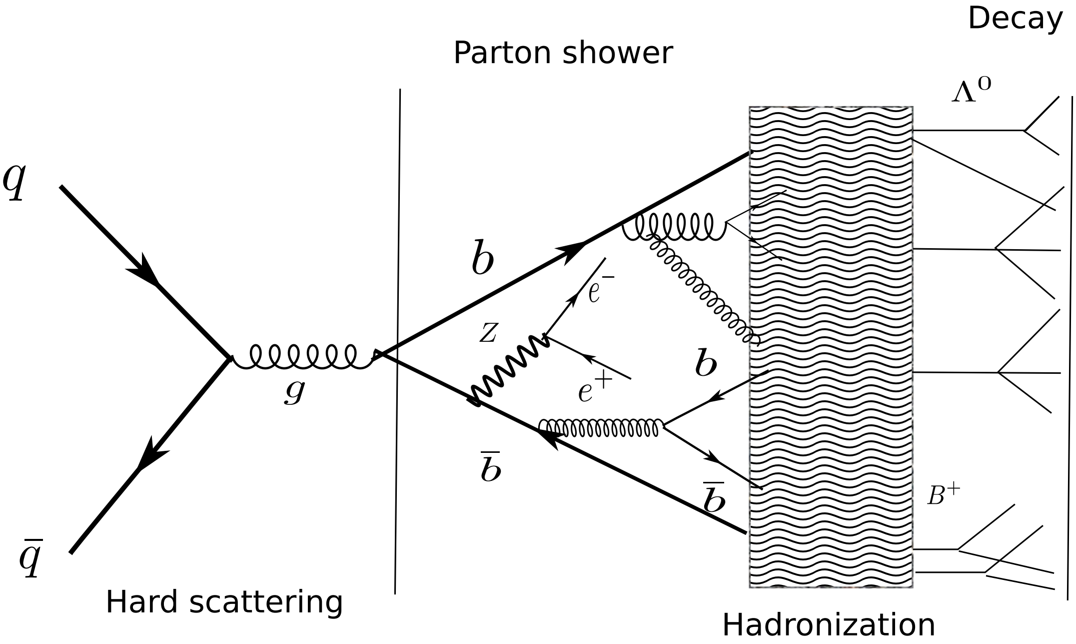

Figure 3.6: Schematic representation of production of Z-boson in association with b-quark pairs and subsequent fragmentation and hadronization and decay of heavy flavor hadrons.

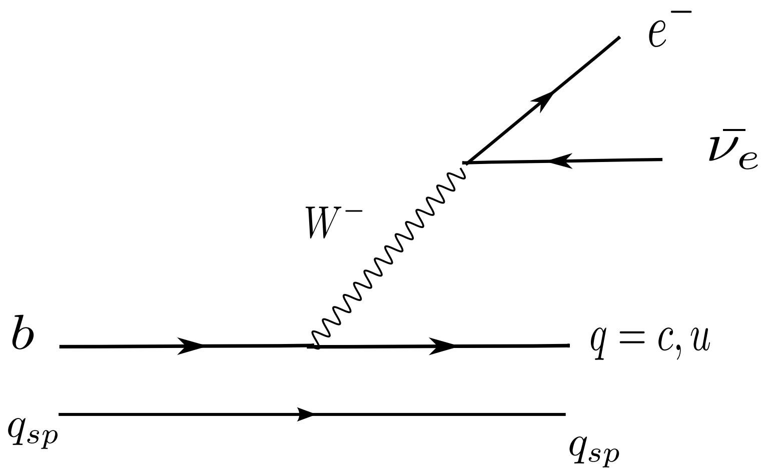

Figure 3.7: Spectator quark diagram for B meson decay.

The Z-boson subsequently decays into an electron positron pair. The b flavoured quark and anti-quark continue to separate from the primary interaction point. Due to QCD confinement the strong force increases with increasing separation until a quark anti-quark pair is produced from the vacuum. These quarks can radiate gluons which in turn split into quark anti-quark pair. This cascade of quark and gluon production process known as parton-showering continues to take place until the energies of the partons reaches a particular scale. At that scale the partons combines to form bound states which are called hadrons. These hadrons decay into lighter particles, either through strong or weak interactions.

In addition to the hard scattering, b-quarks can also be produced through gluon splitting in the parton shower. The rate of production is B-hadrons via gluon splitting is quite high in high energy hadron colliders. Eventually this becomes the dominant background in this study.

Since it is energetically more favourable for a b or $\bar{b}$ quark to combine with another single quark from vacuum, about 90% of the times B mesons (B_o, $\bar{B}^0$, B^+, B^-) are the final hadronized products in the chain of showering of b flavoured quarks. Due to their high mass the formation of strange and charm quarks during parton showering is relatively suppressed compared to lighter quarks. Therefore B_s^0 production constitute approximately 10% of the b-flavoured final states.

The ground state b hadrons decay further to lighter hadrons through charged current interaction. The b-quark in the meson carries away a significant fraction of the momentum of the meson. Therefore it is reasonable to assume that its decay is independent of light quarks in the hadron. The semileptonic decay of B-hadron in such a spectator quark model is shown in Figure 3.7. The branching fraction for this direct semileptonic decay is 10.86×10^{-2} Cascaded decay of the b-quark ($b \to c \to e$) also contribute to the semileptonic decay final states. The inclusive branching fraction for the decay with at least one electron in the final state is $19.3 \pm 0.5 \times 10^{-2}$ [33]. The energies of these electrons are less compared to those coming from Z-boson decays, hence they are also called “soft” electrons.

In this thesis, a pair of 2 opposite sign electron final states are probed which is compatible with the decay topology of a Z-boson into e^{+}, e^{-} and the two $b\bar{b}$ decay into e^{+}, e^{-}. The kinematics and environment in which these two categories can be potentially observed is quite different, However with the ATLAS detector, identification of these final states is possible.

Chapter 4

Experimental setup

In this chapter a brief overview of the Large Hadron Collider (LHC) as well as a description of **A** **T**oroidal **L**HC **A**pparatu**S** (ATLAS) detector is given. In Section 4.1 a brief overview of the pre-accelerating system as well as the LHC machine is given and in Section 4.2 an overview of the ATLAS detector and its various components are described.

4.1 The Large Hadron Collider

The Large Hadron Collider (LHC) is one of the largest scientific instrument in the world at present. It is located at the European Organization for Nuclear Research(CERN), across the border of France and Switzerland. A scheme of the machine is given in Fig. 4.1. A detailed review of LHC can be found in [18]

The accelerator is located in a circular tunnel of circumference 27 km. The LHC accelerates proton bunces in opposite directions in separate beam pipes. The bunches are crossed at four interaction points at the center of four LHC experiments namely ALICE [19], ATLAS [20], CMS [21] and LHCb [22]. Proton collisions happen during bunch crossings and the detectors detect the particles produced in the collissions. The machine is designed to accelerate protons up to 7 TeV per beam, thus producing a center of mass energy of $\sqrt{s} = 14$ TeV.

The acceleration sequence of protons starts with a linear accelerator called Linac2. Hydrongen gas is fed to a duoplasmatron which gives H^+. These ions are accelerated by the Linac2 to 50 MeV. They are then injected into the Proton Synchrotron Booster which accelerates them up to 1.4 GeV. After this acceleration step the protons are sent to the Proton Synchrotron (PS) where the proton energy is increased to 25 GeV. Subsequently they are sent to the Super Proton Synchrotron (SPS) to accelerate them up to 450 GeV. Finally, these protons are injected into the LHC where the final acceleration takes place. The proton beams circulate the ring in bunches. Under nominal operating conditions, each proton beam consists of 2808 bunches, with each bunch containing about 10^{11} protons.

The design energy of LHC is $\sqrt{s} = 14$ TeV. However during a powering test in 2008, an electrical fault occurred producing electrical as well as mechanical damages. The

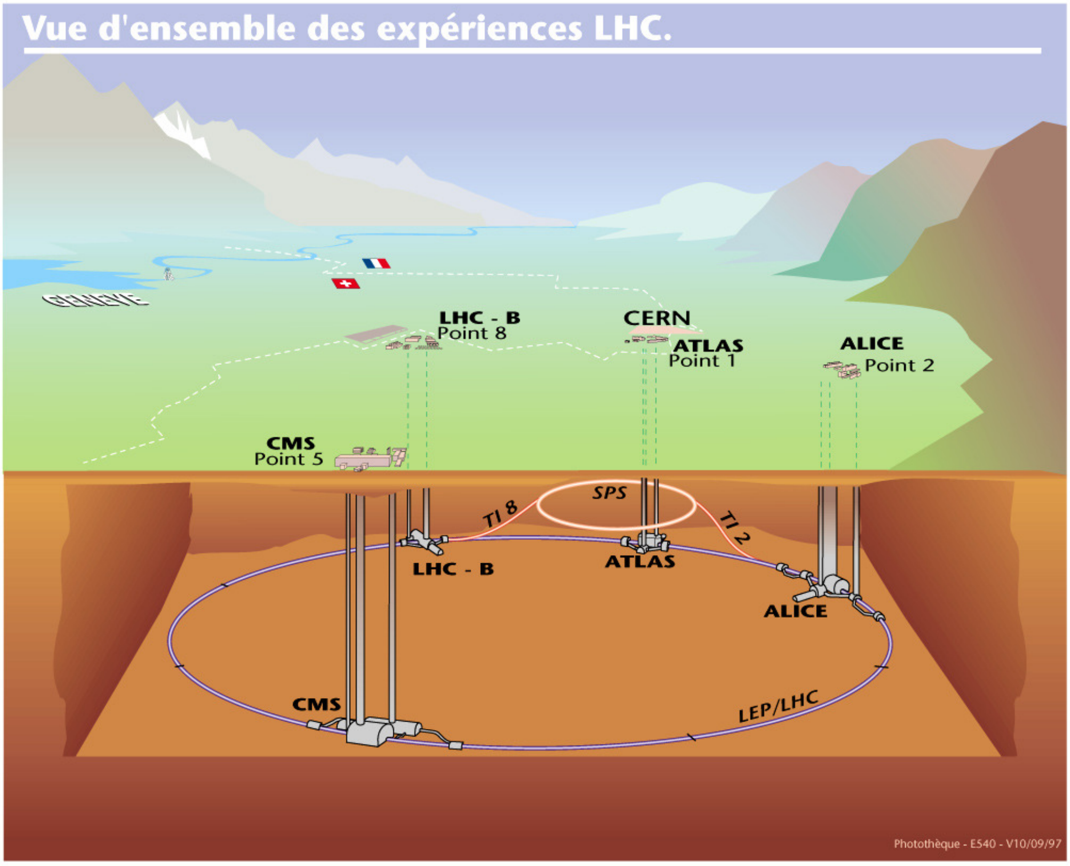

Figure 4.1: Sketch of the locations of the four main experiments(ALICE,ATLAS,CMS and LHCb). The depth of the tunnel varies from 50 m to 150 m underground. Image [23].

reason for the fault was found out to be a faulty solder connection [24]. Several problematic connections were repaired in several other magnets. Until further repairs could be made it was decided to run the LHC at a reduced energy. In 2010 and 2011 the LHC was operated at 3.5 TeV per beam, producing $\sqrt{s} = 7\,\text{TeV}$ collisions. In 2012 the energy was increased to 4 TeV per beam, producing $\sqrt{s} = 8\,\text{TeV}$ collisions. The LHC is shutdown during 2013 and 2014 for a series of repairs as well as detector upgrades. The machine is expected to run at $\sqrt{s} = 13\,\text{TeV}$ during the post repair startup expected in 2015. Major part of this thesis uses the $\sqrt{s} = 8\,\text{TeV}$ data taken during 2012 run period. Data recorded at $\sqrt{s} = 7\,\text{TeV}$ during the 2011 run period has been used for the analysis in chapter 5

4.1.1 Luminosity

The event rate R in a collider experiment is proportional to the interaction cross section σ_{int} [25]. The relationship is given by

$$R = L\sigma_{\text{int}}. \tag{4.1}$$

The proportionality constat L is called the luminosity. If n_1 and n_2 are the number of particles in two colliding bunches which collide at a frequency f, the luminosity is

$$L = f\frac{n_1 n_2}{4\pi\sigma_x\sigma_y}. \tag{4.2}$$

Where σ_x and σ_y are the transverse beam profiles in the horizontal and vertical direction. The beam profiles can be expressed in terms of two quantities namely *transverse emittance*, ϵ and *amplitude function*, β. The beam quality parameter ϵ reflects the process of bunch preparation. The β function is a beam optics quantity that is determined by the magnet configuration. The transverse beam profile σ is related to ϵ and β through

$$\epsilon = \pi\frac{\sigma^2}{\beta} \tag{4.3}$$

With β and ϵ the expression for luminosity becomes

$$L = f\frac{n_1 n_2}{4\sqrt{\epsilon_x\beta_x^*\epsilon_y\beta_y^*}} \tag{4.4}$$

where $\beta_{x,y}^*$ is the β function at the interaction point.

In order to increase the production rate of rare physics events, the luminosity has to be increased. This can be achieved by operating the accelerator with a great number of protons per bunch with low emittance and low β function at collision point.

The instantaneous luminosity as well as integrated luminosity delivered by LHC and recorded by ATLAS detector is shown in Figure 4.2

With increasing luminosity, the average number of interactions per bunch crossing, μ also increases.

$$\mu = L_{\text{int}}\frac{\sigma_{\text{inel.}}}{fn_b} \tag{4.5}$$

where $L_{\text{int.}}$ is the integrated luminosity, σ_{inel} is the proton-proton ineleastic cross section and n_b is the number of bunches per beam. The quantity μ is also a measure of the number of multiple interactions per bunc crossing or “pile up”. The distribution of μ is shown in Figure 4.2c.

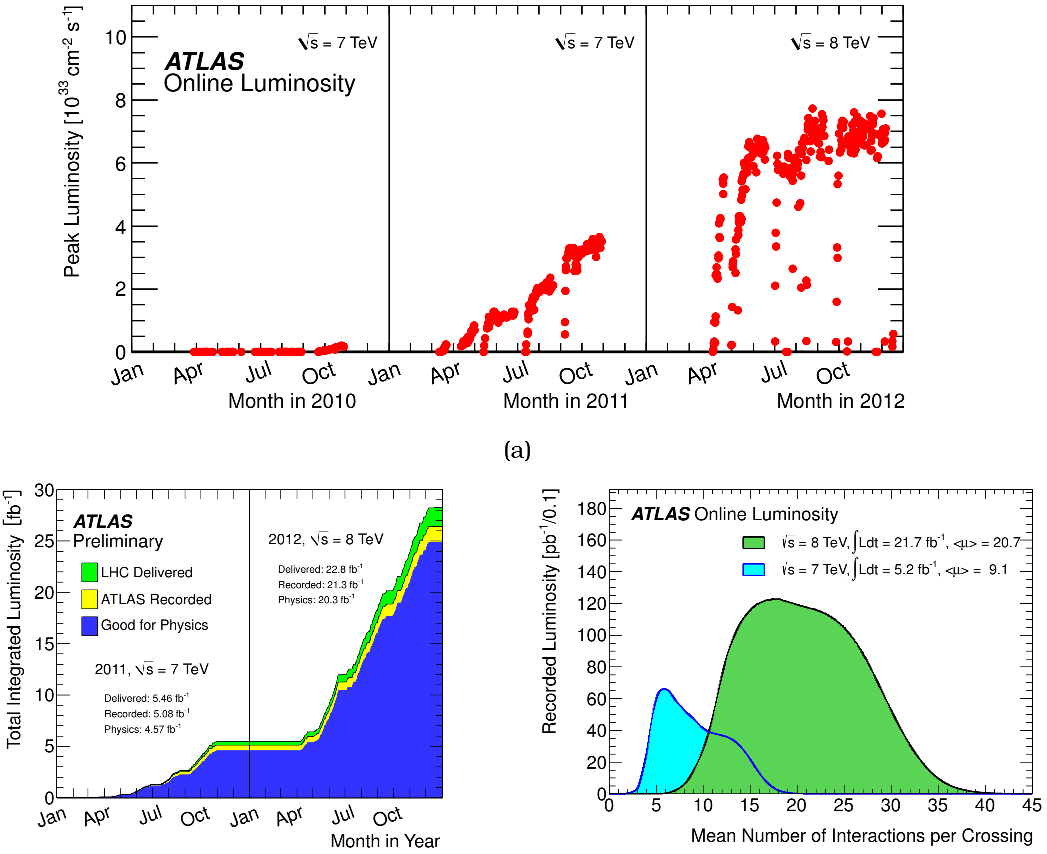

(a)

(b)

(c)

Figure 4.2: (a) peak instantaneous luminosity recorded by ATLAS (b) Total integrated luminosity delivered by LHC and recorded by ATLAS (c) “pile up” or average interactions per bunch crossing for 2011 and 2012 run periods [26].

4.2 ATLAS detector

The ATLAS detector is located at one of the interaction points in the LHC. A three dimensional view of the detector is shown in Figure. 4.3. The detector is 25 m in diameter, 45 m in length and weighs about 7000 tonnes.

The detector is forward backward as well as cylindrically symmetric. The beam pipe is located along the longitudinal cylindrical axis. The nominal proton-proton collision point is at the center of the detector where the cylidrical axis intersects with the forward-backward symmetry axis. This point defines the co-ordinate origin of the ATLAS detector system.

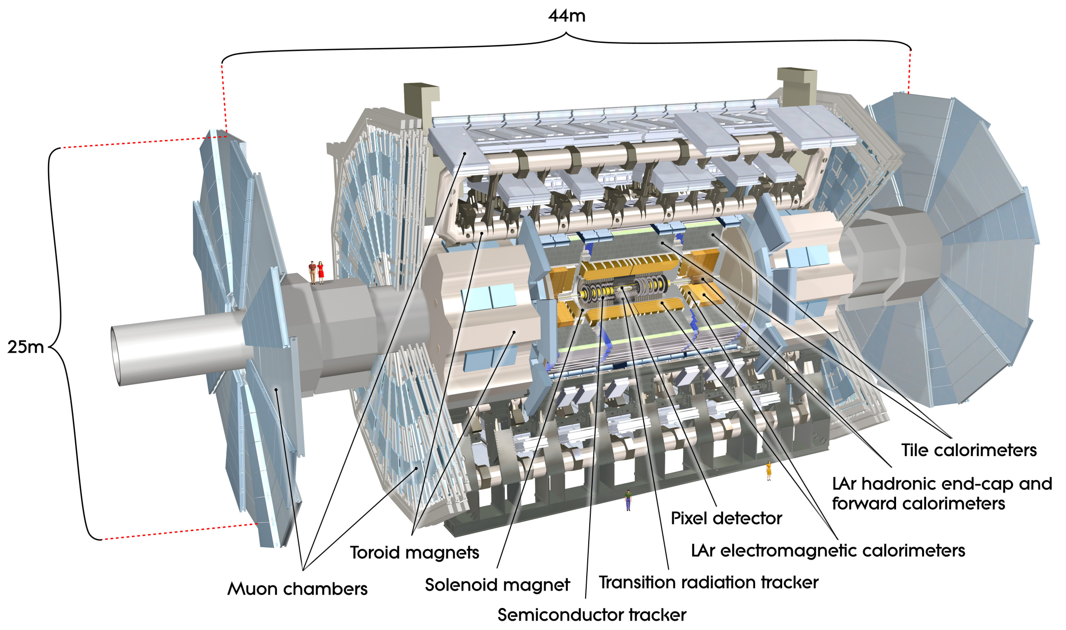

Figure 4.3: Cut away view of the ATLAS detector. A cartoon of two human beings are also included to highlight the size of the detector [26].

4.2.1 Co-ordinate system

The ATLAS co-ordinate system is a right handed co-ordinate system with the positive x-axis defined as pointing from the interaction point to the center of the LHC ring. The positive y-axis is defined as pointing upwards. The side A of the detector is defined as the positive z side and side C is defined as the negative z side. The cylindrical coordinates r, ϕ are used in the transverse plane with the azimuthal angle ϕ measured around the longitudinal axis along the beam line. The polar angle θ is measured as the angle from the longitudinal axis. The pseudorapidity η is defined as $\eta = -\ln[\tan(\theta/2)]$. The distance measure ΔR is defined in the $\eta - \phi$ space, as $\Delta R = \sqrt{\Delta\eta^2 + \Delta\phi^2}$

4.2.2 Inner Detector

At design luminosity, proton-proton collisions produce approximately 1000 particles every 25 ns within the central region of the detector ($|\eta| < 2.5$). The inner detector (ID) has been designed to make precision measurements at this high track densities [27]. The ID is immersed in a solenoidal magnetic field of 2 T. This allows for momentum measurements as well as the separation of charged particles and neutral particles.

The ID consists of three complimentary sub-detectors namely pixel detector [28], silicon microstrip (SCT) detector [29] and transition radiation tracker (TRT) [30]. A

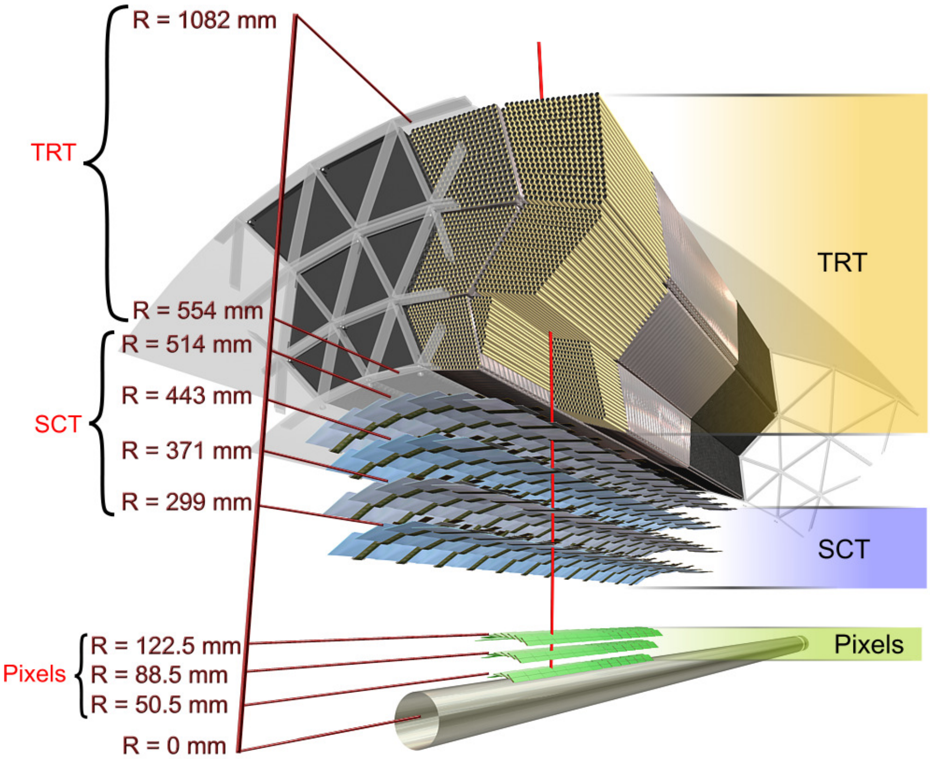

Figure 4.4: Graphics showing a charged particle track (red) passing through various sub-detectors of the inner detector. The particle traverses the beryllium beam pipe, 3 cylindrical pixel layers, 4 double layers of silicon-microstrip sensors (SCT) and approximately 36 straw tubes of the transition radiation tracker (TRT) [26].

schematic of the arrangement of these sub-detectors around the beam pipe is shown in Figure 4.4.

The pixel detector as well as the SCT are based on silicon technology. This allows for high granularity and very good position resolution due to their small size. The sensor is essentially a reverse biased p-n junction. The depletion region acts as the active detecting region. When a charged particle passes through the depletion region, electron-hole pairs are formed and they drift towards the respective electrodes. They are registered as signals at the electrodes and can be read out through output channels.

The pixel detector is the innermost component of the ID. Over three barrel layers and three end-cap disks it has over 80 million output channels with cell sizes of 50 µm × 400 µm and 50 µm × 600 µm. It has a position resolution of 10 µm in the r-ϕ plane and 115 µm along the Z direction.

The SCT is a concentric detector that surrounds the pixel detector. The SCT layers are composed of double layers of silicon strips. The dimensions are 80µm × 6cm.

The construction of the double layers is such that they are rotated by a stereo angle of 40 mrad with respect to each other. The spatial resolution of the SCT is 17 µm in $r - \varphi$ and 580 µm along Z direction. Even though the strip length is 6 cm a very good position resolution in Z direction is gained due to the stereo angle between the double layers. There are approximately 6 million read out channels for the SCT.

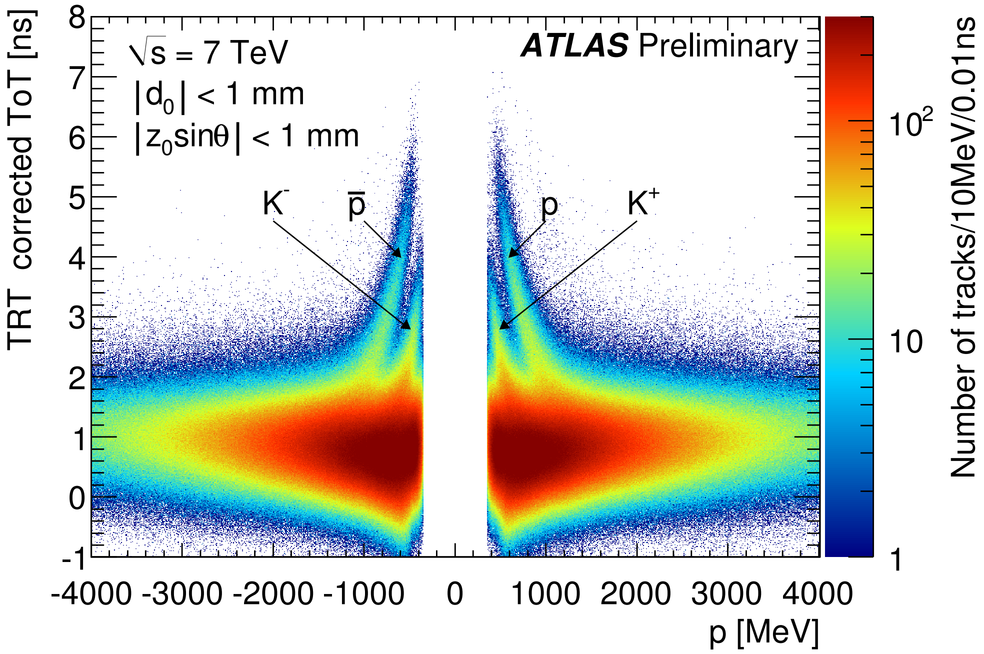

Figure 4.5: Time over threshold estimator showing particle identification capabilities of the TRT as a function of momentum [26].

The TRT is a straw-tube tracker. It consists of approximately 300,000 straw-tubes which can give a position resolution in φ of 130 µm. The TRT can produce up to 36 space points per charged particle. In addition it is also capable of particle identification. Charge particles while traversing different media emit radiation. Since the relativistic γ factor is larger for an electron compared to a hadron, electron emits more transition radiation than a hadron. The TRT read out system records two signal thresholds, high and low. The information about the number of high threshold and low threshold hits can be used to separate hadrons and electrons. Figure 4.5 shows a time over threshold estimator derived from TRT hits, which shows excellent particle identification capabilities. The momentum resolution of ID $\Delta p_T/p_T = 0.04\% \times p_T \oplus 2\%$ (p_T in GeV) [31].

4.2.3 The Calorimeter System

Calorimeter systems are used to measure the energy of particles. When a particle is incident on a material, depending upon its energy it undergo various interactions. As it can be seen from Figure 4.6, electrons and positrons above 10 MeV predominantly undergo bremsstrahlung, whereas photons undergo pair production. The bremsstrahlung photons as well as pair produced electrons and positrons produce secondary particles with progressively decreasing energies through the same mechanism until a cut-off energy is reached. This production of cascade of particles is called a shower. For a comprehensive overview, see [32].

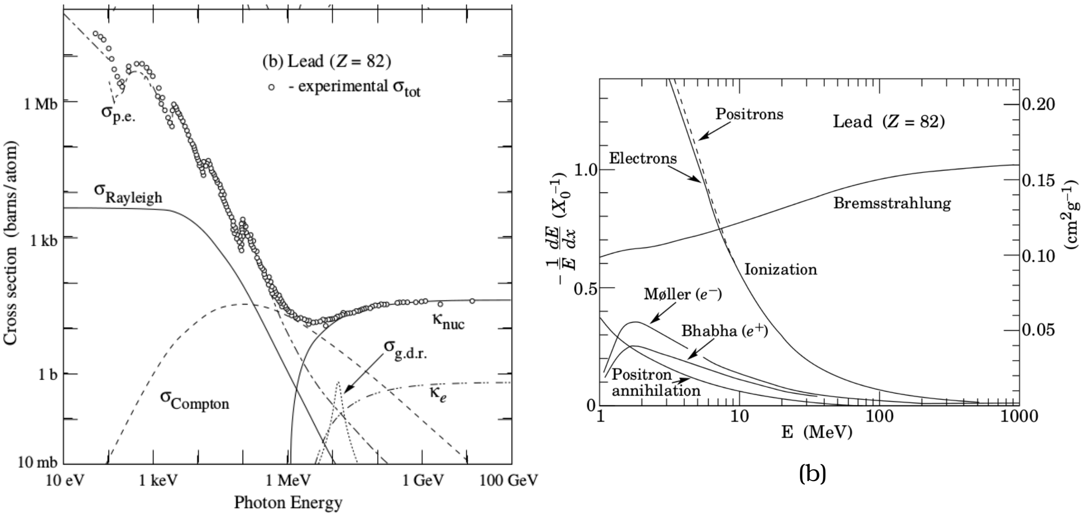

(a)

(b)

Figure 4.6: Cross sections for various interactions with matter for (a) photons and (b) electrons and positrons [33].

There are two types of particle showers; electromagnetic and hadronic. The longitudinal as well as lateral features of an electromagnetic shower can be parameterized through a quantity called radiation length X_0 which depends on the type of the material. The radiation length (X_0) is defined as the length at which a high energy electron looses all but 1/e of its energy or it is 7/9th of the distance at which the intensity of a photon beam is reduced to 1/e of its initial value while propagating through a given material.

Hadronic showers are more complicated than electromagnetic showers. Secondary hadrons are produced through successive strong interactions with a “nuclear interaction length” $\lambda_0 \approx 35A^{1/3}\mathrm{g\,cm^{-2}}$ (where A is the mass number of the material). A significant fraction of the primary energy is used in nuclear excitations, nucleon evaporations and spallations. Particles like neutral pions decay into photons which interact with the material only through electromagnetic interaction. Thus energy from the hadronic part is transferred to the electromagnetic part. Typically the figure of merit of hadronic calorimeters are quantified through the ratio of electromagnetic response to hadronic response.

The principle of calorimetry lies in measuring the energy deposited by particle showers through which the energy of the incident particle can be inferred. Since the shower lengths increases only logarithmically with respect to the energy of the particle, with a small detector volume very high energy particles can be measured. In addition the energy resolution is proportional to $1/\sqrt{E}$, therefore at high energies the relative resolution gets better as opposed to magnetic spectrometers. Calorimeters are sensitive to all kinds of particles, charged or otherwise. Through the reconstruction of missing energy, one can even measure the energy of a neutrino in an event.

The ATLAS calorimeters (Figure 4.7a) are "sampling" calorimeters. These are special kind of calorimeters in which the active materials are interleaved with passive materials. The passive layer is a low radiation length material, which is responsible for producing particle showers, while the active layer detects these showers and gives a measure of the particle energy. The full energy of the incident particle is inferred from a sample of the energy detected by the active layer.

The ATLAS electromagnetic calorimeter is a Lead-liquid argon(LAr) sampling calorimeter with accordion geometry [34], which provides full coverage in φ and $|\eta| < 3.2$. Incident particles produce showers in the low radiation length lead material. These shower particles causes ionization in the LAr medium. Argon is a noble gas which has a boiling point of 87 K. The low operating temperature reduces outgassing from the liquid containment and hence reduces contamination during operation thus ensuring high charge collection efficiency.

The thickness of the Lead layer ranges from 1.1–2.2 mm in η. A high voltage of 2 kV is applied across the LAr gap of $\approx$ 4 mm. This causes the drifting of the electrons towards the readout electrodes with a drift time of $\approx$400 ns. This is longer than the LHC bunch crossing structure of 25 ns. The accordion geometry where the gaps and absorbers are at an angle along the direction of the incoming particle allows for a fast charge collection as well as prevent the escape of particles through the gaps.

The LAr calorimeter has three layers in the longitudinal direction. The first layer has a pitch of 4 mm in η. This fine granularity allows for electron pion separation. The second layer has a granularity of 4×4 cm. The third layer has a granularity of 8×4 cm. The overall thickness of the electromagnetic calorimeter is over 24 radiation lengths in the barrel region and over 26 radiation lengths in the end-caps. The energy resolution of the electromagnetic calorimeter $\Delta E/E = 11.5\%/\sqrt{E} \oplus 0.5\%$

The hadronic sampling calorimeter uses scintillator tiles as well as LAr technology. The scintillator tile calorimeter is separated into a central barrel ($|\eta| < 1.6$ and two extended barrels (in the range $|\eta| < 1.7$). The end-caps ($1.5 < |\eta| < 3.2$) receives a

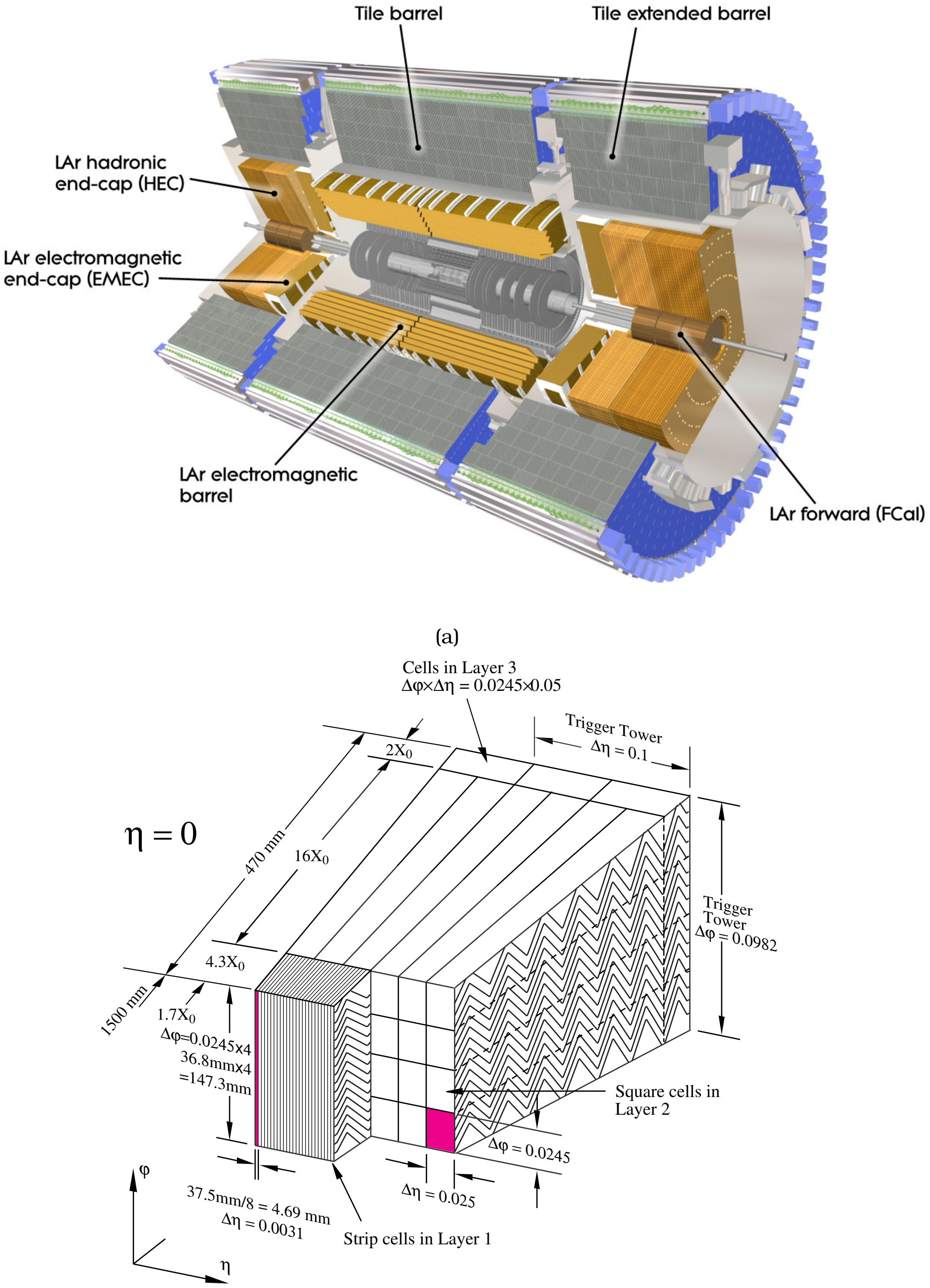

(a)

(b)

Figure 4.7: (a) Cut away view of the ATLAS calorimeter system (b) Sketch of a LAr barrel module showing different calorimeter layers with varying granularity in each layers[26].

higher radiation dose than the barrel, therefore radiation hard liquid argon technology is used in this region. The central region is also called TileCal (Tile calorimeter). It uses scintillating tiles as the active material and steel plates as absorbers. The scintillating tiles are coupled to wavelength shifting fibers and the signal are read out using photomultiplier tubes.

4.2.4 Muon Spectrometer

The muon spectrometer is the outermost detector element of the ATLAS detector [35]. It measures the position of muons as they propagate through the spectrometer. The bremsstrahlung energy losses of a charge particle is inversely proportional to its mass ($1/m^4$). Since the muon is roughly 200 times more massive than the electron, they easily pass through the calorimeter and reach the muon system.

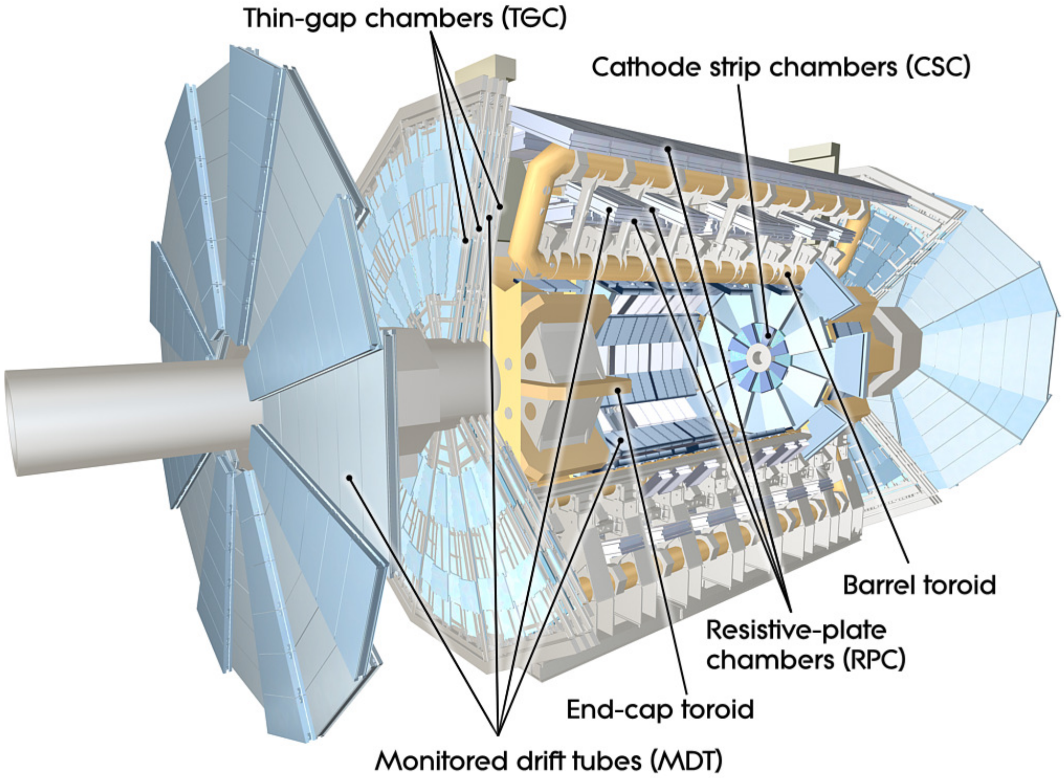

Figure 4.8: The ATLAS muon spectrometer [26]

The spectrometer is a immersed in a torroidal magnetic field. Air core torroidal magnets are used to reduce the multiple scattering. In the region $|\eta| < 1.4$ (barrel region), magnetic bending is provided by the barrel torroidal magnet. Between $1.6 < |\eta| < 2.7$ (end-cap region), the magnetic field is provided by end-cap torroidal magnets. In the transition region ($1.4 < |\eta| < 1.6$), the magnetic field is provided by a combination of barrel and end-cap torroid fields. The magnet configuration provides a field which is mostly orthogonal to the particle trajectories.

Monitored Drift Tubes (MDT) chambers and Cathode Strip Chambers(CSCs) make precision measurements in η. Thin Gap Chambers (TGC) and Resistive Plate Chambers (RPCs) provide low granularity fast signals to the trigger system. The target momentum resolution of the muon system is 10% for 1 TeV muons.

Chapter 5

Level-1 Calorimeter Trigger Monitoring

The event rates at hadron collider experiments like ATLAS are so high that existing data acquisition systems cannot record and store informations from all the events. Therefore only interesting events are recorded. The decision about which event to record and which one to discard is made by the so called trigger system. In this chapter the ATLAS trigger system with an emphasis to the authors ATLAS service task related to the timing monitoring of the calorimeter based trigger system is briefly reviewed.

5.1 ATLAS Trigger System

Many physics processes of interest at the LHC have a low cross section. This means the machine has to be operated at high event rates in order to increase the statistics of interesting events. This directly translates to the luminosity of the machine. The design luminosity of the LHC is $10^{34}\,\mathrm{cm}^{-2}\,\mathrm{s}^{-1}$ [36]. At these luminosities, roughly one billion proton-proton collisions would occur every second. However the ATLAS detector is designed to record only 200 events per second. Since this rate is 5 million times smaller than what is produced, only events of interest can be recorded.

The ATLAS detector has two levels of hardware triggers namely Level-1 (L1) and Level-2 (L2) and a software based Event Filter (EF). The L1 trigger processes coarse (reduced granularity) detector signals to arrive at trigger decision. The L1 has two subsystems, namely the Level-1 Calorimeter trigger (L1Calo) and Level-1 Muon trigger (L1Muon). L1Calo processes information from the calorimeter systems, mainly looking for signatures of isolated high transverse-energy electrons, photons, tau's, jets and missing E_T. L1Muon processes information from the Muon system.

The time interval between proton-proton bunch crossings at the LHC is 25 ns. This interval is very short to make a decision on whether to accept or discard the event. Therefore the detector data is held in memory buffers while L1 makes a trigger decision. Once a successful decision is made, the trigger system sends a Level-1 Accept (L1A) signal to the buffer memories and the event is accepted and read out by the data acquisition system, otherwise it is discarded. The time duration for which the event has to be kept in these buffers is limited by the volume of the buffers. In ATLAS this duration is 2.5 μs. Therefore the L1 has to make a trigger decision within 2.5 μs. For a safer margin this latency period has been set to 2 μs.

5.2 L1Calo Trigger

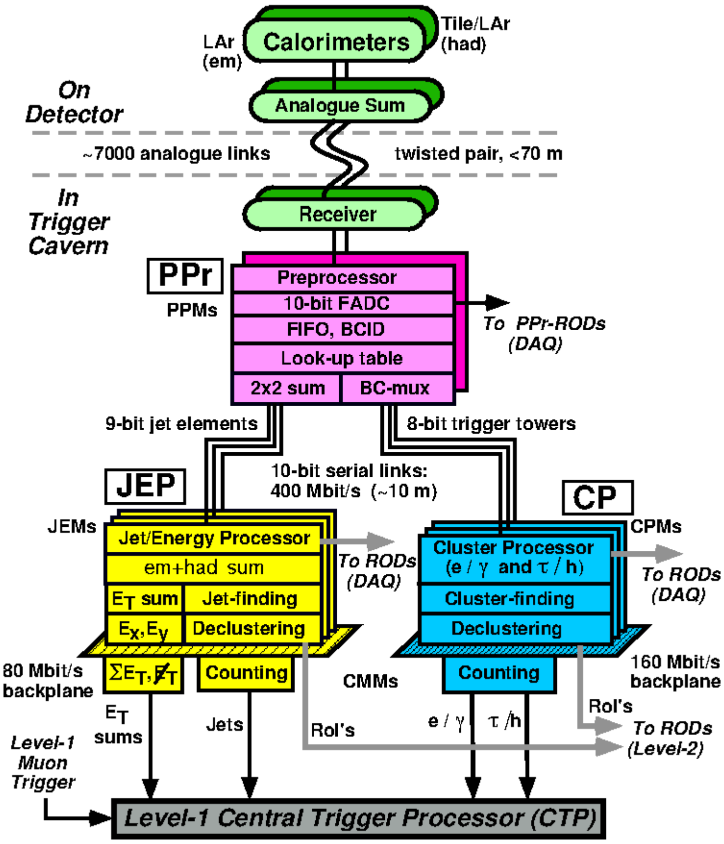

Figure 5.1: A schematic representation of the L1Calo trigger system. Black arrows show real time data path, and grey arrows show readout data path [37].

The L1Calo consists of three subsystems, namely the preprocessor (PPr), the cluster processor (CP) and the jet/energy-sum processor (JEP). A schematic representation is shown in Figure 5.1. The preprocessor digitizes the signals coming from the trigger towers, extracts a transverse energy(E_T) value and assigns the signal to a particular LHC bunch crossing. The CP identifies clusters of electrons, photons and hadrons. The JEP identifies jet candidates and calculates the global sum E_T as well as missing E_T in the event. The information from these modules are passed to the Central Trigger Processor (CTP). Based on the information from L1Calo and L1Muon the CTP sends a Level-1 accept (L1A) signal. When an L1A signal is received, the region of interests as well as the energy sum information are passed to the Level-2 system. In parallel, trigger-tower energies and processing results are handed over to the data acquisition system. This information can be used to monitor the performance of the trigger system.

5.3 Analog Input

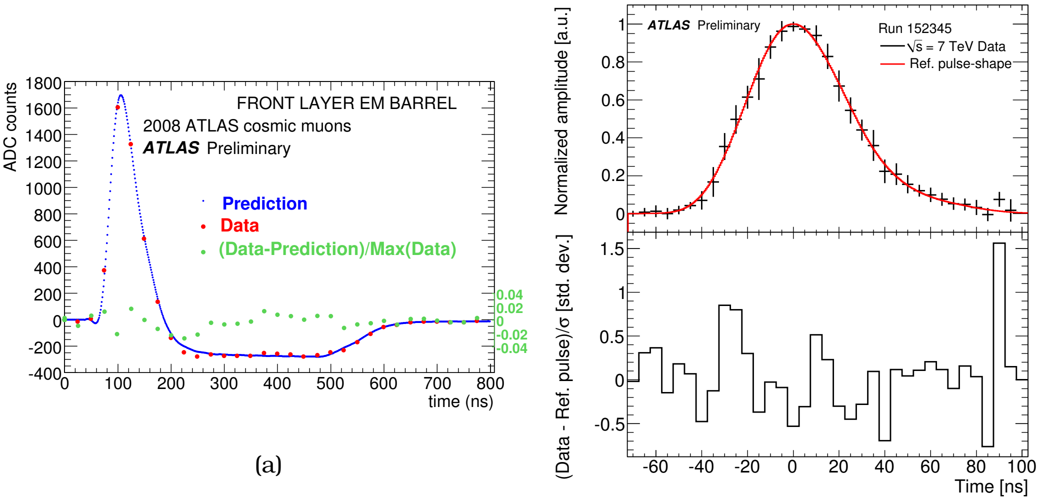

(a)

(b)

Figure 5.2: ATLAS calorimeter pulse shapes (a) LAr and (b) Tile. Notice that the pulse width spans several bunch crossings.

The shape of the signals received from the LAr and Tile Calorimeters are different; see Figure 5.2. In case of the LAr pulses the rise time is less than 1 ns with a linear decay which corresponds to the drift time in the LAr gap. The pulse is amplified at an earlier stage in the front end electronics to make it immune to noise in the subsequent electronics. This pulse is further shaped into a bipolar signal to optimize the signal to noise ratio. The output of the pulse shaper has a rise time of $\sim$50 ns and a long negative undershoot. The positive part of the signal is several bunch cross wide and the area is proportional to the energy deposition in the calorimeter cell.

The pulses from the TileCal Photomultipliers has a rise time $\sim$5.5 ns and a full width at half maximum of $\sim$15 ns. In order to allow for a common processing for the both calorimeter signals in the trigger system, the tile pulses are shaped into a unipolar pulse with a full width at half maximum equal to $\sim$50 ns, similar to the LAr pulses.

The signals from multiple cells are summed up in the front end electronics of the two calorimeter systems to form the so called trigger tower. The trigger towers are adjacent and projective with respect to the interaction point. The number of cells in each trigger tower varies from a few in the endcap to 60 in the barrel region. The granularity of the towers in $\Delta\eta \times \Delta\phi = 0.1 \times 0.1$ for $|\eta| < 2.5$ and coarser at larger pseudorapidities; see Figure 5.3.

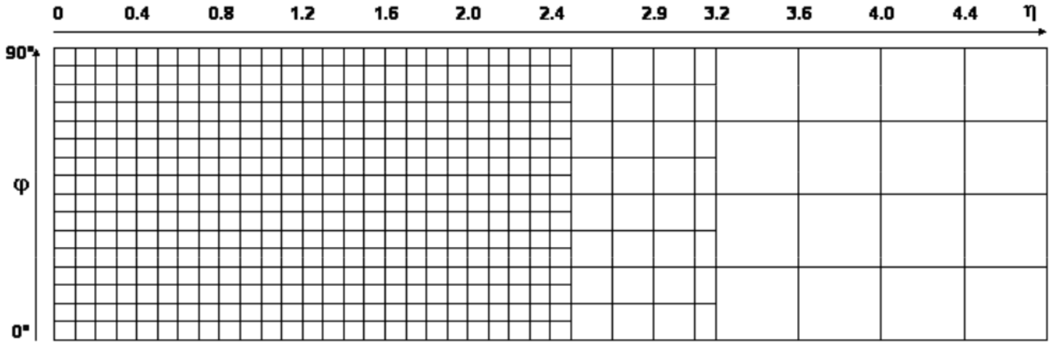

Figure 5.3: Trigger tower granularity in η and ϕ [37].

The trigger tower signals are sent from the detector front end to the electronics cavern differentially through 16 way twisted-pair copper cables of various lengths ranging from 30–70 m. The receiver system of the L1Calo does fine voltage gain adjustments and signal reordering and sends it to the PreProcessor system (PPr).

The signals that reach the PPr are bipolar signals. These are converted to unipolar signals, the amplitudes are adjusted to conform with a digitization window of 1 V. These signals are several bunch crossings wide and they are asynchronous in time due to different time of flight of the particles which are responsible for these signals as well as cables accessing different regions of the detector. Before processing begins the signal has to be digitized. The digitization happens at the LHC bunch cross frequency of 40.8 MHz. After digitization these signals are aligned in time before identifying the bunch crossing as well as calculating E_T.

5.4 Hardware

The description of the hardware follows from [38]. The PPr consists of 124 identical preprocessor modules (PPM). Each of these modules can process 64 trigger tower signals. The PPMs are mounted on 8 crates along with timing units, single board computers as well as optical link transmitter modules. Various units on a PPM is shown in 5.4

The analog input boards condition the signals and send them to 4-channel *Multi-Chip Modules* (PPrMCM), see Figure 5.5 . The PPrMCM stores the event data until a Level-1 Accept signal is received. The *Timing, Trigger and Control Receiver Chip* (TTCrx), decodes the LHC serial protocol signal and places timing information to multiple locations on the PPM.

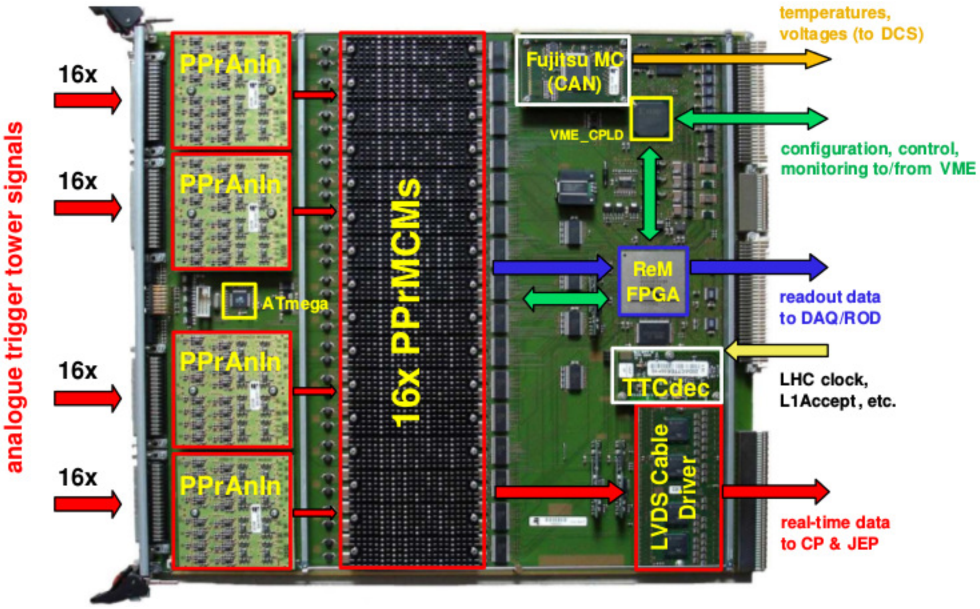

Figure 5.4: The Preprocessor module [38].

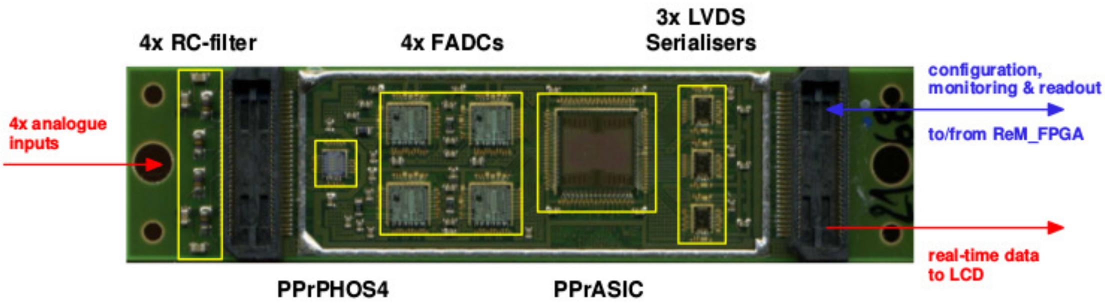

Figure 5.5: PreProcessor Multi-Chip Module: The FADCs convert the analog input signals to digital signals [38].

The PPrMCM's consist of four Flash Analog to Digital Converters (FADCs) to digitise signals, one PHOS4 timing chip (PPrPHOS4) to strobe the FADC's, a custom chip PPrASIC to perform trigger specific data processing and LVDS serializers for transmission of critical data to other units in the L1Calo.

The analog signals that are fed to the PPrMCMs are first passed through a low pass filter to reduce high frequency noise components. The signals are then digitized by the FADCs with 10 bit resolution at the LHC bunch-crossing frequency. The 1 V input voltage range of FADCs correspond to an E_T range of 0–256 GeV deposited in a trigger tower. Thus one FADC count corresponds to ~244 MeV. The maximum size of a pulse is 1023 ADC counts. Signals larger than this value are "saturated signals".

The digitization is driven by PPrPHOS4 chips. The phase of the digitization strobe can be fine tuned within steps of 1 ns resolution so that the peak of the analog signal can be sampled accurately. The phase of the strobe can also be configured for individual chips to facilitate an accurate sampling.

The resulting four 10 bit FADC data streams are then fed to the PPrASIC where trigger specific data processing is carried out. The real time output of the PPrASIC consists of 3 parallel streams, out of which two provides calibrated $\mathrm{E_T}$ values for the Cluster Processor and the third stream provides jet $\mathrm{E_T}$ sums for the Jet Energy Processor.

In the PPrASIC, the FADC signals are first latched with the LHC clock. The latched signals are then delayed by passing through a synchronization First-in-First-Out (FIFO) memory buffer. This is done to align the signal with signals processed in other PPr's.

Fanned out output of the synchronization buffer is then fed to Bunch Crossing Identification (BCID) algorithms.

5.4.1 BCID Algorithms

Associating trigger tower signals to the correct LHC bunch crossing is very important for the trigger logic. Since the LAr pulses as well as the tile calorimeter signals are several bunch crosses wide, this is a challenging task. The trigger must also be efficient for low energy particles which produces low amplitude pusles as well as high energy particles which produces saturated pulses.The PPrASIC employs three methods to cover this large dynamic range. One for unsaturated pulses, another for saturated pulses and a third method that provides a cross check for the first two methods.

The first method uses a finite impulse response (FIR) filter to sharpen the pulse before passing it through a peak finder algorithm. Five consecutive samplings are multiplied with predefined coefficients and summed. The sums of previous, current and the following bunch crossings are compared to find a maximum. The details of other methods can be found in [37].

5.5 Timing

A singal in an L1Calo channel trigger tower is an analogue pulse with an amplitude proportional to the energy deposited. The pulse is sampled every bunch crossing. The shape of the pulse varies slightly depending on the detector region from where it came. The peak of the pulse must be in the center 25 ns bunch crossing sample or slice. Five slices is the approximate width of the pulse, which is the minimum required for optimum energy resolution in the calorimeter readout. If the peak is not in the center slice, then the pulse will not have an associated calibration energy value in the correct bunch crossing and hence it will not be summed within the correct event.

It is essential that the system is well timed in order to achieve the best energy resolution for the trigger. Therefore the peak of the pulse should be sampled.

Timing calibration of a trigger tower so that the peak is in the center slice is known as good “coarse” timing. However, to trigger accurately, the peak of the analogue pulse must be in the middel of the center slice. This is known as good “fine” timing. The aim is to calibrate and maintain every tower within 2 ns of this center. The smallest increment of change on the timing is 1 ns

5.5.1 Pulse Selection

Only “good” pulses are selected for the analysis [39]. Fine time is not calculated if the peak

- is less than the peak threshold,
- is in the first or last sampled slice,
- has adjacent slices equal in size to the peak
- has adjacent slices smaller than pedestal value

The trigger towers are split into partitions as shown in Table 5.1. The trigger towers are coarser than calorimters cells.

The signals from the trigger towers are summed using a sliding window algorithm to determine region of interest to identify electrons/photons, tau’s, hadrons and jets. This information is sent to the Central Trigger Processor (CTP). The CTP sends an L1 accept signal to the data acquisition based on these informations as well as the information from the L1Muon.

The signal digitization in the PPr system can be adjusted for individual trigger towers to synchronize the digitization with the LHC clock frequency. A coarse timing in steps of 25 ns as well as a fine timing in steps of 1 ns, up to 25 ns is possible. Both procedures allow to sample the analogue signal peak correctly at its maximum. This is very crucial since incorrect digitization can influence the results of the BCID

Partition name	Abbreviation	η range
Electromagnetic layer		
Barrel	EMBA/EMBC	$0 < \|\eta\| < 1.4$
Barrel/End-cap overlap	OverlapA/OverlapC	$1.4 < \|\eta\| < 1.5$
Endcap	EMECA/EMECC	$1.5 < \|\eta\| < 3.2$
Forward Calorimeter	LArFCal1A/LArFCal1C	$3.2 < \|\eta\| < 4.9$
Hadronic layer		
Long Barrel	TileA/TileC	$0 < \|\eta\| < 0.9$
Extended Barrel	TileA/TileC	$0.9\|\eta\| < 1.5$
Endcap	HECA/HECC	$1.5 < \|\eta\| < 3.2$
Forward Calorimeter	FCAL23A/FCAL23C	$3.2 < \|\eta\| < 4.9$

Table 5.1: L1Calo partitions: Negative η side is A side and positive η side is C side.

logic as well as the E_{T} sum logic. For a stable and meaningful operation of BCID the sampling of the analogue pulse should be within a precision of ±10 ns. Similarly a timing precision of ±5 ns is needed for energy measurements with less than 2% uncertainty. The signal pulses have been modelled using a Gaus-Landau (GLU) convolution or double Landau function (LLU) for various detector regions and have been calibrated by an earlier effort [40]. Results obtained from the GLU fit for typical L1Calo pulse are shown in Figure 5.6b

There are several factors which may contribute to change in timing. This includes random changes due to electronics, signal transmission problems and problems in the hardware. It has been found that timing shifts occur during the operation of the detector. For instance the thermal expansion of the signal cables due to weather changes causes shifts in timing. Potential electronic noise could also cause deviations from sampling the pulses correctly. Hence the timing behavior of the sampling strobe has to be monitored. The GLU, LLU functions have six free parameters for the fit and it would be computationally expensive for the data acquisition system to do fits for ~7200 L1Calo channels during every bunch crossing. Therefore a simple alternative wad deviced. Instead of fitting, the peak region the pulse described by the central three ADC slices (Figure 5.6a) is approximated using a second order polynomial. Solving for the maxima, the peak position is determined.

We model the signal peak region using a second order polynomial

$$f(x) = ax^2 + bx + c \tag{5.1}$$

This function has a maximum at

$$f_{\max} = \frac{-b}{2a} \tag{5.2}$$

Since the analog signal is sampled at 40.8 MHz the time interval between successive samples is 25 ns. Therefore in our model, the function assumes only discrete values.

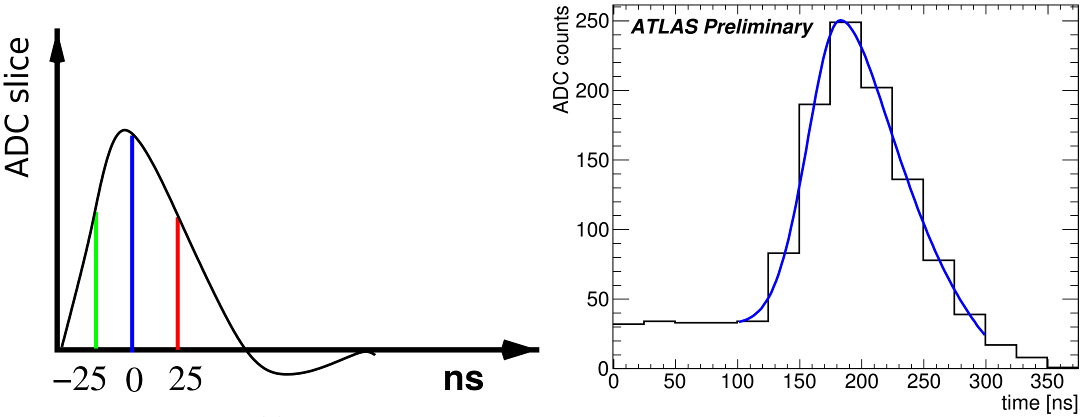

(a)

(b)

Figure 5.6: (a) Schematic representation of signal sampling: The blue line indicates the central slice. Using these three slices and assuming they are described by a parabola the peak position is found. (b) A hybrid Gaus Landau (GLU) function is fit to the signals read out from the L1Calo system.

Adding some boundary conditions namely

$$f(0) = c \tag{5.3}$$

$$f(-25) = 25^2 a - 25b + c \tag{5.4}$$

$$f(25) = 25^2 a + 25b + c \tag{5.5}$$

solving for a and b

$$a = \frac{f(-25) + f(25) - 2f(0)}{2 \times 25^2} \tag{5.6}$$

$$b = \frac{f(25) - f(-25)}{2 \times 25} \tag{5.7}$$

the expression for fine time is obtained.

$$\textbf{FineTime} \equiv f_{\mathrm{max}} = \frac{f(-25) - f(25)}{2[f(-25) + f(25) - 2f(0)]} \times 25 \text{ ns} \tag{5.8}$$

A software package has been written to calculate *FineTime* for all the 7168 L1Calo channels individually. The *FineTime* calculated are filled in histograms specific to individual trigger tower channels as well as different L1Calo partitions. Any anomalies or sudden shifts in *FineTime* is an indication of discrepancy in sampling the peak of the analog pulse, which eventually compromises the performance of the L1Calo system and thus valuable physics information. The monitoring histograms are available as live histograms at the desk of the ATLAS trigger shifter in the ATLAS control

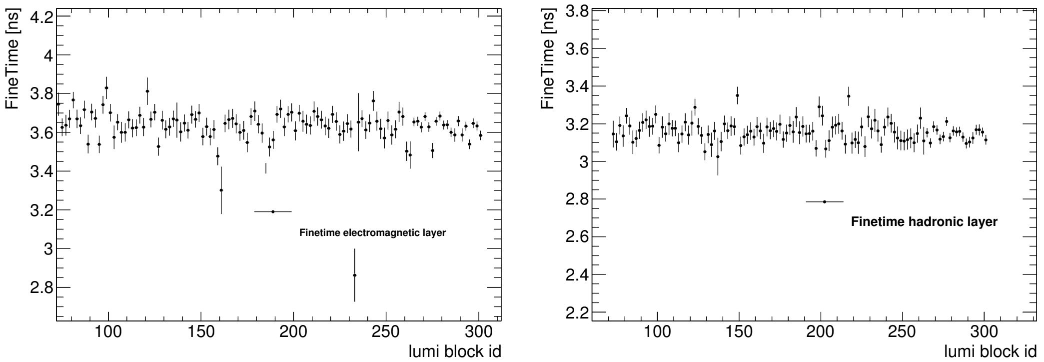

(a) Electromagnetic layer (b) Hadronic layer

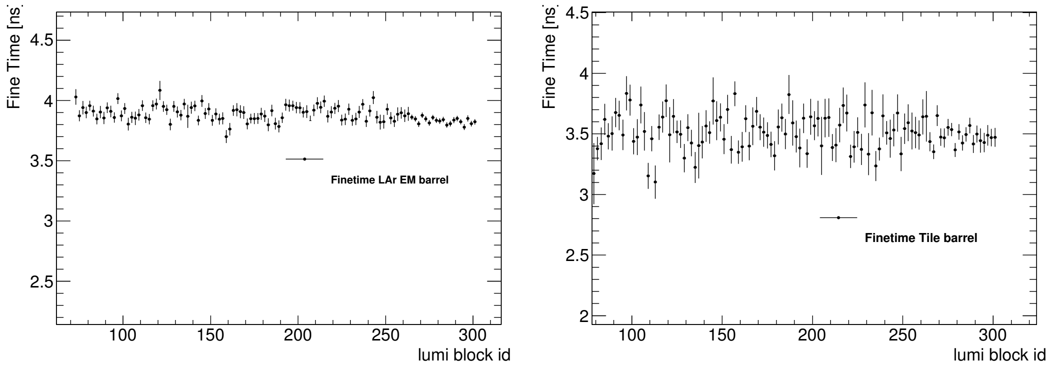

(c) Electromagnetic barrel region (d) Tile barrel region

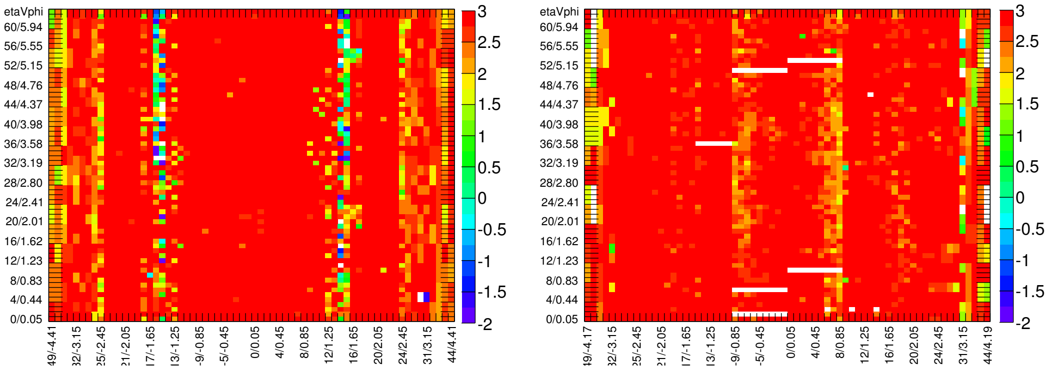

(e) Electromagnetic trigger tower (f) Hadronic trigger tower

Figure 5.7: Average trigger tower fine time. The histograms on the top show average and rms of fine time for the electromagnetic as well as the hadronic layers of the trigger tower. The middle histograms shows average and rms fine time for the barrel region of the electromagnetic as well as the hadronic layers of the trigger tower. Finally average fine time is shown for all the L1Calo channels as an $\eta - \phi$ map. The fluctuations are within the tolerable range of an uncertainty of ±5 ns.

room. In case of an abnormal behavior the shifter can take necessary actions to bring back the system to normalcy or notify the expert concerned. The package also makes *FineTime* histograms available for a detailed analysis later, once the data is stored on disk. Selected sample histograms are shown in Figure 5.7

5.6 Conclusion

A software framework for monitoring fine time shifts has been developed. The software is part of the ATLAS analysis package *Athena*. Monitoring histograms are produced during live data taking. The package also offers the possibility to make FineTime histograms for offline data. The monitoring histograms show that there has been no drastic fine time shifts for the data taking periods.

Chapter 6

Electron Reconstruction

Electrons are primary signatures of electro-weak processes. They are crucial in precision tests of the Standard Model at the LHC. High p_T electrons are signatures of several New Physics searches. An efficient and precise electron identification was one of the main goals of the ATLAS detector design. In this chapter the electron reconstruction and various standard ATLAS identification techniques are reviewed. Throughout this thesis unless otherwise specified electron means both electron and positron.

6.1 Electron Reconstruction

An electron is characterized by a track in the Inner Detector (ID) associated with a narrow cluster of energy deposition in the electromagnetic calorimeter. An event display of lepton + jet event is shown in Figure 6.1. The track reconstructed in the ID points to a very narrow cluster of energy deposition in the electromagnetic calorimeter. There is no activity in the hadronic calorimeter cells behind the clusters in the electromagnetic calorimeter

Electron candidates are reconstructed by associating tracks in the ID with local energy depositions in the electromagnetic calorimeter using a sliding window clustering algorithm [41]. Electron interactions in the calorimeter produce particle showers, which ultimately deposit energy in the calorimeter cells. The algorithm scans the entire η-ϕ space and builds clusters from the cells. The clustering is seeded by a “hot cell” in a small search window of 3 units in η and 5 units in ϕ (1 unit = 0.025 in η and ϕ, which is the cell granularity of the middle layer of the electromagnetic calorimeter). These clusters are required to have a minimum transverse energy of 2.5 GeV.

In the next step, the ID tracks are associated to the clusters. Tracks are extrapolated from the Inner Detector to the second layer of the electromagnetic calorimeter and the differences between η and ϕ coordinates of the cluster and track is calculated. This track–cluster matched candidate is considered to be an electron candidate if

- $\Delta\eta_{\text{calo-track}} < 0.05$,

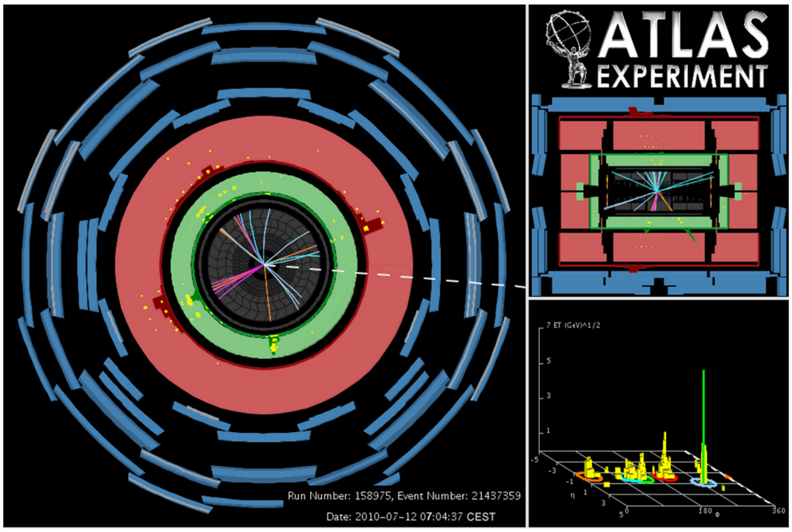

Figure 6.1: An event display of an electron plus jet candidate. The downward pointing orange track with an associated green cluster is the electron candidate.

- $\Delta\phi_{\text{calo-track}} < 0.1$,

where $\Delta\eta_{\text{calo-track}}$ and $\Delta\phi_{\text{calo-track}}$ are the η and ϕ difference between the respective coordinates of the clusters bary-center and the extrapolated track.

Particles which lose energy due to bremstrahlung in the inner detector bend stronger in ϕ than naively expected. Therefore the cut in ϕ is loosened to 0.1 to take care of these electron candidates. If more than one track satisfy these matching criteria, then the one which has the lower ΔR value is chosen.

The total material in the active region of the inner detector $|\eta| < 2.5$ is roughly 50% of X_0. This means that the electron could potentially lose a significant fraction of its energy due to bremsstrahlung before reaching the calorimeter. However these radiated photons reaching the calorimeter are contained in the calorimeter volume closely associated to the electron clusters. This makes it possible to recover some of the bremstrahlung losses in case the electron is not undergoing hard bremsstrahlung. For the data taking period of 2012, an additional track reconstruction algorithm was used which accounts for these bremstrahlung losses. Tracks associated with the seed clusters are refitted using a Gaussian Sum Filter (GSF) algorithm [43].

After the track matching, the seed clusters are rebuilt, the cluster size is enlarged to 3×7 in $\eta - \phi$ in the central barrel region and 5×5 in the end-cap region. The total energy of the electron is determined from 4 components [44]:

- The energy measured in the cluster.

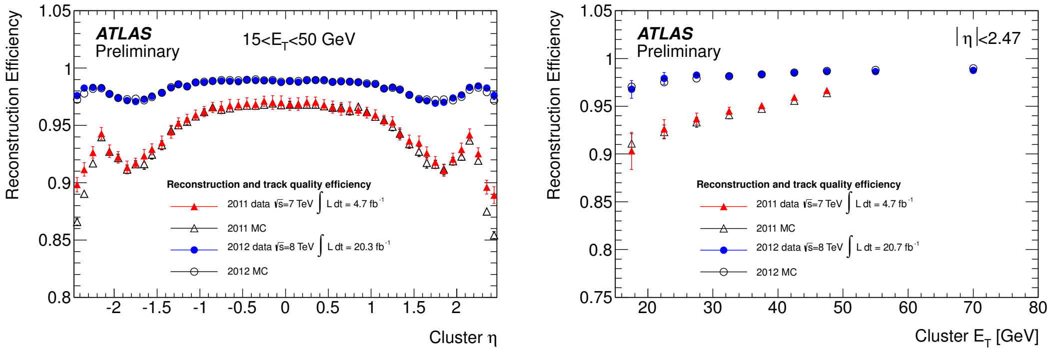

Figure 6.2: Electron reconstruction efficiency as a function of (a) cluster η and (b) cluster E_{T}. The red curve represent 2011 data and the blue curve represent 2012 data [42].

- The estimated energy loss before the electron reaches the calorimeter.
- The estimated energy loss laterally outside the calorimeter.
- The estimated energy loss leaked in the longitudinal direction in the calorimeter.

The electron candidates at this stage of reconstruction are referred to as “container electrons”. The efficiency to find electron candidates with this method is shown in Figure 6.2. The use of GSF algorithms has significantly improved the electron candidate reconstruction efficiency.

Apart from prompt electrons, reconstructed electron candidates also consist of hadrons, conversion electrons, electrons from π^0 decays and semileptonic decays of heavy flavor particles. In the following electron identification for prompt isolated electrons is described. Development of a method for identifying electrons from heavy-flavor decays is described in chapter 7

6.2 Electron Trigger

Isolated electrons like those coming from Z-boson decays provide a clean trigger signals in the calorimeter. At L1, electron candidates are selected by requiring electromagnetic trigger towers to exceed an E_T threshold. In order to reduce hadronic fakes a hadronic veto is also applied to L1 electron triggers. True electrons are expected to deposit only a small amount of energy in the hadronic calorimeter behind the electron cluster. The L1 electron trigger defines a region of interest which acts as a seed for electron reconstruction in HLT. Offline electron reconstruction algorithms are available at this level to identify electrons.

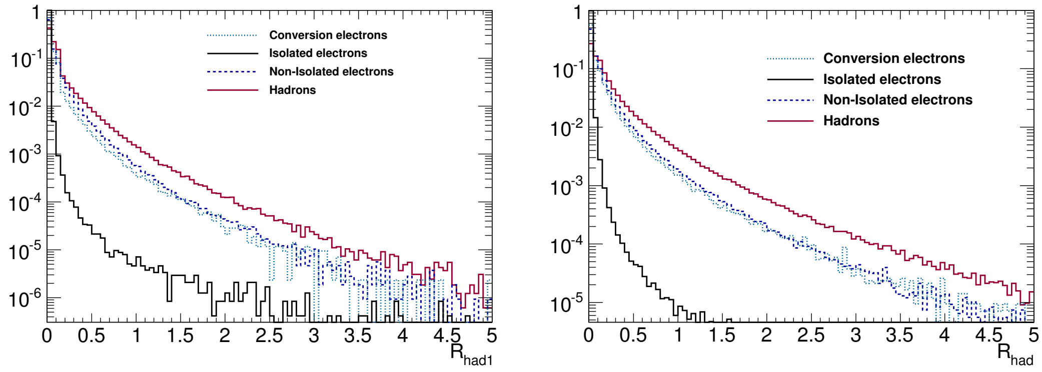

(a)

(b)

Figure 6.3: Energy leakage into the hadronic calorimeter parameterized as (a) R_{had1} : Ratio of energy deposited in the first layer of the hadronic calorimeter to the energy deposited in the electron cluster (b)R_{had} : Ratio of energy deposited in all hadronic layers to the energy deposited in the electron cluster.

Two categories of electron triggers exist, primary trigger and supporting trigger. Primary triggers are un-prescaled triggers which employ strict particle identification criteria. They are used in physics analysis. The supporting triggers select electrons based on the E_T cuts without any identification criteria. Thus they offer a very unbiased electron candidate sample which can be used for performance studies. Since they do not use any identification criteria, the rates are high and hence supporting triggers are heavily prescaled.

6.3 Electron Variables

Prompt decays of W and Z bosons produce largely isolated electrons. However, electrons coming from the decay of heavy flavor particles like B-hadrons and D-mesons are not so well isolated, because they are produced in association with jets. There is no inclusive way of identifying both the isolated and non-isolated components. Most of the effort in ATLAS is concentrated on optimizing the identification of isolated prompt electrons for searches or identifying vector bosons

The separation between real electrons and background can be achieved by using variables measured in the calorimeter as well as in the Inner Detector that can be used to identify electrons.

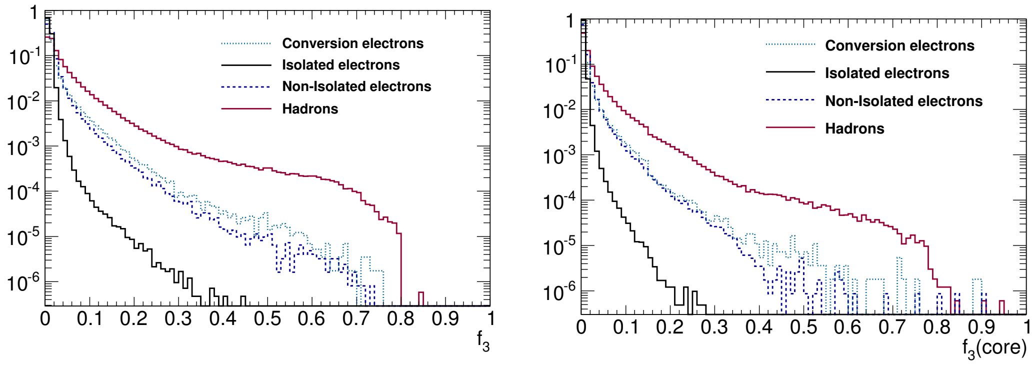

Figure 6.4: Discriminating variables sensitive to the electron energy deposition in the third layer of the electromagnetic calorimeter.

6.3.1 Calorimeter Variables

The electromagnetic calorimeter has three layers with fine segmentation in η and ϕ. The response of the electromagnetic calorimeter to incident particles is parameterised using "shower shape variables".

Electromagnetic calorimeter activity related to the electrons are predominantly contained within its volume without any significant leakage into the hadronic calorimeter behind the electron cluster. If there is more activity in the hadronic calorimeter cells directly behind the electron cluster the candidate is less likely to be an electron.

The variable $R_{\text{had}1}$ is defined as the ratio of the energy deposited in the first layer of the hadronic calorimeter behind the electron cluster to the energy deposited in the electron candidate cluster, which can separate true electrons from hadrons. $R_{\text{had}1}$ distributions for different categories of electron candidates are shown in Figure 6.3. Large values of $R_{\text{had}1}$ indicates hadronic activity associated to the cluster. In the transition region between the barrel and end-cap of the hadronic calorimeter ($0.8 < |\eta| < 1.37$), the hadronic leakage is calculated using all layers of the hadronic calorimeter denoted by a new variable R_{had}.

Since the electron showers are more likely to be contained within the volume of the electromagnetic calorimeter, the electromagnetic shower develops in the first sampling layer, increases the shower activity in the second layer and dies out in the third sampling layer. Thus true electrons deposit usually less energy in the third sampling layer. The ratio of energy deposited in the third sampling layer to the total energy of the electron cluster could be another potential discriminating variable to separate electrons from hadrons. Two different parameterizations are available for this

$$f_3 = \frac{E_3}{E}, \qquad \text{and} \qquad f_3(\text{core}) = \frac{E_3(\text{core})}{E},$$

where E_3 is the cluster energy deposited in the third sampling layer and $E_3(\text{core})$

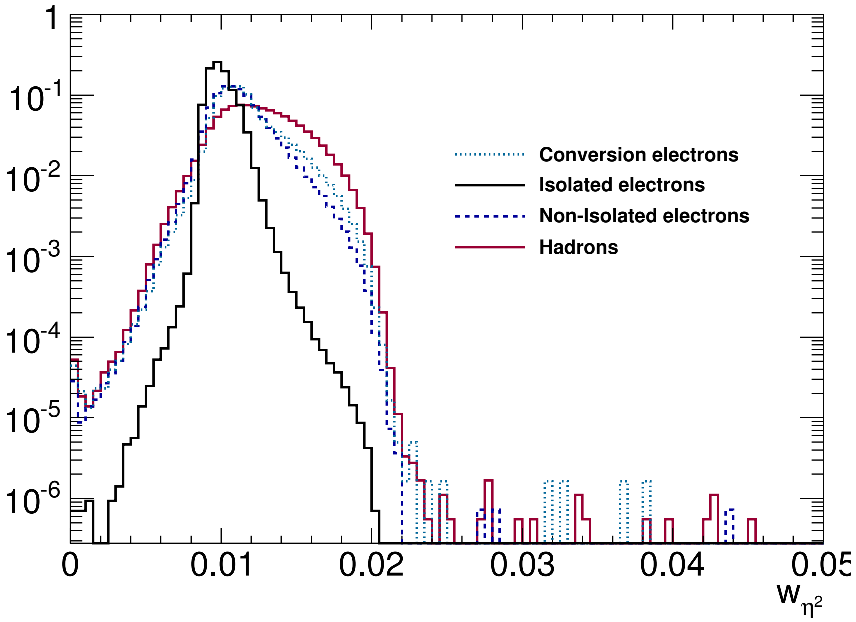

Figure 6.5: The shower width measured as the RMS of the η distribution of the cells in the second sampling layer. Isolated electrons have a narrow profile.

is the energy deposited in the core region (corresponds to 3×3 cells in $\eta - \varphi$) of the calorimeter cluster. In regions with lot of activity the E_3(core) variables are expected to show better discrimination. The distributions are shown in Figure 6.4. As expected at higher f_3(core) values hadron contributions are dominant compared to electrons. Although non isolated electrons have low energy compared to prompt electrons, their f_3(core) values tend to be harder compared to the prompt electrons. This is due to the high calorimeter activity around a non isolated electron.

The shower width in the second sampling layer can be parameterised in three independent variables. $w_{\eta 2}$ shown in Figure 6.5, measures the width as energy weighted root mean square of the η distribution in the cells of the second sampling layer. It is defined as

$$w_{\eta^2} = \sqrt{\frac{\sum_i E_i \eta_i^2}{\sum_i E_i} - \left(\frac{\sum_i E_i \eta_i}{\sum_i E_i}\right)},$$

where the index i runs over the 3×5 cells window of the second sampling layer, around the electron cluster bari-center.

R_η and R_φ are the other two variables which measure the shower width in the second sampling layer. R_η is defined as the ratio of energy deposited in the 3×7 cells in $\eta - \varphi$ to the energy deposited in 7×7 cells in $\eta - \varphi$ in the second layer of the electromagnetic calorimeter. Similarly R_φ is defined as the ratio of energy deposited in the 3×3 cells in $\eta - \varphi$ cells in $\eta - \varphi$ to the energy deposited in the 3×7 cells in

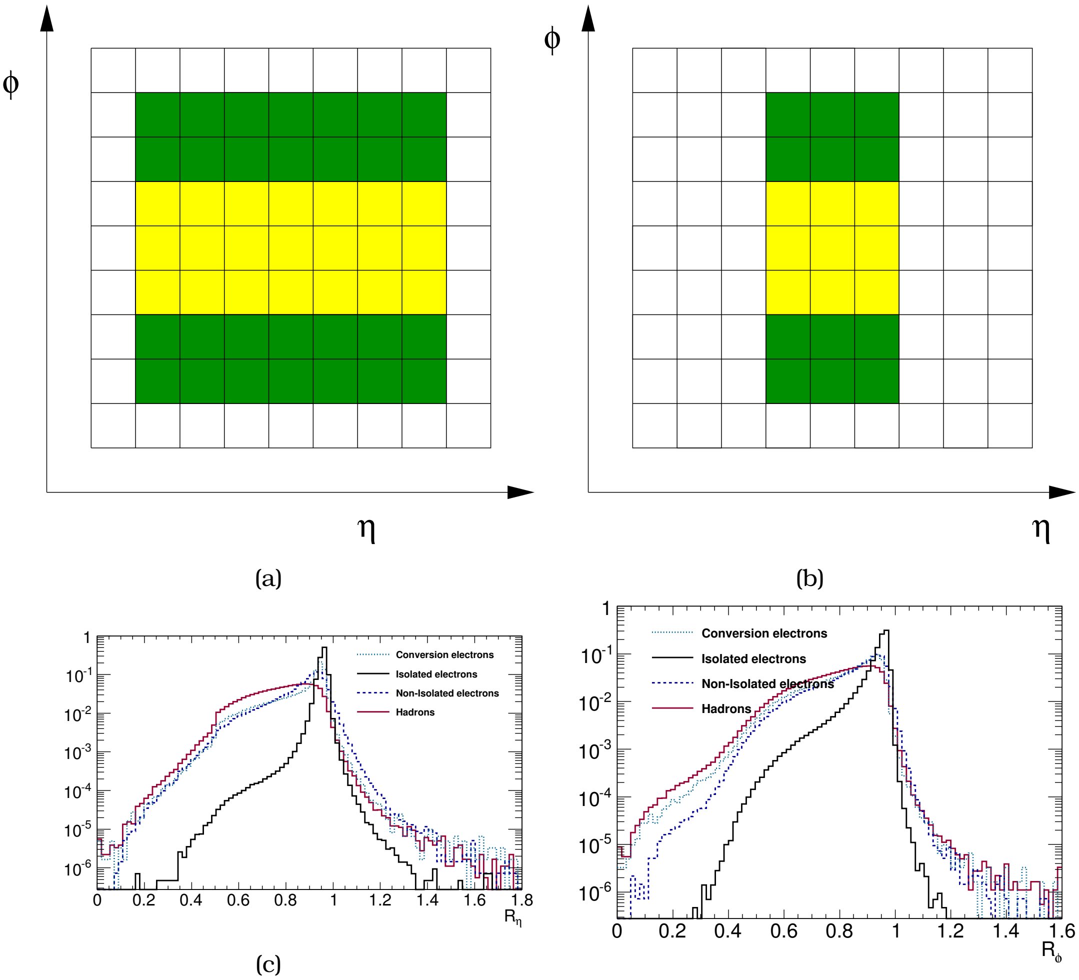

(a) (b)

(c) (d)

Figure 6.6: Schematic representation of (a) R_η and (b) R_φ. Both variables represents ratio energies deposited in a group of calorimeter cells. Energy deposited in yellow regions are numerators and green regions are the denominators in the ratios. The distributions for respective variables are shown in (c) and (d). Isolated electrons have a narrow profile in both variables.

$\eta - \varphi$ in $\eta - \varphi$ in the second sampling layer.

$$R_\eta = \frac{E_{(3\times7)}}{E_{(7\times7)}} \qquad \text{and} \qquad R_\varphi = \frac{E_{(3\times3)}}{E_{(3\times7)}},$$

where $E_{(3\times7)}$ is the energy deposited in 3×7 cells in $\eta - \varphi$ of and $E_{(7\times7)}$ is the energy deposition in 7×7 cells in $\eta - \varphi$ of the second sampling layer. A schematic representation as well as variable distribution is shown in Figure 6.6.

The first layer of the electromagnetic calorimeter has the highest granularity among

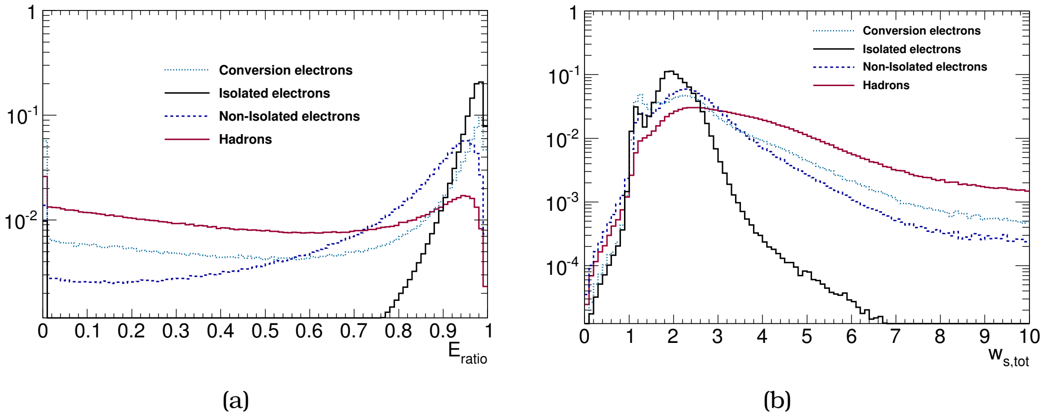

(a)

(b)

Figure 6.7: (a) E_{ratio} and (b) $w_{\text{s,tot}}$ shower shape variables in the first layer of electromagnetic calorimeter or the first layer.

all three layers. Therefore the lateral development of the shower can be reconstructed more precisely there.

The variable E_{ratio}, defined as

$$E_{ratio} = \frac{E^s_{1^{st}max} - E^s_{2^{nd}max}}{E^s_{1^{st}max} + E^s_{2^{nd}max}},$$

where $E^s_{1^{st}max}$ is the first maximum and $E^s_{2^{nd}max}$ is the second maximum energy deposition in the strip layer. This variable is sensitive to the difference of the first and second maximum energy deposition in the strip layer. Objects like jets have multiple particles associated to the same cluster. The energy deposited by these particles in the strip layer tend to be more or less equal, hence a difference in first and second maximum energy deposition would be less. However this is not expected for a true electron as it can be seen in Figure 6.7a.

The width of the shower in the first sampling layer or the strip layer is another variable which can separate electrons from background. The variable is parameterised as

$$w_{s,tot} = \sqrt{\frac{\sum_i E_i(i - i_{max})^2}{\sum_i E_i}} \tag{6.1}$$

The distribution is show in Figure 6.7b

where E_i is the energy in the i^{th} strip, i is the strip index, and i^{max} is the index of the strip with the most energy. The sums runs over 20×2 strips in $\eta \times \phi$ around the cluster center.

Low energy electrons doesn't have much shower activity as high energy electrons. Hence they lose energies predominantly in the first layer of the electromagnetic calorimeter. Two variables which exploit this feature are shown in Figure 6.8. The

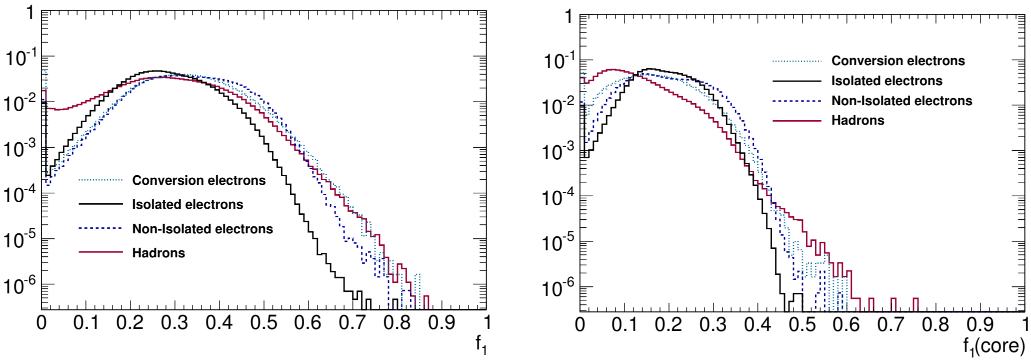

(a) (b)

Figure 6.8: (a) f_1 and (b) f_1(core) distributions. The ratio of energy deposition in the first layer to the total cluster energy and the ratio of energy deposition in the core region of the cluster in the first layer to the total cluster energy respectively.

variables are defined as the following.

$$f_1 = \frac{E_3}{E}, \qquad \text{and} \qquad f_1(\text{core}) = \frac{E_3(\text{core})}{E},$$

where E_3 is the cluster energy deposited in the third sampling layer and $E(\text{core})_3$ is the energy deposited in the core region (corresponds to 3×3 cells in $\eta - \phi$) of the calorimeter cluster.

6.3.2 Inner Detector Variables

One of the main background to real electrons is the photon conversion background. The cross section for pair production is high while energetic photons interact with matter. Since the distribution of material increases upstream and the pixel and strip detectors are thin silicon technologies, the pair production probability is much smaller in the inner detector. Therefore pixel and strip layer hit requirements for electron candidate tracks reduce the conversion background greatly without compromising the signal efficiency. Of particular interest is the hits in the first pixel layer or b-layer. The only material before this layer is the beam pipe. A b-layer hit requirement is the most sensitive variable against photon conversions. The hit distributions are shown in Figure 6.9.

The transverse impact parameter distribution d_0 (Figure 6.10a) is a measure of the distance of the closest approach of the electron track to the primary vertex. Prompt electrons tends to have a smaller value for d_0 than conversion electrons which are produced in the material upstream. Since long lived B-hadrons have a displaced secondary vertex heavy-flavor decay electrons also have large impact parameter values. However, it tends to be smaller than that of conversion electrons.

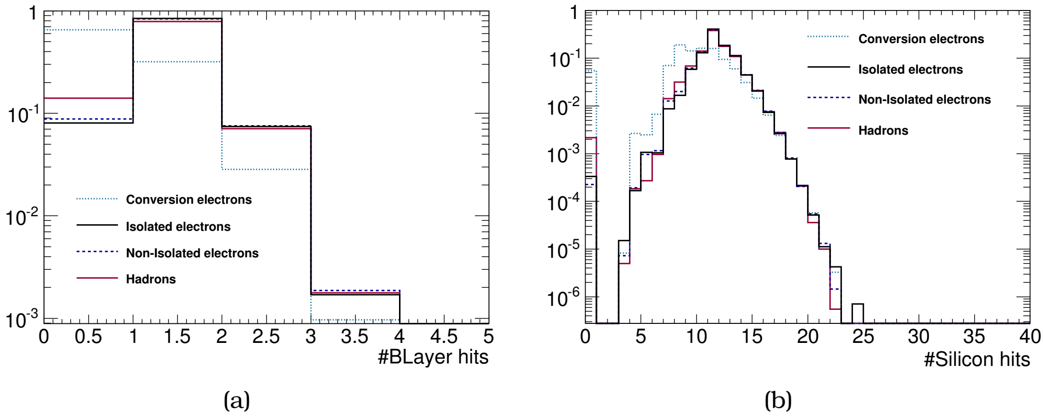

Figure 6.9: (a) number of b-layer hits and (b) number of hits in pixel layer and SCT in total.

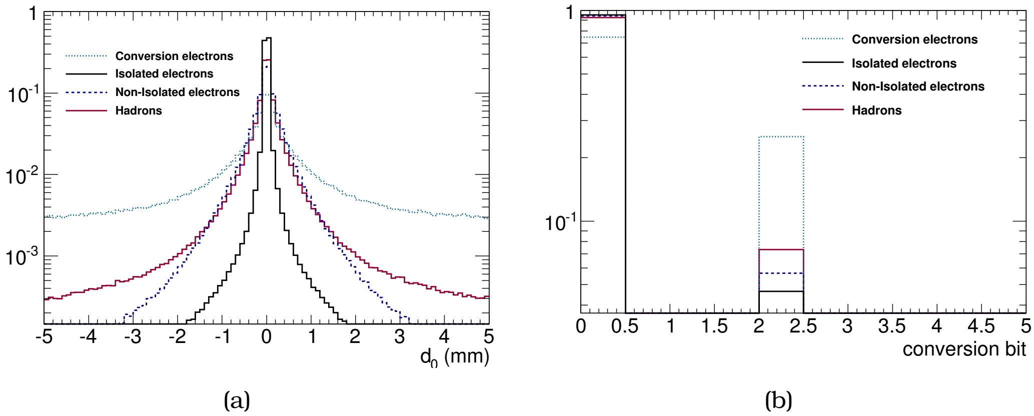

Figure 6.10: (a) Transverse impact parameter, d_0 distribution and (b) Conversion bit distribution. 0 indicates no conversions and 2 indicates 2 leg conversions.

A conversion finder algorithm is used to find the electron candidates originating from the photon conversions in the ID. To each electron candidate the algorithm assigns conversion bits one out of possible three. If the algorithm failed to identify the electron candidate as a conversion electron, then a bit 0 is set. Photon conversions produce pair of opposite charged electrons. However, sometimes one of the electrons could be outside the detector acceptance, leaving the other lone pair within the active region of the detector. To account for these types of conversion electrons the algorithm flags all candidates which doesn't have a b-layer hit as single leg conversion electron and a conversion bit value of 1 is set. In case of double leg conversions where the two conversion electron candidates propagate through the active detector volume, all kinematic properties of photon conversions are used. The

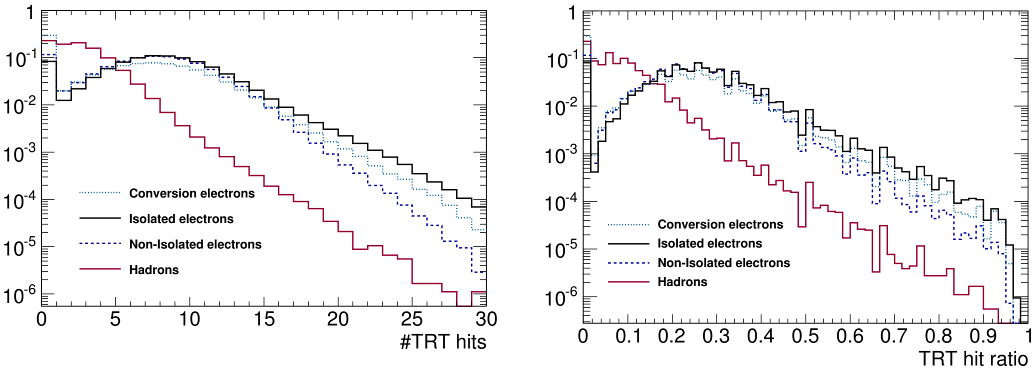

Figure 6.11: (a) Number of TRT hits and (b) TRT high threshold hit fraction. Being heavier hadrons doesn't produce transition radiation photons as much as electrons.

two electron candidates are required to be oppositely charged, with a small opening angle between their tracks. Since conversion photons have a common vertex, vertex of the di-electron system is required to match with the material geometry in the ID. Figure 6.10b shows conversion bit distribution of various electron candidates. A conversion bit requirement of 0, ie. no conversion, removes a significant fraction of conversion background without compromising much on the efficiency for non converted electrons.

When a charged particles passes through the Transition Radiation Tracker (TRT), transition radiation photons are produced. The transition radiation produced is proportional to the Lorentz γ factor ($\gamma = E/m$). For a given energy massive particles have a low gamma factor. Thus massive charged particles like pions and other hadrons tend to produce less transition radiation. The transition radiation photons ionize the gas. The ionization charges are collected and registered as a hit. The hits are classified as high threshold hits and low threshold hits corresponding to 6 keV and 300 eV transition radiation photon energies respectively [45]. The distribution of number of TRT hits and TRT high threshold hit fraction is shown in Figure 6.11. For hadrons, the fraction of high threshold TRT hits peak at lower values in contrast to electrons. Therefore this fraction can be used as a good discriminant to separate electrons from hadrons.

6.4 Combination of Track and Cluster Variables

As it can be seen from the distributions, the calorimeter variables are sensitive to E_T and η. The shower shape development is a function of E_T, high energy particles tend to have narrower shower profiles. Isolated electron identification tends to improve as one goes high in E_T. The η dependence is mainly due to the projective geometry of

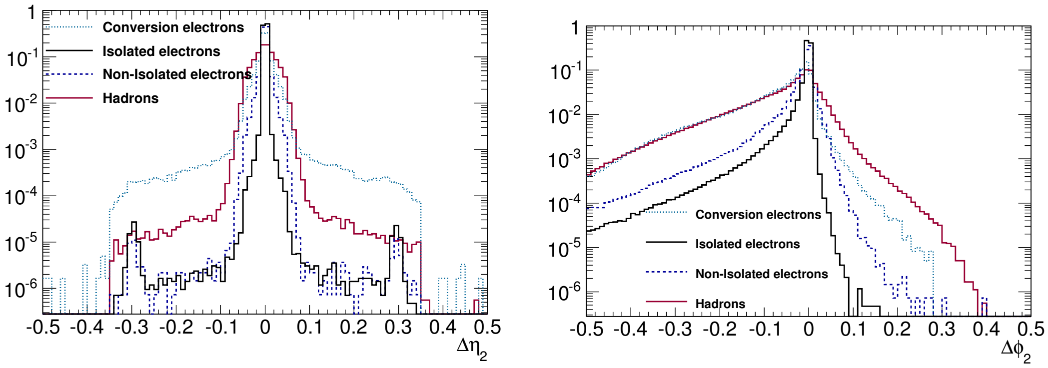

(a) (b)

Figure 6.12: Inner Detector tracks are extrapolated to the calorimeter. The distribution (a) shows the offset of η measured in the tracker and the cluster φ measure in the strip layer of the calorimeter. Distribution (b) shows the offset in tracker φ and cluster φ reconstructed in the second layer of the calorimeter.

the calorimeter. The region $1.37 < |\eta| < 1.52$ is called crack region where a transition between barrel calorimeter to end-cap calorimeter happens. Since the background rejection in this region is very poor due to the presence of additional material, the region is excluded from physics analysis.

The inner detector variables are however largely independent of electron η and E_T except for the TRT. The TRT response is dependant on η because of the different material used in the barrel and end-caps. Since the readout frames of the ID are in nano seconds range it is immune to pileup.

Combination of ID and calorimeter provides additional discrimination power. Tracks reconstructed in the ID can be extrapolated to the calorimeter and compared to the cluster position. $\Delta\eta$, the difference between the track and cluster eta tends to be less for real electrons. Other charged particles that can be produced in association with hadrons and conversion electrons can cause a shift in the cluster η position.

$\Delta\varphi$ reflects the track cluster matching in φ. Bremsstrahlung losses reduces the energy of the charge particle. In the solenoidal field these tracks curve more than expected, hence the $\Delta\varphi$ distribution would be more broader than $\Delta\eta$ distribution. Both distributions are shown in Figure 6.12. The distributions are broader for both hadrons and conversion electrons. In case of hadrons this happens due to calorimeter activity in the neighboring cells. The conversion electrons are produced through photon interactions in the ID material. The average ID hit per conversion electron is less compared to real electrons (Figure 6.9). The broad tails of conversion electrons in $\Delta\eta_2$ and $\Delta\varphi_2$ distributions arise due to the imprecise track measurement in the ID.

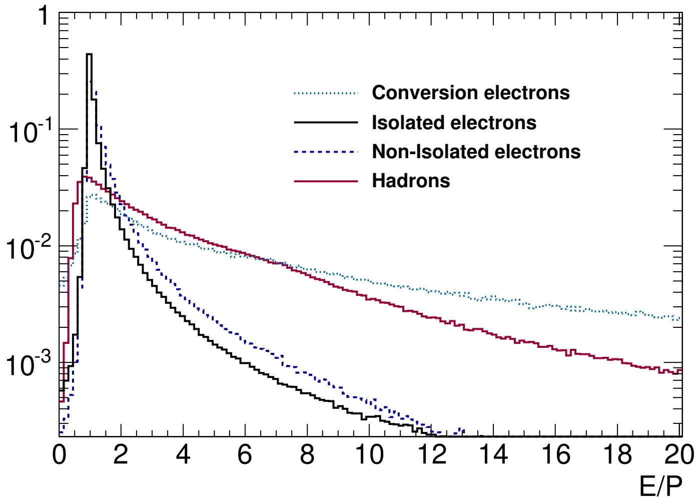

Figure 6.13: The ratio of energy reconstructed in the calorimeter to the momentum measured in the ID. Real electrons show a peak at 1 since the energy deposited in calorimeter and the momentum reconstructed in the ID are comparable. The long tails are due to bremsstrahlung losses.

Another variable that can be used is the ratio of the energy reconstructed in the electromagnetic calorimeter to the momentum measured by the ID. In the ideal case, in the absence of bremstrahlung the energy reconstructed by the tracker and the calorimeter should be the same and the ratio should be 1. But in reality, due to the presence of ID and the electron energy is not fully reconstructed by the ID. The hadrons do not deposit their energy fully in the electromagnetic calorimeter. In the E/P distribution (Figure 6.13) hadrons tend to peak at low values, real electrons peak at 1 with a long tail due to bremstrahlung losses. Conversion electrons are emitted collinear hence both electrons happen to end up in the same cluster, giving a large value for E/P.

Another class of variables called isolation variables can be used to discriminate between signal and background. Isolation is a measure of the activity of energetic particles around the electron candidate. Isolation is calculated by adding energy in a cone centered around the electron. The cone size can be 0.2, 0.3 or 0.4 units in η-ϕ space. There are two classes of isolation variables. The one which is calculated with the energy deposited in the calorimeter and the other which is calculated with the energy measured in the inner detector. Figure 6.14 shows $\mathrm{E}_T^{\mathrm{cone}}(0.3)/\mathrm{E}_T$ and $\mathrm{p}_{\mathrm{T}}^{\mathrm{cone}}(0.3)/\mathrm{p}_{\mathrm{T}}$ calorimeter and tracker isolation variables respectively. Hadrons and heavy-flavor electrons are produced in association with the other particles, hence they tend to have larger value of isolation compared to prompt electrons.

Since the calorimeter measures the energy of neutral particles as well, calorimeter based isolation variables are more sensitive to particle activity than tracker based iso-

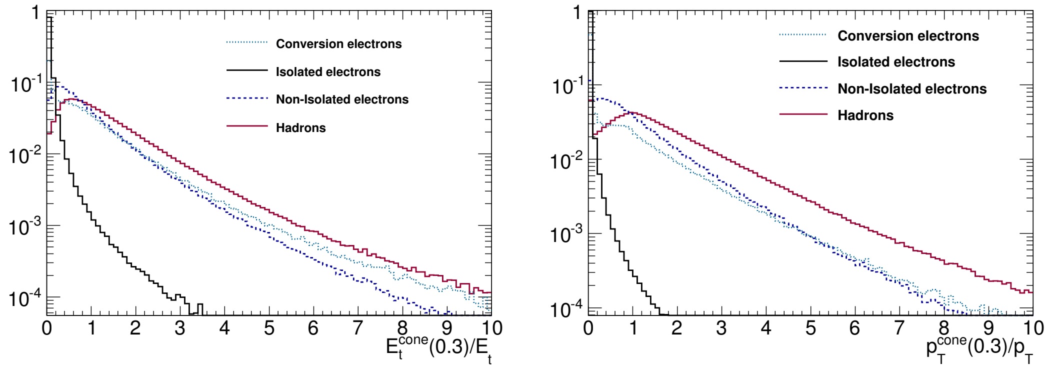

(a) (b)

Figure 6.14: (a) Calorimeter isolation $E_T^{cone}(0.3)/E_T$ and (b) Tracker isolation variable $p_T^{cone}(0.3)/p_T$ showing separation between electrons and hadrons.

lation. However the tracker based isolation is less sensitive to pileup effects. Hence the tracker and calorimeter based isolation variables are more or less complimentary.

6.5 Standard Electron Operating points

Many physics analysis which are looking for electrons has a prompt, isolated high p_T electrons in the final state. A set of cuts are applied on the electron discrimination variables in order to achieve a sufficient purity and efficiency. These cut values are standardised in ATLAS which allows for the central handling of efficiency and systematics determination.

In order to satisfy a broad range of physics requirements three menus of electron operating points are defined namely *Loose*, *Medium* and *Tight* in the increasing order of electron purity.

Among the discriminating variables described above, the isolation variables are not used in the menu. The isolation variables uses a large detector region (up to 0.4 in R). This requirement many not be universally optimal for all physics analysis. Depending on the physics case, individual analysis may select an optimal isolation cut.

The cut values are tightened more and more in each menu. The menu was optimized using background PDFs obtained from data. Signal PDFs were obtained from Monte Carlo and data driven corrections were applied. The cut values in the cut menu were determined by the trigger requirements. At an instantaneous luminosity of $10^{33}\,\mathrm{cm}^{-2}\,\mathrm{s}^{-1}$, the *Medium* operating point would correspond to a single electron trigger rate of 20 Hz for 20 GeV electrons. The *Loose* and *Tight* menu were set with respect to the *Medium* operating point. The *Loose* menu is obtained by relaxing the cuts in *Medium* to give a 95% signal efficiency. Likewise the *Tight* menu is obtained

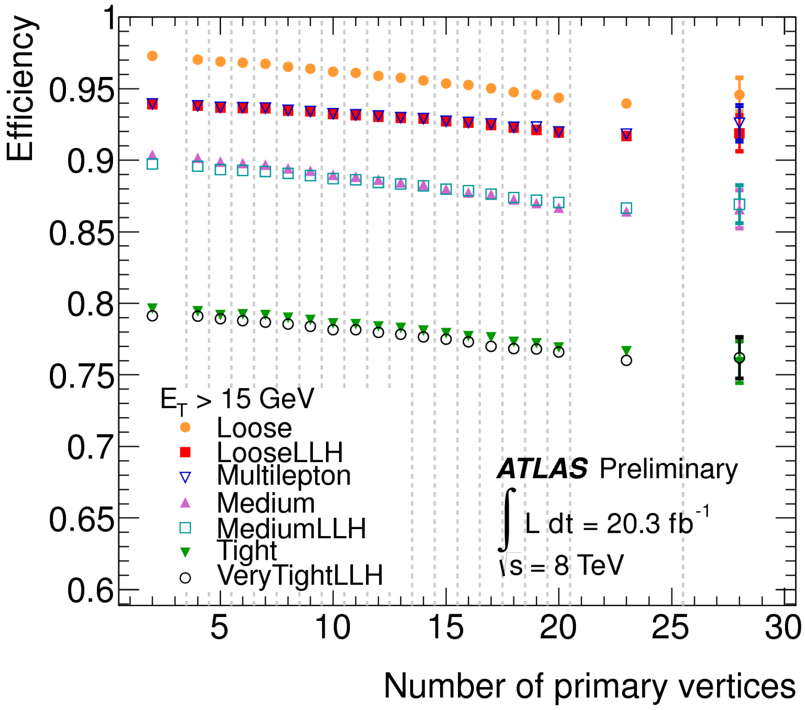

Figure 6.15: Measured reconstruction efficiency for various electron selection menus, as a function of number of primary vertices. The menus are relatively stable to pileup [42].

by tightening the cuts in the *Medium* menu to give a signal efficiency of 75%. In addition to these *Multilepton* menu was also defined, which is optimized for low energy electron selection in the $H \rightarrow ZZ^* \rightarrow 4l$ analysis. The *multilepton* menu has a similar efficiency as the *Loose* menu but a better background rejection.

During the 2012 data taking period the instantaneous luminosity of the LHC was quite high compared to the 2011 data run. Due to this increased luminosity, the average interactions per bunch crossing almost doubled. Certain optimizations were added to the cut menu to make it less susceptible to pileup. The pileup stability of the operating points are shown in Figure 6.15. The Z-boson reconstruction part of this thesis was performed with this improved pileup stable cuts menu. The electron variables used in the menu are described in Table 6.1.

6.6 Conclusion

Using the ID and calorimeter variables, electron identification capabilities of ATLAS have been demonstrated. Several standard working points which are optimized for the selection of isolated electrons have been described. However heavy flavor decay

Name	*loose*	*medium*	*tight*	*multilepton*
$R_{\mathrm{had\,1}}$	✓	✓	✓	✓
f_3		✓	✓	✓
W_{η^2}	✓	✓	✓	✓
R_η	✓	✓	✓	✓
R_ϕ				
$w_{s,tot}$	✓	✓	✓	✓
E_{ratio}	✓	✓	✓	✓
f_1				
f_1(core)				
n_{Blayer}		✓	✓	✓
n_{Pixel}	✓	✓	✓	✓
n_{Si}	✓	✓	✓	✓
n_{TRT}		✓	✓	✓
f_{HT}		✓	✓	✓
d_0		✓	✓	
σ_{d_0}				
$\Delta P/P$				
$\Delta\phi_{\mathrm{res}}$				
$\Delta\eta 1$	✓	✓	✓	✓
$\Delta\phi 2$				✓
E/p			✓	
convBit			✓	

Table 6.1: Variables used in various electron cut menus. The *loose* uses only a minimum set of variables while the *medium*, *tight* and *multilepton* menus use a host of variables.

electron or soft electron identification is not optimized in this identification scheme. A method to identify soft electrons is described in the following chapter.

Chapter 7

Soft Electron Identification

The standard menu for electron identification described in the previous chapter is optimized for prompt and isolated electron selection. In this chapter, the development, validation and performance of a soft electron tagger for the identification of B-hadron decay electrons is described.

7.1 Motivation

The work presented in this thesis is related to finding events with a Z boson and b and a $\bar{b}$ quark pair in the final state. The b-quarks produced in the hard process undergo parton shower until a cut off energy scale is reached. The partons then hadronize and form B-hadrons. Due to the nature of b-quark fragmentation, the B-hadrons produced in the hadronization process have high $\mathrm{p_T}$. They are long lived particles which decay with a displaced secondary vertex. These secondary vertices are typical signatures of b-quark final states in a jet. There exist algorithms which either explicitly reconstruct displaced secondary vertices inside the jet or applies cuts on the impact parameter of tracks associated to the candidate jets to identify b-quark jets or b-jets. However, the uncertainties on b-jet tagging ranges from 6 to 8% as shown in Figure 7.1. In addition to this, jet energy scale uncertainties contribute in precision measurements. The energy scale uncertainties involved in electron reconstruction and identification are lesser than this [46]

The standard electron identification procedure used in many ATLAS analysis (Table 6.1) is optimized for identifying high $\mathrm{p_T}$ isolated electrons. Identifying low $\mathrm{p_T}$ or "soft" electrons which are the decay products of B-hadrons which in turn are the final state products of the hard scattering process is the main focus of this thesis.

Identifying soft electrons in a busy environment of jets is a challenging task. The hadrons and electrons tend to overlap in the jet and as a result, the characteristic shapes of electron discriminating variables are distorted. However, it is possible to identify these soft electrons by exploiting the capabilities of the inner detector as well as the granularity of the electromagnetic calorimeter.

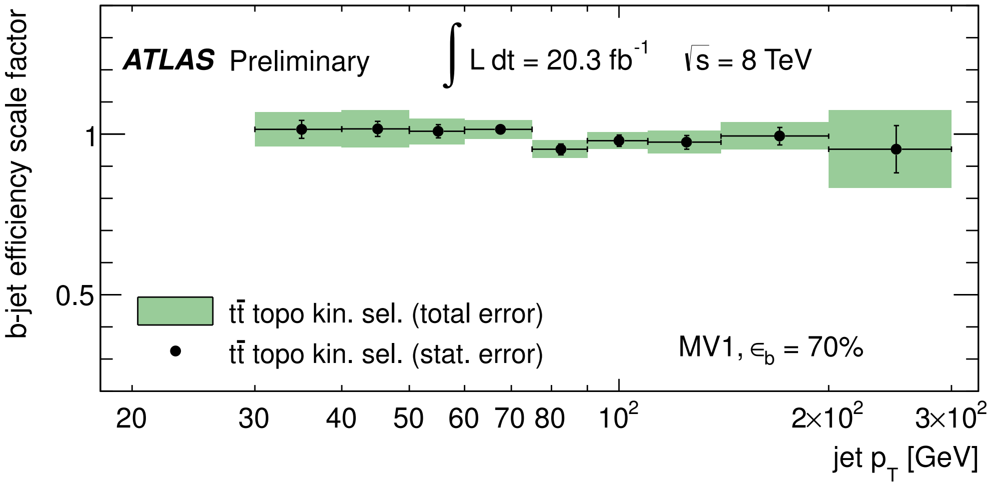

Figure 7.1: B-tagging efficiency scale factor and uncertainties shown as a function of jet p_T for the MV1 b-jet tagger. The uncertainties on the scale factors range from 6% to 8% [47].

7.2 Signal and background samples

The Monte Carlo samples used in this study contain events with electrons in jets from Z-boson associated production $pp \to Z + b\bar{b}$, $pp \to Z + uds$(light flavor jets), where the Z boson decays via $Z \to e^+e^-$. The signal sample $Zb\bar{b}$ is enriched in true electrons with a filter at the generator level. Both b-quarks at the generator level are required to have an electron within a cone of ΔR <0.4

The electron candidates from the $Z + uds$ and multijet Monte Carlo samples are used as background. Samples were generated using the Alpgen [48] and Pythia [49] Monte Carlo generators for the hard process and parton showering respectively. The generated objects are passed through a full ATLAS detector simulation based on GEANT4 [50]. The Monte Carlo samples used are listed in Table 8.1

Since the standard cut based menu is optimized for identifying isolated, high-pt electrons, it cannot be used for soft electron identification. The information from the TRT is extremely useful and important for identifying electrons. Therefore only electron candidates which fall within the acceptance of the TRT $|\eta| < 2$ are considered. In addition cuts are applied to the shower shape variables as well as the inner detector variables to suppress the huge hadronic background.

To reduce the number of fake electron candidates, only tracks with p_T above 5 GeV are considered. In addition the electrons lying in the "crack" region of the electromagnetic calorimeter is also removed. The number of TRT low threshold hits are required to be above 10 and with at least one high threshold hit. The tracks are required to have at least 3 pixel hits and 7 hits combined in the pixel and the SCT

Category	Samples	Generator
Signal	$pp \to Zb\bar{b}$ + Np0	Alpgen + Pythia
Background	$pp \to Zu\bar{u}$ + Np0	Alpgen + Pythia
	$pp \to Zu\bar{u}$ + Np1	Alpgen + Pythia
	$pp \to Zu\bar{u}$ + Np2	Alpgen + Pythia
	$pp \to Zu\bar{u}$ + Np3	Alpgen + Pythia
	$pp \to Zu\bar{u}$ + Np4	Alpgen + Pythia
	$pp \to Zu\bar{u}$ + Np5	Alpgen + Pythia
	$pp \to$ multijets	Alpgen + Pythia

Table 7.1: Signal and Background MonteCarlo samples. The number Np<n> indicates the number of additional partons in the event that comes from the underlying event. The hard scattering process generated by Alpgen is showered using Pythia

Type	Description
Baseline cuts	$\lvert\eta_{\mathrm{trk}}\rvert < 2.0$, $1.37 < \lvert\eta_{\mathrm{cl}}\rvert < 1.52$, $\mathrm{E}_T > 5\,\mathrm{GeV}$
Tracking cuts	At least 10 TRT Hits, 7 Silicon layer hits and 3 Pixel layer hits.

Table 7.2: Preselection cuts applied for electron candidates

layer. In order to suppress electrons from photon conversion candidates are required to have a b-layer (innermost pixel layer) hit.

B-hadrons have a significant life time of approximately 1 ps. Hence a displaced secondary vertex is a signature of the decay of the heavy B-hadron. On average, this displaced vertex is $\approx 3\,\mathrm{mm}$ from the primary vertex, still within the radius of the b-layer. Thus a b-layer hit requirement can significantly reduce photon conversion background, while keeping electrons from heavy flavor decays. A veto is applied to those tracks passing through dead b-layer modules. Details of the electron candidate preselection are given in Table 7.2

As shown in Figure 7.2 these preselection cuts only reduce the signal events by 20% within the kinematic region of our interest.

The software tool *McTruthClassifier* [51] is used to classify the candidate electrons into signal and different types of backgrounds.

The Signal electrons come from direct ($b \to e$) and cascaded ($b \to c \to e$) semileptonic decays of B-hadrons. The Background electrons arise from photon conversions occuring in the inner detector material, in flight decays of light hadrons, and hadrons wrongly reconstructed as electrons. The signal and background electron distributions for $\mathrm{p_T}$ TRT high threshold hit ratio, f_1(core) and impact parameter d_0

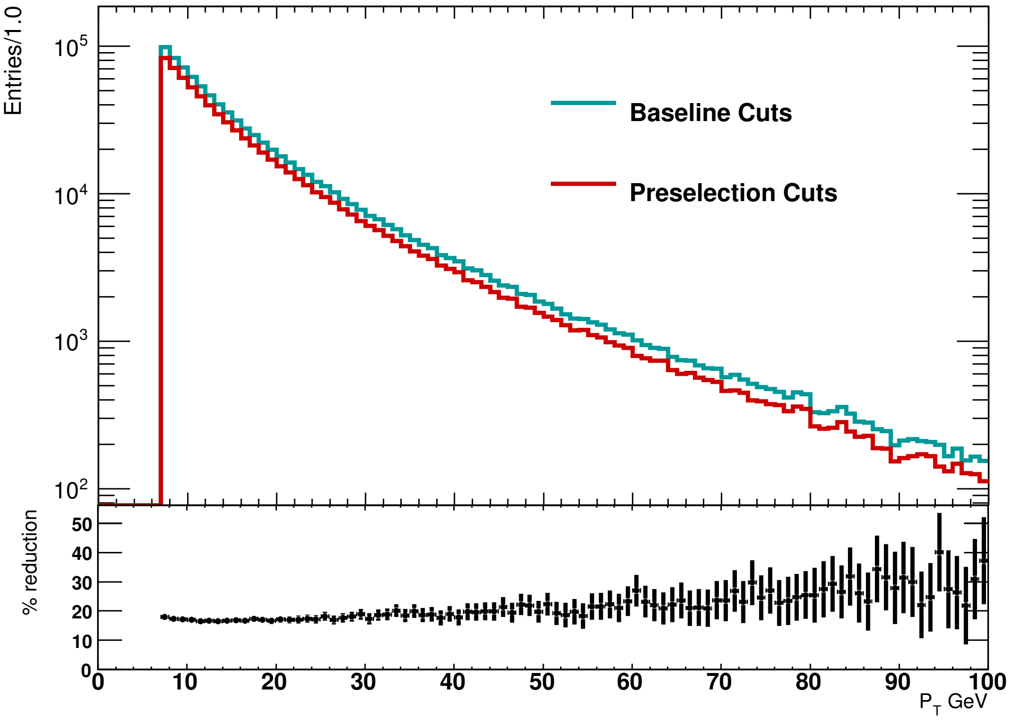

Figure 7.2: p_T distribution of electron candidates from $b \rightarrow e$ signal events sample after baseline kinematic selection and preselection. The preselection cuts reduce on an average 20% of the signal electrons with respect to the baseline selection.

are shown in Figure 7.3a. The conversion background is softer than the signal electrons whereas the hadron contamination is harder compared to the signal.

Figure 7.3b shows the TRT high threshold hit ratio for the signal and background distributions. Since the conversion electrons are true electrons, no separation is possible between signal electrons and conversion electrons.

Figure 7.3c shows the f_1(core) distribution shows a marginal discrimination between signal and background. The hadrons deposit less energy in the first layer of the electromagnetic calorimeter. Since the p_T spectrum of the conversion electrons is harder at intermediate energies, the ratio f_1(core) is peaked towards the lower values. A host of other electron distributions are shown in Appendix 8.6. Some of these variables show a very good signal and background separation, others show only a marginal separation, while certain others do not show any discrimination power against signal and background. This motivates the possibility of using a multivariate classifier which optimizes the identification of signal electrons in a multi dimensional space of these variables.

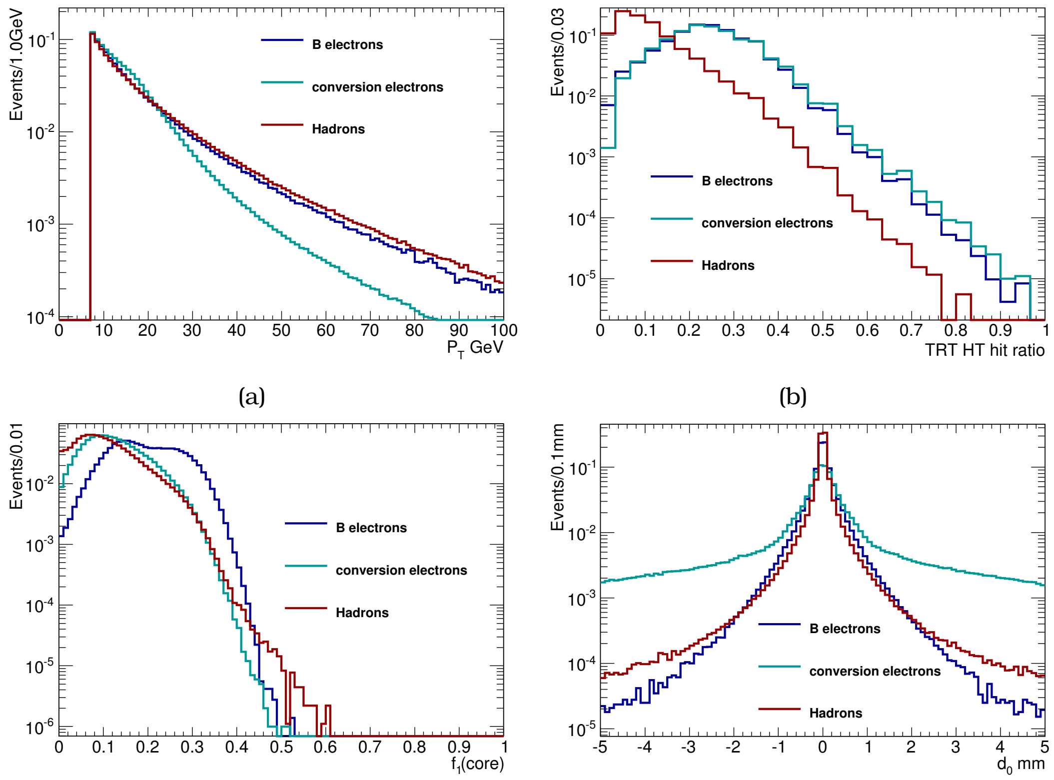

(a) (b)

(c) (d)

Figure 7.3: Normalized distributions of signal electrons (B electrons) and electrons from photon conversions and hadrons in (a) p_T, (b) in TRT high threshold hit ratio, (c) f_1(core) and (d) d_0, the transvrse impact parameter.

7.3 Multivariate Techniques

Classification of events or objects into categories of signal or background is important in high energy physics data analysis. The sequential application of cuts on multiple variables associated with an event or object is one method of signal-background separation. A group of algorithms collectively called Multivariate Algorithms (MVA) are far superior in classification compared to cut methods. They take a vector of variables from the dataset and then map them to one or more discriminating values. Based on the requirement of purity and efficiency, an operating point on this discriminating value can be fixed. These algorithms use multidimensional parameter space instead of one parameter at a time. Rather than classifying an object as signal or background, the algorithms apply a probability to be signal or background to the object.

The algorithm used in this analysis is based on Boosted Decision Trees (BDT) implemented in the TMVA framework [52]. Monte Carlo truth matching is done

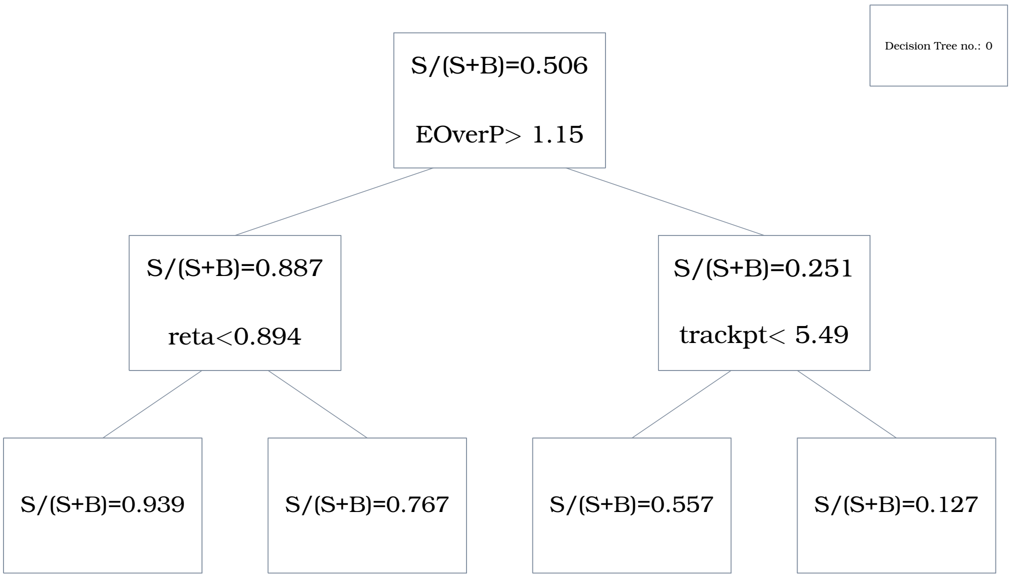

Figure 7.4: Schematic of a decision tree. S is signal and B is background. If S/(S+B) exceed a certain value then the electron is a signal electron, otherwise a background electron.

to obtain signal and background samples. These samples are divided into twoP: training and test sample. The training sample is used to train the boosted decision tree classifier and the test sample is used to benchmark the final classifier after the training.

7.3.1 Boosted Decision Tree Algorithm

A decision tree is a machine-learning technique that is used to predict a target variable based on several input variables. Sequential cuts are applied to the candidate depending on whether it passed or failed a previous cut. These cuts are organised as nodes like in a tree like structure. At a node a variable and cut value are evaluated and the candidate either pass or fail the cut. However, candidates which fail the cut are not discarded. The cut evaluation only determines the fate of the candidate, as to which node the candidate will encounter next.

As seen in Figure 7.4, a tree begins at a primary (root) node and branches off to two secondary nodes corresponding to the pass or fail of the root node cut. Each of these nodes carries a cut value. A candidate evaluated at this node would advance to other nodes down the tree, either to the left or right child node. This propagation of candidates finally ends at a terminal node or “leaf” which posses a classifier value. This value will be assigned to the candidate. All events are given a decision tree score between -1 and 1 which can of course be normalized to some other desired range.

Decision tree training is a supervised learning procedure which uses a set of known signal and background training samples. Each candidate is assigned a weight to build a tree structure of cut nodes. The function used in this method to quantify the separation between signal and background at any given node is the *Gini index* [53] $p(1-p)$, where p is the purity. Purity is defined as

$$p = \frac{\sum_s W_s}{\sum_s W_s + \sum_b W_b}, \tag{7.1}$$

where $\sum_s$ is the sum over signal and $\sum_b$ is the sum over background. W_s and W_b are the weights given to the signal and background samples.

For a given branch

$$\text{Gini} = \left(\sum_{i=1}^{n} W_i\right) p(1-p), \tag{7.2}$$

The *Gini index* is 0 when the purity is either maximal or minimal (p=0 or p =1).

At the root node the cut values that corresponds to maximum separation is executed on the input variables. The maximum separation is defined as the maximum change in the Gini index between the parent node and the two child nodes

$$C \equiv \text{Gini}_{\text{parent}} - \text{Gini}_{\text{left,child}} - \text{Gini}_{\text{right,child}} \tag{7.3}$$

The cut corresponding to the highest C value is chosen for the initial branching. After the initial branching, the best cuts according to the *Gini* separation are calculated and executed for both the left and right child nodes. The tree then grows as the cut selection process continues at each node. A node is no longer split at the "leaf" node where a split would result in less than a minimum number of events landing in the node. Each leaf node is subsequently assigned a purity value according to Eq: 7.1

Decision trees were hardly used in high energy physics due to their sensitivity to statistical fluctuations in the training sample. However with the advent of a general class of technique called *boosting* this has changed [53]. Boosted decision trees combine many different weak decision trees in order to suppress their sensitivity to statistical fluctuations.

Boosting is a way of enhancing the performance of a weak multivariate classifier. After the initial classifier training, the training sample is modified such that previously misclassified candidates are given a larger weight. The procedure is done iteratively and finally the results of all the different classifiers are averaged. The final classifier is then a linear combination of the so called base classifiers.

$$y_{\text{Boost}}(\mathbf{x}; \alpha_0, \ldots, \alpha_M, \mathbf{a_0}, \ldots, \mathbf{a_M}) = \sum_{i}^{M} \alpha_M b(\mathbf{x}; \mathbf{a_m}), \tag{7.4}$$

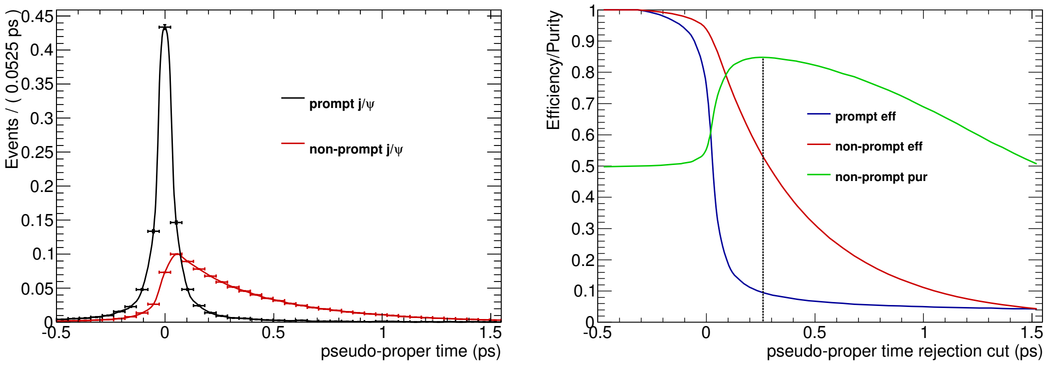

(a)

(b)

Figure 7.5: (a) Pseudo-proper time distributions for prompt J/ψ's directly produced in proton-proton collisions and non-prompt J/ψ's produced in B-hadron decays (b) Efficiency for finding both components as well as the purity for finding non-prompt J/ψ's are plotted as a function of rejection cut on pseduo-proper time. The Maximum purity corresponds to a rejection cut value of 0.261.

where $b(\mathbf{x}; \mathbf{a_m})$ are the M trained based classifiers. $\mathbf{a_m}$ denote the parameters of the classifier m obtained in the training. The weight of the classifier in the boost procedure is denoted by α_M. The final result of boost procedure is typically better than the individual classifiers, especially when they are weak classifiers. For a detailed description refer [54].

There exist different classes of boosting algorithms, however here, a particular algorithm called *gradient boosting* algorithm is used.

7.4 Variable Validation using Data

The Monte Carlo description of the electron identification variables may not be the same as that in real data. There are known Monte Carlo mis-modellings, for instance in the TRT responses and the shower shapes in the electromagnetic calorimeter [44]. In order to compare the electron identification variables in data and Monte Carlo a J/ψ sample is selected and the so-called "tag and probe" method is applied.

The branching fraction of J/$\psi \rightarrow e^+e^-$ is 5.94 ± 0.06% [33]. The other known decays of J/ψ are into muons and hadrons. Therefore the detection of one decay electron implies the existence of the other with a combined invariant mass close to that of J/ψ. One well reconstructed electron is selected applying the *tight*++ identification cut. This is labelled as the tag electron. Since the existence of the other electron pair is guaranteed, a loose selection or selection schemes required by the study can be applied on the other electron.

J/ψ final states are composed of two contributions. One is called a *prompt* component which comes from J/ψ directly produced in the proton-proton hard scattering. The other one is called a *non prompt* component as they come from B-hadron decays. The non-prompt J/ψ's are produced in a busy environment of jets and therefore the electron-positron pairs coming from their decay are not well isolated.

Experimentally it is possible to separate these two components. The *prompt* decays occur close to the primary vertex while the decay of *non prompt* component will have a measurably displaced vertex due to their long lived B-hadron parent. This displaced vertex can be parameterised through pseudo-propertime [55] defined as

$$t_0 = \frac{L_{xy}.m_{J/\psi}}{p_T(J/\psi)}, \tag{7.5}$$

where $m_{J/\psi}$ and $p_T(J/\psi)$ are the mass and transverse momentum of the J/ψ. The transverse decay length L_{xy} is the projected decay length of the J/ψ candidate on to the $x-y$ plane. Pseudo-propertime values of prompt J/ψs are lesser compared to non prompt J/ψs which are produced through the decay of long lived B-hadrons.

The tag electron is required to pass the standard *tight*++ cut. The probe electron is required to fulfill the preselection cut. The difference between the z-components of tag and probe electron pair at the vertex must be less than 0.2 mm. The p_T of the tag and probe pair should be more than 500 MeV. These pairs should also be well separated in the calorimeter. $\Delta R^{\text{calo}}_{\text{tag-probe}} > 0.1$ to make sure that the probe is not effected by a close by tag electron. The invariant mass of such opposite sign tag and probe pairs in three E_T bins are shown in Figure 7.6. The signal is modelled using a *CrystalBall* function. A convolution of *lognormal* distribution and a first order polynomial to describe the background in the sidebands. The ψ_{2s} peak also becomes visible in higher E_T bins.

7.4.1 Sideband Subtraction Method

Sideband subtraction is a statistical method used to obtain signal distributions from a combined signal and background sample. The sideband subtraction involves at least two variables. A "separation variable" such as the mass, and an associated variable distribution, for instance p_T. The goal is to statistically subtract the background contamination in the associated variable using the separation variable.

In our case the J/ψ invariant mass distribution is the separation variable and the goal is to obtain pure signal distributions from the data for all the electron variables associated to the probe leg of the tag-probe pair.

Even though the signal region is predominantly consists of signal events, it is not free of background. The invariant mass distribution is divided into three regions, one signal region and two sideband regions. The signal region is selected such that it covers roughly 1.5 σ around the mass peak. The sidebands constitute the low

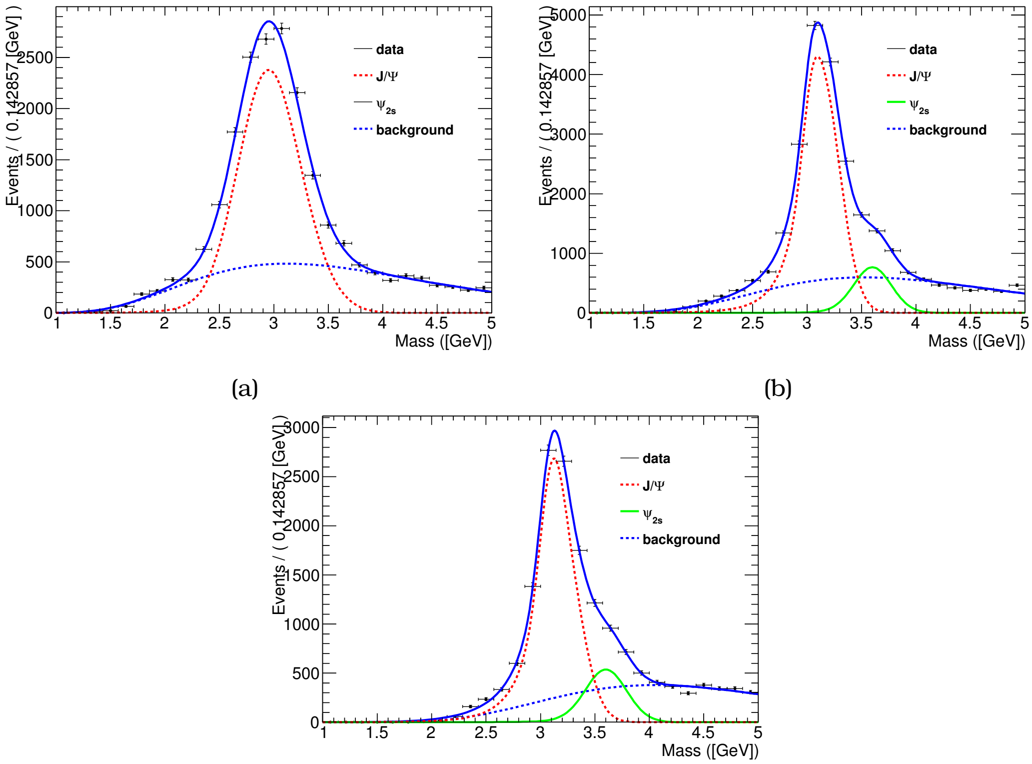

(a)

(b)

(c)

Figure 7.6: J/Ψ invariant mass distributions in bins of (a) 5 GeV to 10 GeV (b) 10 GeV to 15 GeV (c) 15 GeV to 20 GeV probe transverse momentum. The black dots represent data while the continuous lines are signal and background models fit to the data. ψ_{2s} contribution is shown in green. The J/ψ peak as well as the ψ_{2s} is modelled using Crystal ball function. The background is modelled by a combined *logNormal* and first order polynomial.

and high mass region where the signal contribution is small or negligible. With a model which describes signal and background, a fit is made to the invariant mass distribution. The background events in the signal region are estimated from the side-band regions. Then electron variable distributions are constructed for these regions. The goal is to estimate the number of background events in each bin of the signal region and to subtract it in order to obtain a pure signal distribution for every variable.

Number of background events in the signal region and sideband region can be obtained from the background fit. The ratio of number of background events in the signal band to the number of background events in the sidebands gives the *signal-to-sideband background* ratio.

For a given variable α, the true distribution α_{pure} can be obtained by the following

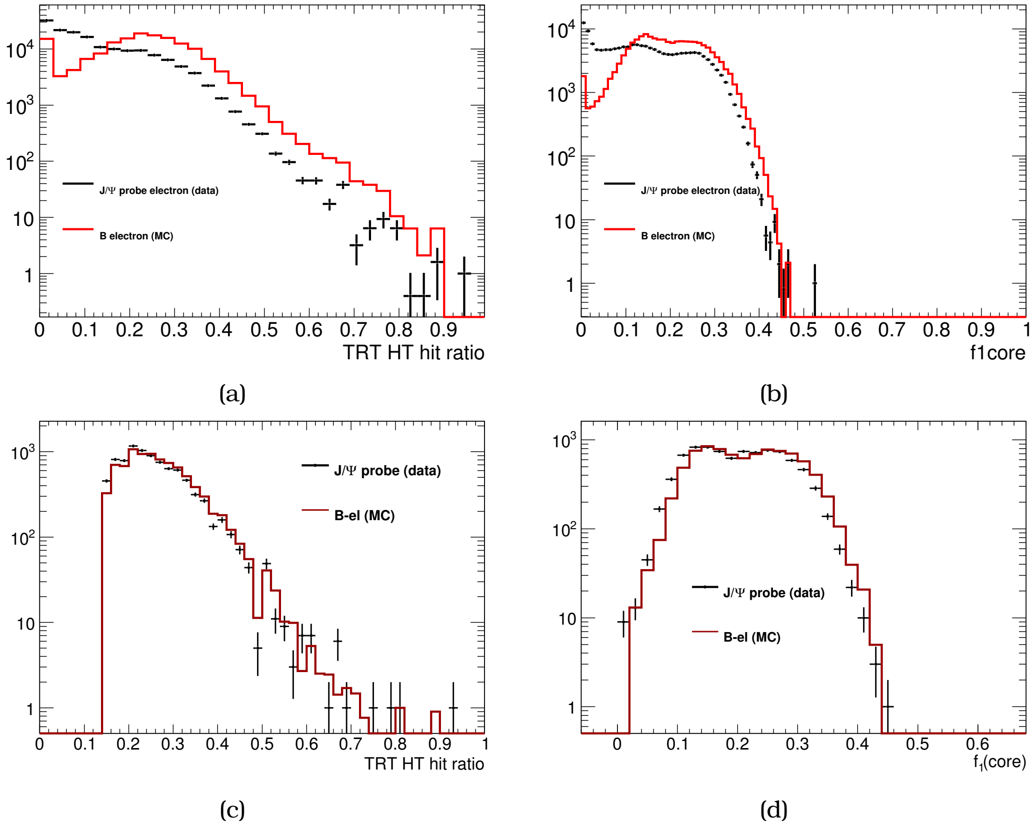

(a) (b)

(c) (d)

Figure 7.7: Electron distributions: (a) TRT high threshold hit ratio distribution and (b) f_1(core) distribution showing the hadronic contamination at low values. The Monte Carlo is normalized to the entries in the data. The distributions (c) and (d) shows the TRT high threshold hit ratio and f_1(core) after removing the hadronic contamination.

formula

$$\alpha_{\text{pure}} = \alpha_{\text{Signal band}} - \text{MF} \times \alpha_{\text{Sideband}}, \tag{7.6}$$

where α_{pure} is the true signal distribution, α_{Sideband} is the α distribution in the sidebands, $\alpha_{\text{Signal band}}$ is the α distribution in the signal region and MF is the *signal-to-sideband background* ratio. A closure test has been performed to verify this method. See Appendix 3.

We used non-prompt J/ψ sample to extract pure electron distributions. Since these electrons are in a dense environment, their characteristic electron distributions should match to those coming from B-hadron decays. However, not all electron variable distributions extracted from data using sideband subtraction method is well described by the Monte Carlo. This is expected as the shower parameterization in Monte Carlo are not expected to describe the data quite well [44]. This can be clearly seen from the TRT hit ratio distributions and the f_1(core) distributions shown in Figure 7.7. A cut value of 0.15 is applied on f_1 and a cut on TRT high threshold hit ratio at 0.1 is applied to discard the hadronic component that is not described by the Monte Carlo. After applying this cut significant improvement in data and Monte Carlo agreement is observed.

Some of the distributions after applying the cut values are shown in the Figure 7.8

7.5 Variables for MVA input

Validated variables based on calorimeter, ID or either combinations of both are used in the soft electron identification. A list of variables used to train BDTG classifier is given in Table 7.3.

Classifiers with a small number of degrees of freedom are less prone to statistical fluctuation in the training sample. However if the underlying probability density function(PDF) has a rich feature, it cannot be described by the limited number of degrees of freedom. Moreover if more degrees of freedom are introduced the classifier becomes more vulnerable to statistical fluctuations in the training sample. Hence an optimum number of trees has to be chosen which describes the features of the underlying PDF and also making the classifier less susceptible to statistical fluctuations (also known as overtraining). Overtrain checks has been done using a statistically independent test sample. Figure 7.9 shows BDTG response curves for training sample and a statistically independent test sample. The response curves do not show any overtraining features.

7.5.1 BDTG optimization

The BDTG performs better when the input variables are largely uncorrelated. Therefore variable sets which are uncorrelated are used in the identification tool.

The variable set is also optimized using a so called "n-1" technique. The BDTG classifier with n (all) variables is evaluated using a sample of signal and background electrons and the signal efficiency is plotted against the background rejection.

In a subsequent step the process is repeated on n BDTG classifiers, each trained with the original set of variables minus one variable at a time. If a particular classifier performs worse than the original, the removed variable has a good discrimination power and it should be considered to be retained in the final optimized set of variables. On the other hand if an *(n-1)* th BDTG classifier is performing better than the original then the removed variable is not contributing effectively to an optimal classifier. Repeating this process until all the variables are tested, a set of optimal variables is finally arrived. The BDTG classifier is trained with the set of variables which optimize the performance.

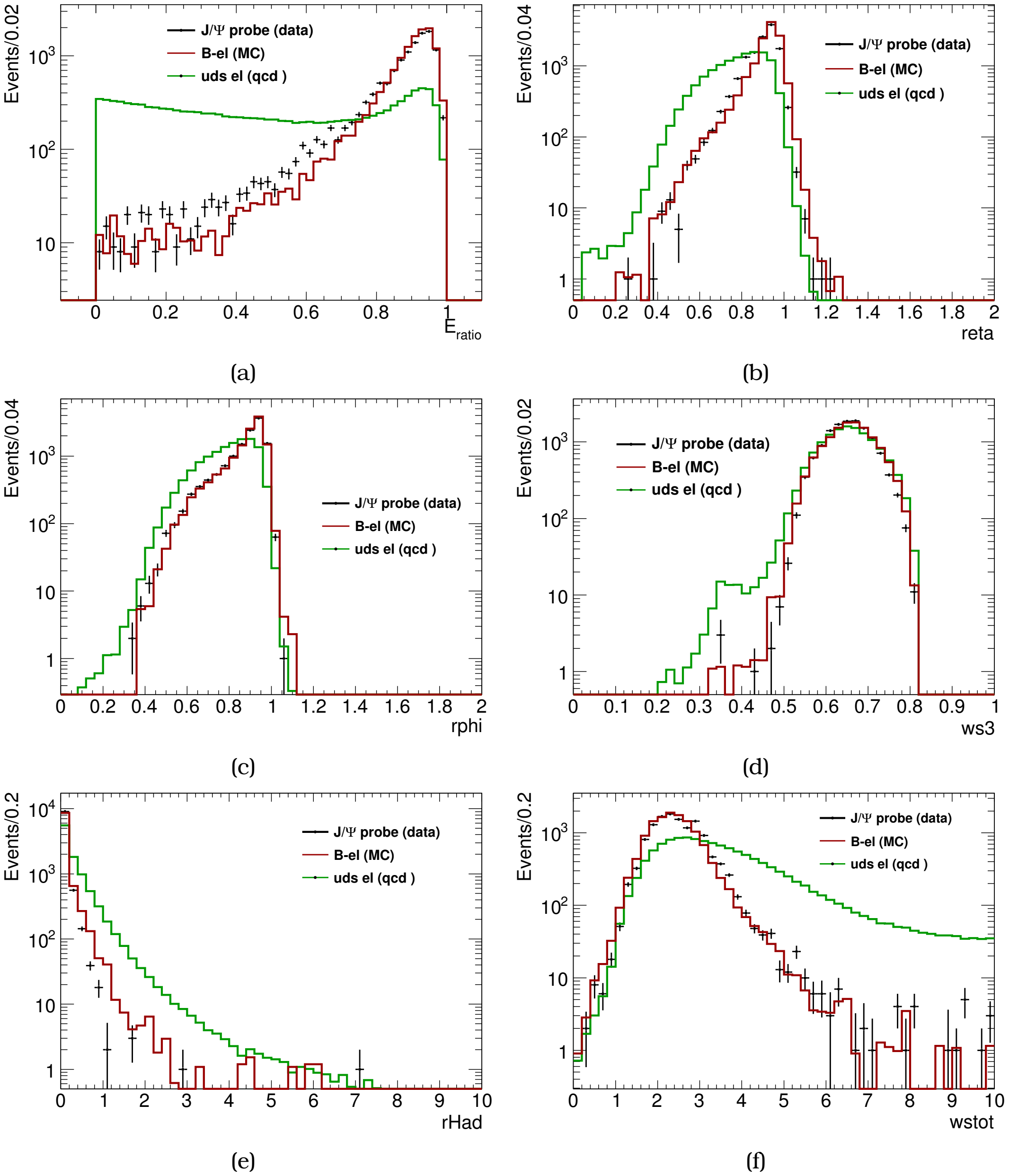

(a) (b) (c) (d) (e) (f)

Figure 7.8: Electron identification variables obtained from J/ψ enriched sample using sideband subtraction method. The B-electron variables shows remarkable agreement with the variables obtained from data. Background electron distributions obtained from a QCD multijet sample is also plotted for comparison.

Decision trees work by optimizing the signal and background at every node. It is impossible to predict how a cut at a particular node will effect the possible separation

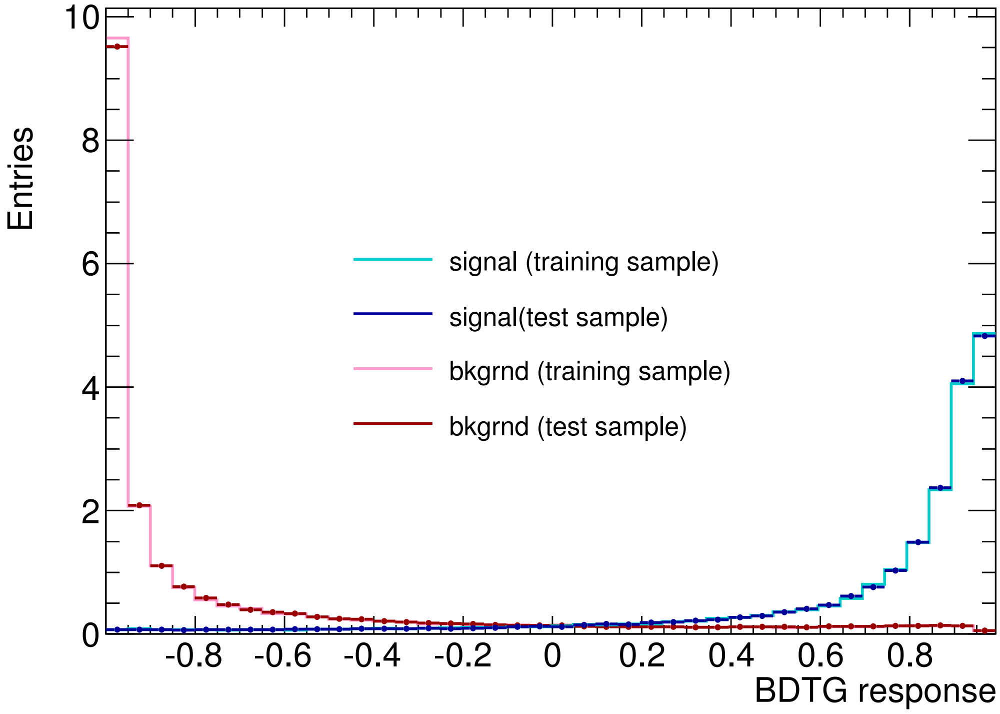

Figure 7.9: Overtraining check for BDTG classifier. Statistically independent background and signal samples are used to check if the classifier is overtrained. The signal sample consists of electrons truth matched to a B-hadron, obtained from $Z + b\bar{b}$ Monte Carlo sample. The background is an electron sample obtained from QCD multijet sample which consists of electron fakes, hadrons and electrons from light flavor decay. The remarkable agreement between the test and training sample shows that there is no significant overtraining.

of signal and background further down the tree. If any cut naturally separates candidates into signal and background such cuts should be implemented before training. Therefore we bin the signal and background electron candidates in E_T and train them separately.

Figure 7.11 shows the signal efficiency versus background rejection curve for electrons from B-hadron decay for both the BDTG classifier and standard cut menu. The BDTG shows up to 50% less background at the same efficiency.

7.6 Efficiency and Systematics

The tag and probe method is used to measure the efficiency of soft electron identification. The tag electron is required to pass the standard *tight*++ cut with a p_T above

Variable	Description
$\mathrm{p_T}$	Transverse momentum measured in the track or calorimeter (depending on certain track quality cuts)
cl_E	Energy measured in the cluster after applying corrections and scale factors
f_1(core)	Ratio of energy deposition in the core region of the calorimeter cluster
f_3(core)	Ratio of energy deposition in the core region of the calorimeter cluster
w_η^2	Energy weighted RMS of η co-ordinates of the cells in the calorimeter cluster
w_{s3}	Shower width over three strips around the maximum energy deposited strip
$w_\mathrm{s,tot}$	The shower width in the first sampling layer (over 20 strips)
depth	The longitudinal shower depth in the second sampling layer
$\mathrm{f_{HT}}$	Fraction of high-threshold hits in the TRT
E/P	The ratio of energy reconstructed in calorimeter to the momentum reconstructed in the ID
$\Delta\eta_2$	The difference between extrapolated track η and the η measured in the calorimeter
$\Delta\phi_\mathrm{rescaled}$	rescaled $\Delta\phi$ after accounting for bremstrahlung losses (GSF output)
$\Delta P/P$	Normalized momentum correction after accounting for bremstrahlung losses (GSF output)
E_ratio	Ratio of the energy differences between the first and second maximum energy depositions in the strip layer to the sum of these energy maximums
R_η	Ratio of energy deposited in 3×7 cells to the energy deposited in 7×7 cells in $\eta\times\phi$ in the second sampling layer
R_ϕ	Ratio of energy deposited in 3×3 cells to the energy deposited in 7×7 cells in $\eta\times\phi$ in the second sampling layer
d_0	Distance of closest approach of the track to the primary vertex in the transverse plane

Table 7.3: List of variables used in training BDTG multivariate classifier.

5 GeV. The probe electron is only required to pass the baseline kinematic selection cuts. The tag and probe pairs are fitted to a common vertex in order to reduce the combinatorics. Since J/Ψ's decay in flight, the electron positron pair is expected to be in the same hemisphere. A cut $\Delta R < 3.5$ is applied to ensure this. The invariant

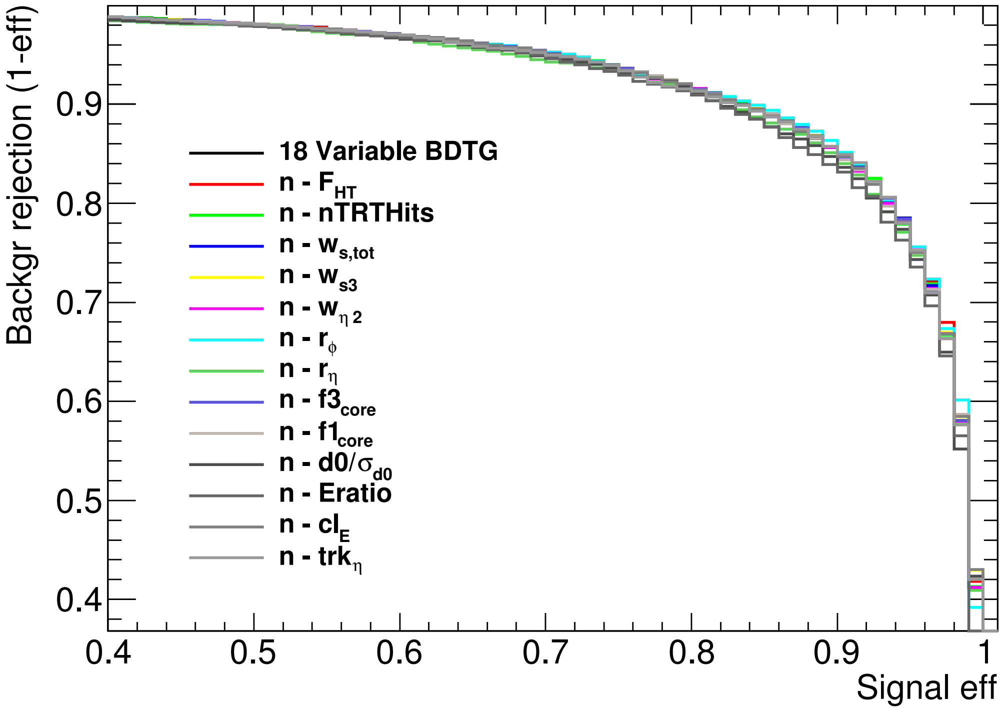

Figure 7.10: Variable set optimization using *n minus one* technique. Individual variables are sequentially removed, one at a time for different classifiers and their performance is compared.

mass distribution for the resulting tag & probe pair is shown in Figure 7.12

The ratio of tag and probe pairs after background subtraction to these tag and probe pairs that pass the soft electron identification criteria, gives the electron identification efficiency.

$$\epsilon = \frac{N^{J/\psi}_{\textit{soft electron probes}}}{N^{J/\psi}_{\text{probes}}} \tag{7.7}$$

The systematic uncertainty is taken as the statistical uncertainty on the efficiency, the uncertainty on the fit used to estimate the background added in quadrature.

The background is estimated using a polynomial function $y = ax^2 + bx + c$. The background estimate is varied between its maximum and minimum values obtained from the fits. The difference in the efficiencies calculated using the signal value from these different backgrounds is taken as the systematic uncertainty on the background fit. These uncertainties are added in quadrature as following.

$$\Delta\epsilon = \sqrt{(\Delta\epsilon_{\text{stat}})^2 + (\epsilon_{\text{bkg, max}} - \epsilon_{\text{bkg, min}})^2} \tag{7.8}$$

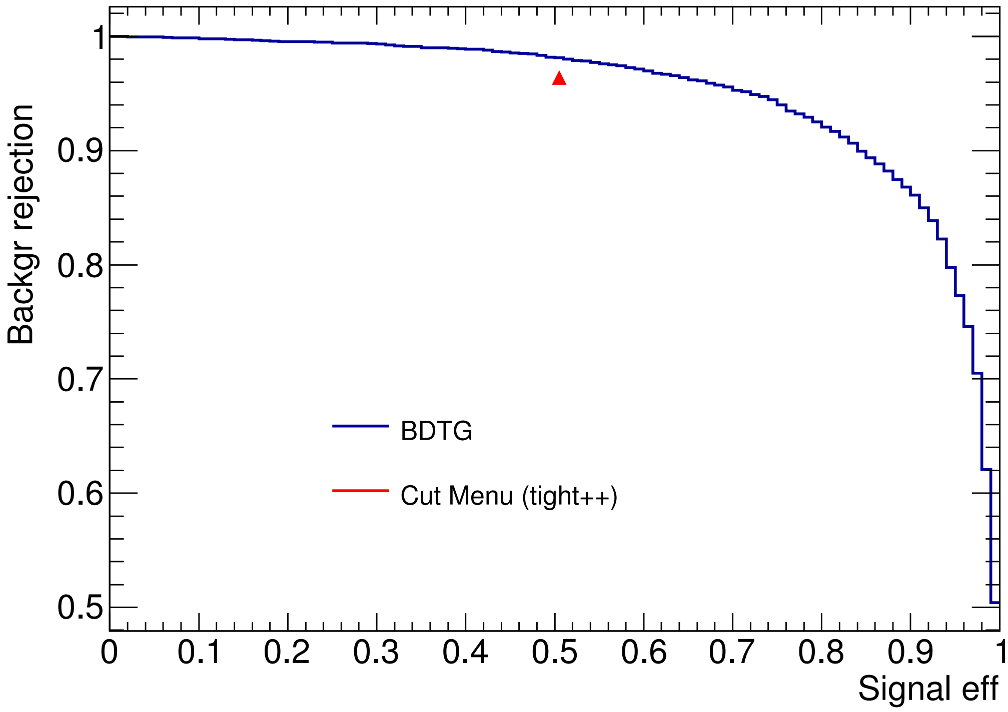

Figure 7.11: Background rejection as a function of signal efficiency, plotted for both the BDTG classifier and the standard tight++ cut menu. The BDTG classifier offers significantly higher performance in terms of background rejection and signal effciency for the not so well isolated B electron identification.

Probe electron p_T [GeV]	Reconstruction Efficiency (ϵ)	Uncertainty stat	$\epsilon_{bkg,max} - \epsilon_{bkg,min}$	Total
5-10	0.733	0.00312	0.01959	0.01984
11-15	0.743	0.00241	0.01473	0.01492
16-20	0.718	0.00316	0.02407	0.02428

Table 7.4: Soft electron reconstruction efficiency. Statistical and background fit uncertainties as well as the quadrature sum of these uncertainties are shown.

7.7 Conclusion

The standard cut based menu for electron identification is not optimzied for the identification of electrons that come from semileptonic decay of B-hadrons. Using a boosted decision tree, the electron identification capability of the ATLAS inner detector and calorimeter is exploited. The boosted decision tree based soft electron

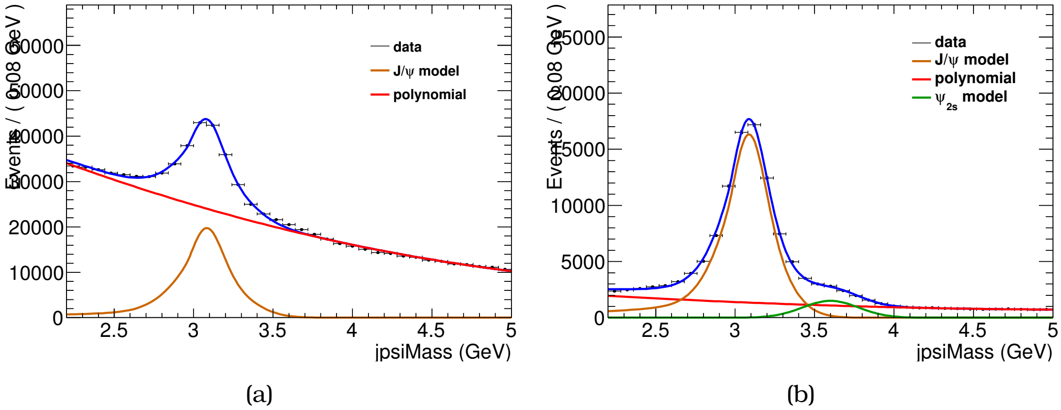

Figure 7.12: Invariant mass distribution for (a) all tag & probe pair and for (b) probes that pass BDTG operating point 0.5. The signal is modelled by a convolution of CrystalBall function and gaussian. The background is estimated using a second order polynomial.

identifier is found to have a better signal efficiency and background rejection compared to the standard cut menu. The average efficiency of the tagger has been found to be around 74% which is comparable to the efficiency of the standard *tight*++ operating point. The uncertainty has been found to be less than 2.5%

Chapter 8

$pp \rightarrow Z(e^+e^-) + b\bar{b}$ Feasibility with Soft Electron Tagger

In this chapter, use of the soft electron tagger for the measurement of the associated production of two b-quarks with a Z-boson is explored. The decay of the Z-boson into two opposite sign electrons and the semileptonic decay of both b-quarks leads to a four electron final state. The kinematics of electrons coming from the decay of Z-bosons is different from the kinematics of electrons coming from the semileptonic decay of b-quarks. Appropriate electron identification schemes are used for identifying these two electron categories.

8.1 Decay Kinematics

Z-bosons undergo prompt decays into electron positron pairs. These electrons are relatively isolated with distinct shower shape patterns in the calorimeter. The b-quarks which are produced in the primary hard interaction undergo parton shower and hadronization which is manifested as a stream of particles in the detector, called jets. The fragmentation of b-quarks is "hard" compared to other light flavors. Therefore the B-hadrons have relatively high p_T compared to other light hadrons. When B-hadrons undergo semileptonic decay into electrons, they tend to have a larger p_T with respect to the jet axis, since the parent B-hadron is massive. These electrons are more energetic than those electrons coming from light hadrons. However, they are still much less energetic and less isolated compared to electrons coming from Z-boson decays.

The measurement of $b\bar{b}$ production is based on the identification and selection of two electrons at low momentum ($p_T > 7\,\mathrm{GeV}$). About 2% of the $b\bar{b}$ final states, are constituted by two electrons originating from the same b-quark, through the cascaded decay ($b \rightarrow ce^-\bar{\nu}_e \rightarrow se^+e^-\bar{\nu}_e\nu_e$). And about 4% of $b\bar{b}$ final states are constituted by two electrons originating from different b-quarks. These electrons are either the direct product of the semileptonic decay of both b-quarks or from subsequent semileptonic decay of a c-quark in one of the b-quark legs. The charge of these electrons can either be opposite ($b\bar{b} \rightarrow e^+e^-X$ and $c\bar{c} \rightarrow e^+e^-X$) or same

($b\bar{c} \rightarrow e^-e^-X$ and $\bar{b}c \rightarrow e^+e^+X$) [56].

A series of cuts at the event level as well as on electron candidates are applied to identify the signal with two opposite charge high p_T electrons which are the decay products of the Z-boson. The two electrons that come from semileptonic decay of B-hadrons are identified using the soft-electron tagger.

8.2 Data and Monte Carlo Samples

The data used in this analysis is from the 2012 proton-proton collision run take by the ATLAS experiment when the LHC was operated at a center of mass energy of $\sqrt{s}$=8 TeV. Only data which were recorded during good operation conditions of the calorimeter and inner detector systems are considered. It corresponds to 20.3 fb^{-1} of total integrated luminosity of data. However, only 16.2 fb^{-1} of data is used for this analysis.

The Monte Carlo samples used for this analysis were generated using the matrix element event generators Alpgen [48] and Pythia [49] for parton shower calculations. The generated events are passed through the full simulation [57] of the ATLAS detector. A list of all datasets used is shown in Table 8.1

8.2.1 Heavy Flavor Overlap Removal

In all the Monte Carlo samples used in this analysis, proton-proton collisions are simulated by interfacing a matrix element generator with a parton shower generator. Potential overlaps between the phase space covered by the matrix element generator and parton shower Monte Carlo have to be removed in order to avoid double counting. For soft collinear emissions, the parton shower description has been found to agree quite well with data. Complimentary to this the matrix element description matches with data in case of widely separated hard emissions. Parton shower-matrix element matching schemes remove phase space overlaps, However in the Alpgen samples that are used, there do exist such overlaps. Therefore it is necessary to discard these duplicated events.

If two events with same configuration are encountered, the following scheme is adopted to remove the overlap. If the heavy quarks have a large opening angle, then the event is taken from ME calculation. If the event contains two collinear quarks then the parton shower calculation is used. These operations are performed by the official tool *Heavy Flavor Overlap Removal* (HFOR) [58].

8.3 Event Selection

In order to reduce scattering with residual gas, accelerators propagate beams at high vacuum. Even though the proton beams circulate in the LHC at ultra high vacuum,

Category	Samples	Generator
Signal	$pp \rightarrow Z \rightarrow e^+e^-b\bar{b}$ + Np0	Alpgen + Pythia
	$pp \rightarrow Z \rightarrow e^+e^-b\bar{b}$ + Np1	Alpgen + Pythia
	$pp \rightarrow Z \rightarrow e^+e^-b\bar{b}$ + Np2	Alpgen + Pythia
	$pp \rightarrow Z \rightarrow e^+e^-b\bar{b}$ + Np3	Alpgen + Pythia
Background	$pp \rightarrow Z \rightarrow e^+e^-c\bar{c}$ + Np0	Alpgen + Pythia
	$pp \rightarrow Z \rightarrow e^+e^-c\bar{c}$ + Np1	Alpgen + Pythia
	$pp \rightarrow Z \rightarrow e^+e^-c\bar{c}$ + Np2	Alpgen + Pythia
	$pp \rightarrow Z \rightarrow e^+e^-c\bar{c}$ + Np3	Alpgen + Pythia
Background	$pp \rightarrow Z \rightarrow e^+e^-$+ Np0	Alpgen + Pythia
	$pp \rightarrow Z \rightarrow e^+e^-$+ Np1	Alpgen + Pythia
	$pp \rightarrow Z \rightarrow e^+e^-$+ Np2	Alpgen + Pythia
	$pp \rightarrow Z \rightarrow e^+e^-$+ Np3	Alpgen + Pythia
	$pp \rightarrow Z \rightarrow e^+e^-$+ Np4	Alpgen + Pythia
	$pp \rightarrow Z \rightarrow e^+e^-$+ Np5	Alpgen + Pythia
Background	$pp \rightarrow W \rightarrow e\nu$+ Np0	Alpgen + Pythia
	$pp \rightarrow W \rightarrow e\nu$+ Np1	Alpgen + Pythia
	$pp \rightarrow W \rightarrow e\nu$+ Np2	Alpgen + Pythia
	$pp \rightarrow W \rightarrow e\nu$+ Np3	Alpgen + Pythia
	$pp \rightarrow W \rightarrow e\nu$+ Np4	Alpgen + Pythia
	$pp \rightarrow W \rightarrow e\nu$+ Np5	Alpgen + Pythia
Background	$pp \rightarrow ZZ$ + Np0	Alpgen + Pythia
	$pp \rightarrow ZZ$ + Np1	Alpgen + Pythia
	$pp \rightarrow ZZ$ + Np2	Alpgen + Pythia
	$pp \rightarrow ZZ$ + Np3	Alpgen + Pythia
Background	$pp \rightarrow WW \rightarrow l\nu l\nu$ + Np0	Alpgen + Pythia
	$pp \rightarrow WW \rightarrow l\nu l\nu$ + Np1	Alpgen + Pythia
	$pp \rightarrow WW \rightarrow l\nu l\nu$ + Np2	Alpgen + Pythia
	$pp \rightarrow WW \rightarrow l\nu l\nu$ + Np3	Alpgen + Pythia
Background	$pp \rightarrow WZ$ + Np0	Alpgen + Pythia
	$pp \rightarrow WZ$ + Np1	Alpgen + Pythia
	$pp \rightarrow WZ$ + Np2	Alpgen + Pythia
	$pp \rightarrow WZ$ + Np3	Alpgen + Pythia
$t\bar{t}$	$pp \rightarrow t\bar{t}$	McAtNlo + Herwig

Table 8.1: Signal and Background Monte Carlo samples. The number Np<n> indicates the number of additional partons in the event that come from underlying events.

proton interaction with residual gas in this rarefied medium is not negligible. The rate is proportional to the pressure in the beam pipe and it is assumed to be constant [59]. In order to avoid such events a track multiplicity cut is applied on the primary vertex candidate. Only events which have a primary vertex candidate with at least 3 associated tracks are considered.

Events are also required to pass a high level di-electron trigger `EF_2e12Tvh_loose1` or `EF_2e12Tvh_loose1_L2StarB`. These triggers select events for which the Event Filter has identified two electrons with p_T above the threshold of 12 GeV passing the loose identification criteria. Further up in the trigger chain at Level-1, it requires two electromagnetic signals in the calorimeter, isolation requirements in the hadronic trigger towers and corrections for dead material. The di-electron trigger becomes fully efficient at 20 GeV.

8.3.1 Event Weights

The standard pileup conditions simulated by the Monte Carlo samples are in disagreement with the data. The amount of events simulated at given pileup-condition does not match to the proportion of the events at the same pileup conditions in data. To correct for that pileup weights are calculated using an ATLAS official tool and applied to all the Monte Carlo samples. The average number of interactions per bunch crossing μ as well as the number of primary vertices reconstructed (n_{vtx}) is shown in Figure 8.1. Applying the weights improve both μ and n_{vtx} agreement with data.

The width of the z-coordinate distribution of the reconstructed primary vertex is over estimated in the Monte Carlo sample. A weighting factor is applied to correct for this as well. Figure 8.2 shows the primary vertex z-coordinate distribution after applying the weights.

8.3.2 Energy Scale and Resolution

The energy mis-calibration is a measure of the difference in response between data and simulation. It is represented by the following relation

$$E^{\mathrm{data}} = E^{\mathrm{MC}}(1 + \alpha), \tag{8.1}$$

where E^{data} and E^{MC} are the electron energy reconstructed in data and simulation respectively. The mis-calibration term α represents the departure from optimal calibration.

The energy resolution of the electromagnetic calorimeter can be parameterised

$$\frac{\sigma_{\mathrm{MC}}(E)}{E} = \frac{a}{\sqrt{E}} \oplus \frac{b}{E} \oplus c, \tag{8.2}$$

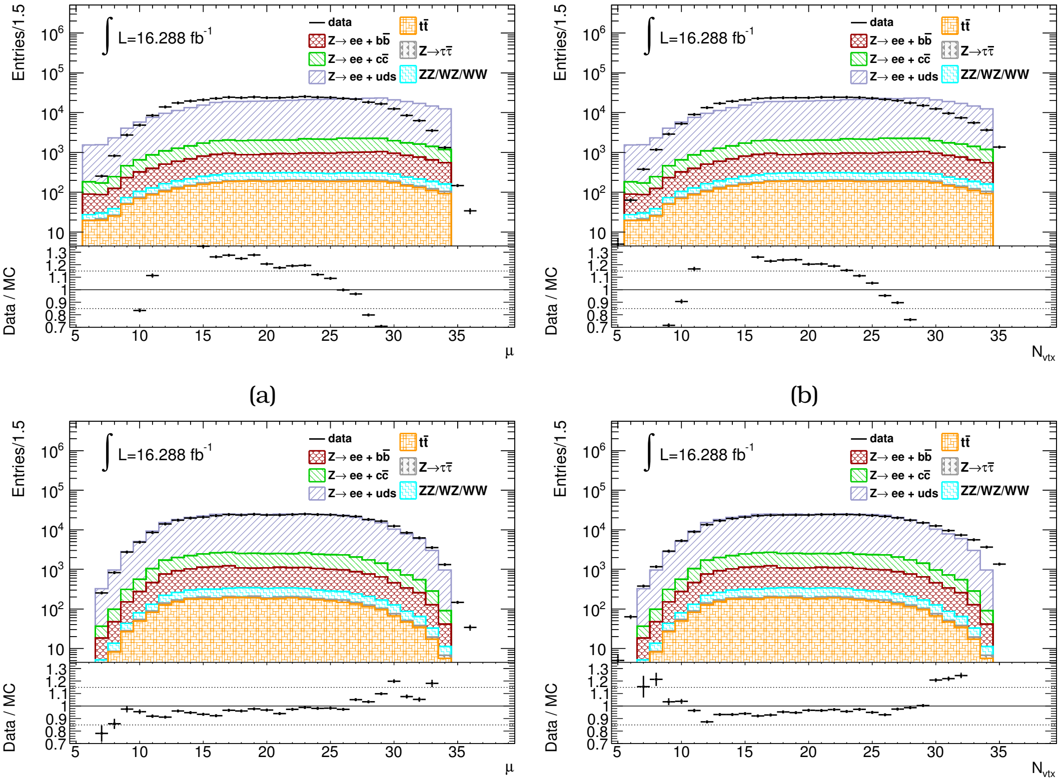

(a) (b)

(c) (d)

Figure 8.1: (a) and (b) show the average number of interactions per proton bunch crossing μ and number of primary vertices reconstructed in an event n_{vtx} respectively using default settings. Both variables are a measure of pileup. (c) and (d) show the same variables after applying weights to the various Monte Carlo samples. After re-weighting, the Monte Carlo agreement with data improves significantly.

where a is the sampling term, b is the noise term and c is the constant term. The sampling term is known up to 10% from test beam studies [60]. Resolution corrections are derived with the assumption that resolution is well modelled by the Monte Carlo up to a constant term c as the following.

$$\left(\frac{\sigma_E}{E}\right)^{\text{data}} = \left(\frac{\sigma_E}{E}\right)^{\text{MC}} \oplus c \tag{8.3}$$

The energy mis-calibration and resolution is directly linked to the reconstructed invariant mass for lepton pairs ij, by the following relations

$$m_{ij}^{\text{data}} = m_{ij}^{\text{MC}}(1 + \alpha_{ij}) \tag{8.4}$$

$$\left(\frac{\sigma_m}{m}\right)_{ij}^{\text{data}} = \left(\frac{\sigma_m}{m}\right)_{ij}^{\text{MC}} \oplus c_{ij} \tag{8.5}$$

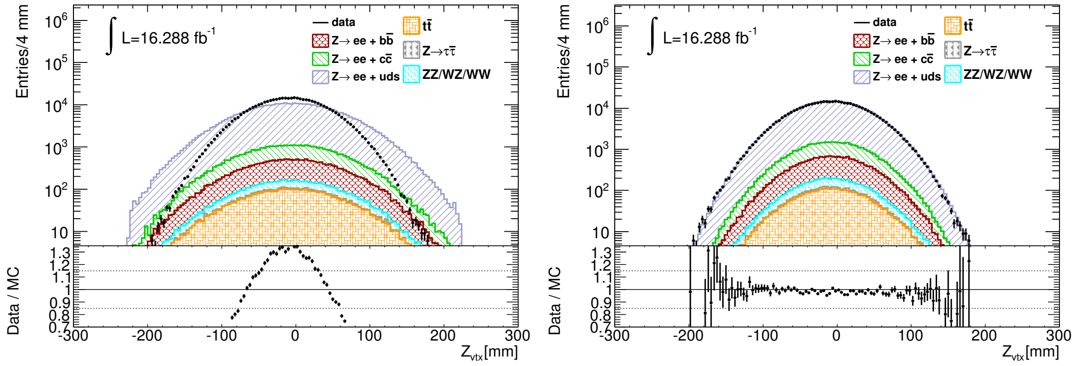

(a)

(b)

Figure 8.2: (a)The distribution of primary vertex z-coordinate in data and simulation (b) Primary vertex z-coordinate distribution after applying a weighting factor to the Monte Carlo samples, see text.

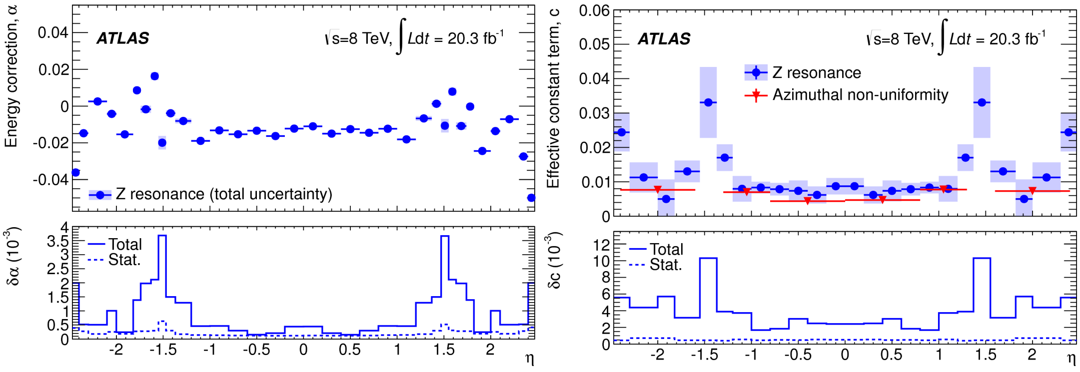

(a)

(b)

Figure 8.3: (a) Energy scale correction α diffference in data and Monte Carlo. The bottom plot shows the statistical and total energy scale uncertainties as a function of η (b) The constant c term measured in data and Monte Carlo. The bottom plot shows the statistical and systematic uncertainties on c. Taken from [60].

Using standard candles like $Z \to e^+e^-$ or $J/\psi \to e^+e^-$, the quantities α and c can be directly measured from the invariant mass distribution. Figure 8.3 shows the measured distributions of these two terms. Energy scale and energy resolution corrections thus obtained are applied to the electrons during analysis.

8.4 Electron Selection

Electron identification cuts applied for the selection of the Z-boson and $b\bar{b}$ event topologies are different. However some baseline electron cuts are similar for both cases. Electrons which happen to be in the transition region of the calorimeter $1.43 < |\eta| < 1.52$ are excluded since the electron identification performance is poor in this region. The electron candidates are required to be within the central barrel region of calorimeter ($|\eta| < 2.47$)

8.4.1 Isolated Electrons

Isolated high p_T electrons are identified using the *medium++* [61] operation point of the standard cuts menu. The invariant mass of the electron pairs thus identified are calculated using the energy deposited in the calorimeter and angular information from the Inner Detector. Only events with a Z-boson candidate invariant mass of $66 < m_Z < 120$ are accepted. Both electrons are required to have p_T higher than 20 GeV, for which the trigger is fully efficient. It is also required that both electrons have opposite charges.

Figure 8.4 shows the p_T, η, and φ distributions of the leading and sub leading electron candidates which pass the above selection cuts. It can bee seen that the Z+jets samples constitute a huge background for this analysis

The decay of Z-boson into electrons gives a clear signature of the event. The cuts that are applied are sufficient to remove all the non Z background. However Figure 8.5 shows that a small fraction of these backgrounds remain which are mainly composed of the following

- Events with W bosons decaying into electron and neutrino: $W \rightarrow e\nu$
- Events with top quark pairs, where one or both W bosons produced in the decay of the top quarks decay into electron and neutrino.
- Electrons coming from the decay of τ leptons which are resonantly produced through $Z \rightarrow \tau\tau$
- Diboson events, where electroweak gauge bosons are produced in pairs and decaying into electrons (WW, WZ, ZZ).

However the Z+jets and $Z + c\bar{c}$ backgrounds are irreducible with this method because their final states contain two electrons which come from Z-boson decays. The yield of signal $Z + b\bar{b}$ signal and different irreducible background components are shown in Table 8.2.

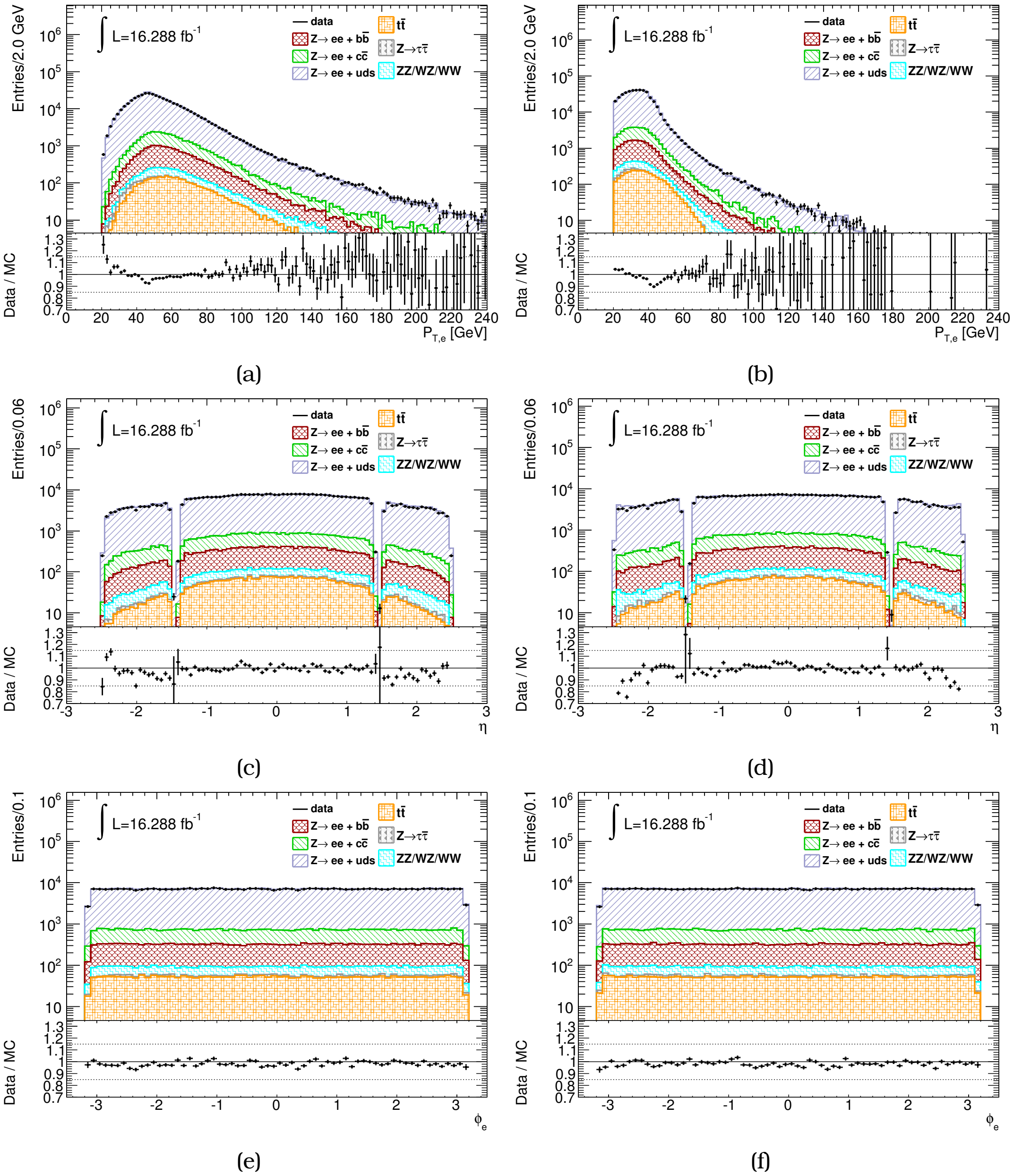

(a)

(b)

(c)

(d)

(e)

(f)

Figure 8.4: p_T, η and ϕ control distributions for electrons which pass *meidum*++ identification cuts. The plots on the right and left are the distributions for the leading p_T and the subleading p_T electron.

8.4.2 Soft Electrons

The Z-boson candidate event selection outlined in the previous section is dominated by $Z+$ light jets, $Z + b\bar{b}$ and $Z + c\bar{c}$ contributions. The B-mesons and D-mesons in the final states of $Z + b\bar{b}$ and $Z + c\bar{c}$ decay semileptonically into electrons and muons.

Type	Sample	Yield
Signal	$Z + b\bar{b}$	14538.95
Background	$Z + c\bar{c}$	25467.46
	$Z + uds$	402432.47
Total Background		448163.80

Table 8.2: Signal and background yield after Z-boson candidate selection.

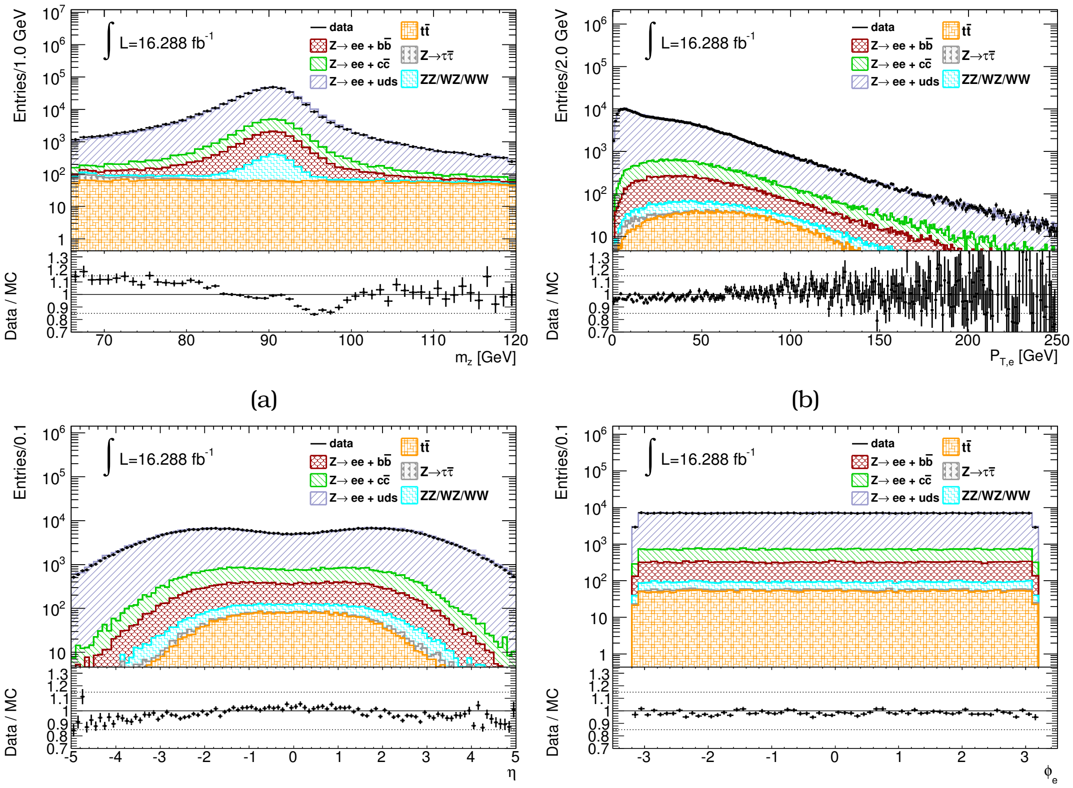

(a) (b)

(c) (d)

Figure 8.5: (a) Invariant mass (b) transverse momentum (c) pseudo rapidity and (d) φ distributions of Z-boson candidates showing the various backgrounds which are mainly composed of W boson decays, top quark decays, di-bosons and τ decays.

The soft electron selection cuts are optimized to identify the electrons coming from semileptonic decay of B-hadrons.

The non-Z electron candidates in the selected events are dominated by hadron fakes, photon conversions and electrons from in-flight decay of light hadrons. These backgrounds are reduced as much as possible before the soft electron tagger is applied. From Figure 8.6, it is clear that the kinematics of non-Z electrons are quite well described by Monte Carlo. Figure 8.6c shows the "conversion flag" distribution. Conversion flag value 2 indicates two leg photon conversion contamination (see chapter 6). Figure 8.6e shows the transverse impact parameter (d_0) distribution of the non-Z electrons. Here the Z + light jets sample shows a broader spectrum compared to the heavy flavor samples. Although electrons from semileptonic decays are not isolated as much as prompt electrons from W/Z decays, they are expected to be more isolated than collinear conversion electrons.

Figure 8.6f shows the distribution of the isolation variable $\mathrm{E}_T^{\mathrm{cone}}(20)/\mathrm{E}_T$ (see chapter 6). The $b\bar{b}$ signal is slightly enriched by rejecting electron candidates which are very close to jets. A cut value of $\mathrm{E}_T^{\mathrm{cone}}(20)/\mathrm{E}_T < 2$ is applied on the candidate electrons. This eliminates candidates which are wrongly reconstructed as electrons due to overlap with other particles in the calorimeter.

The photon conversion background is reduced by applying the following cuts:

- The transverse impact parameter value of candidate electrons is restricted to be less than 20 mm.

- Candidates which have conversion flag value 2 are rejected.

- Candidates without a b-layer hit are rejected.

These cuts reduce a significant fraction of electron fakes. For comparison the electron candidate multiplicity before and after applying the above discussed cuts are shown in Figure 8.7.The Soft electron tagger response distribution for the selected candidates are shown in Figure 8.7c.

An operating point corresponding to soft electron tagger response value of 0.1 is chosen. All di-electron combinations which survive the above cuts are further subjected to an invariant mass cut of 1.2 GeV to further suppress background from Dalitz decay and remaining photon conversion background. In addition track quality cuts are applied to further improve the purity of the electron selection. The complete list of cuts is given in Table 8.3.

Figure 8.8 shows distributions of invariant mass and angular separation and charge combinations of electron pairs. Low statistics and sizeable background makes the extraction of the hard scattering process $pp \rightarrow Z + b\bar{b}$ difficult. Even at the Monte Carlo level it is impossible to identify the b-electron which comes from the decay of the original b-quark produced in the hard scattering. The originating parton is not a well definied physical concept. During parton shower color connections arise between the "daughters" of hard b-quark. This would mean that there are graph reconnections between the daughters and the "tree picture" of the event becomes invalid [62].

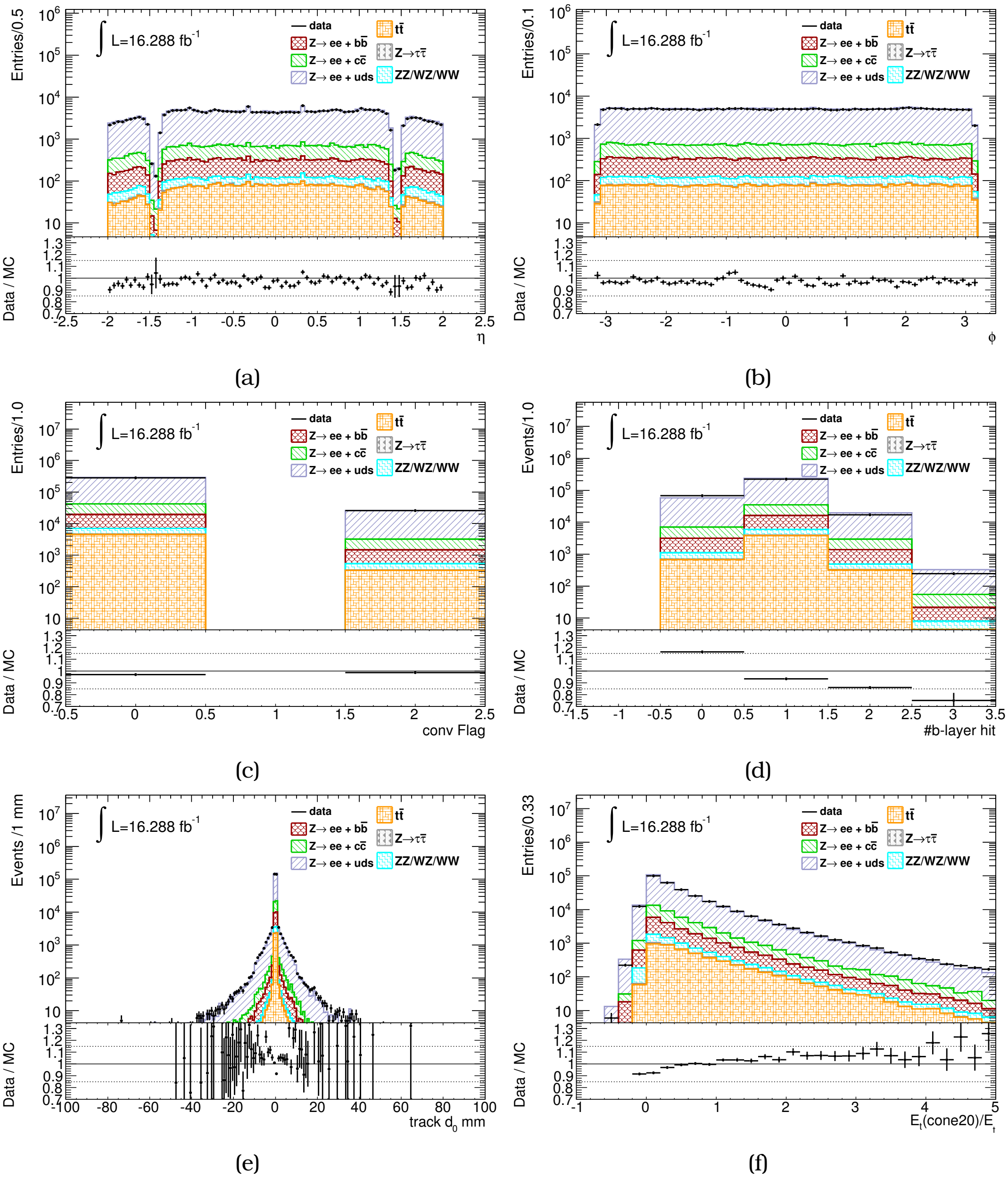

(a) (b)

(c) (d)

(e) (f)

Figure 8.6: (a) η and (b) ϕ as well as (c) conversion flag (d) number of b-layer hits (e) track impact parameter (f) Calorimeter isolation distributions of electron candidates in events which have a Z-boson candidate. The variables are plotted only for the non-Z electron candidates in the event.

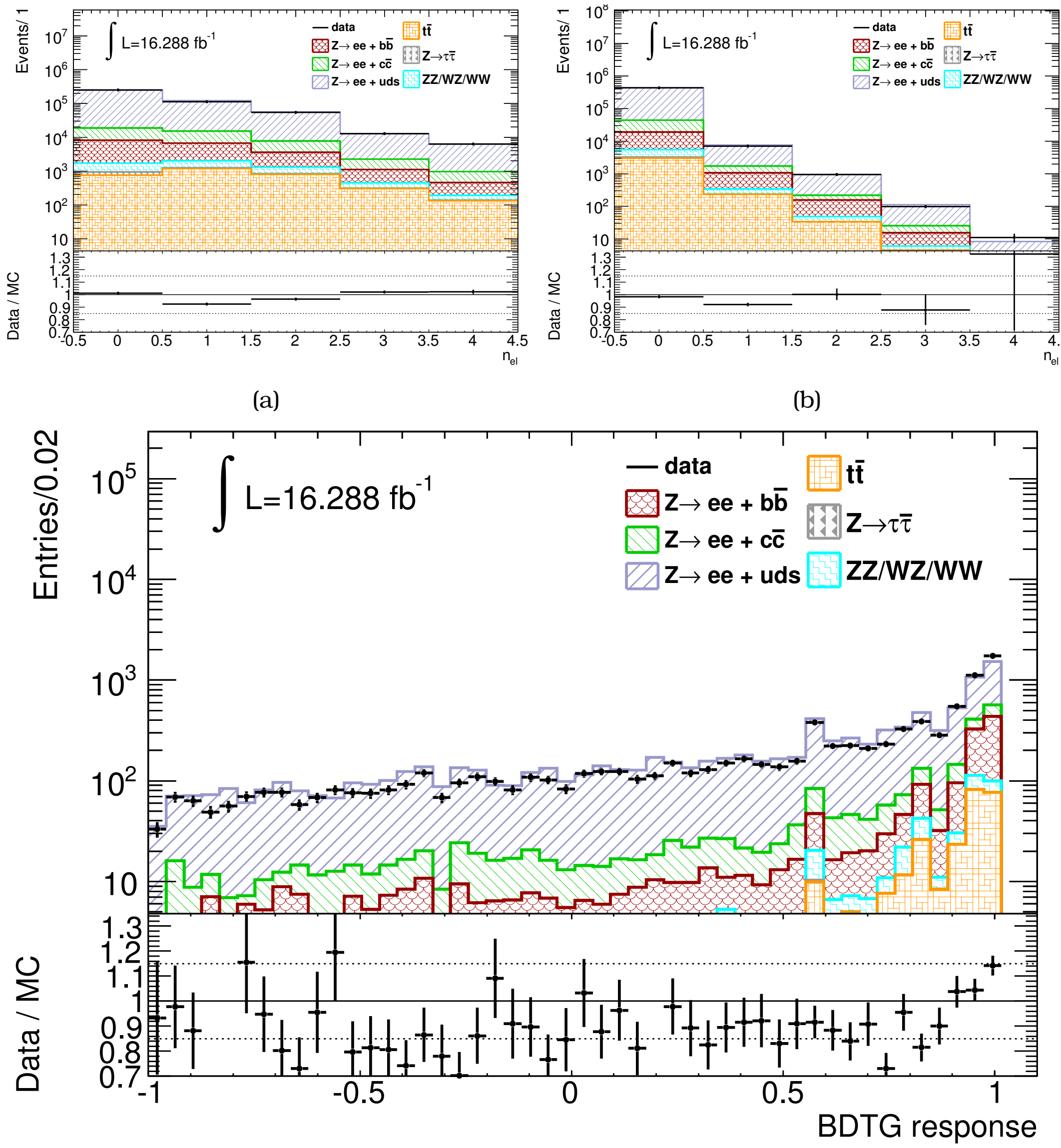

(a)

(b)

(c)

Figure 8.7: Multiplicity of electron candidates (a) before and (b) after preselection. (c) shows the soft electron response distribution.

8.5 Heavy Flavor Production at Hadron colliders

At hadron colliders heavy quarks like charm and beauty are produced by two mechanisms, the hard scattering and during parton shower. Monte Carlo studies have shown that the *Z*+ light jets process has a significant heavy flavor contribution.

In general the processes contributing to heavy quark production in hadronic collisions are the following [63]

Isolation cut	$E_T^{\text{cone}}(20)/E_T < 2$
Conversion rejection	# b-layer hits !=0 Conversion Flag = 0 track $d_0 < 20\,\text{mm}$
Track quality	$n_{\text{pixel hits}} >= 2$ $n_{\text{Silicon hits}} >= 7$ $\lvert\eta_{\text{trk}}\rvert < 2.0$
invariant mass cut	$m_{e1,e2} > 1.2\,\text{GeV}$

Table 8.3: Cuts applied on non-Z electron candidates to increase the purity of selected electrons.

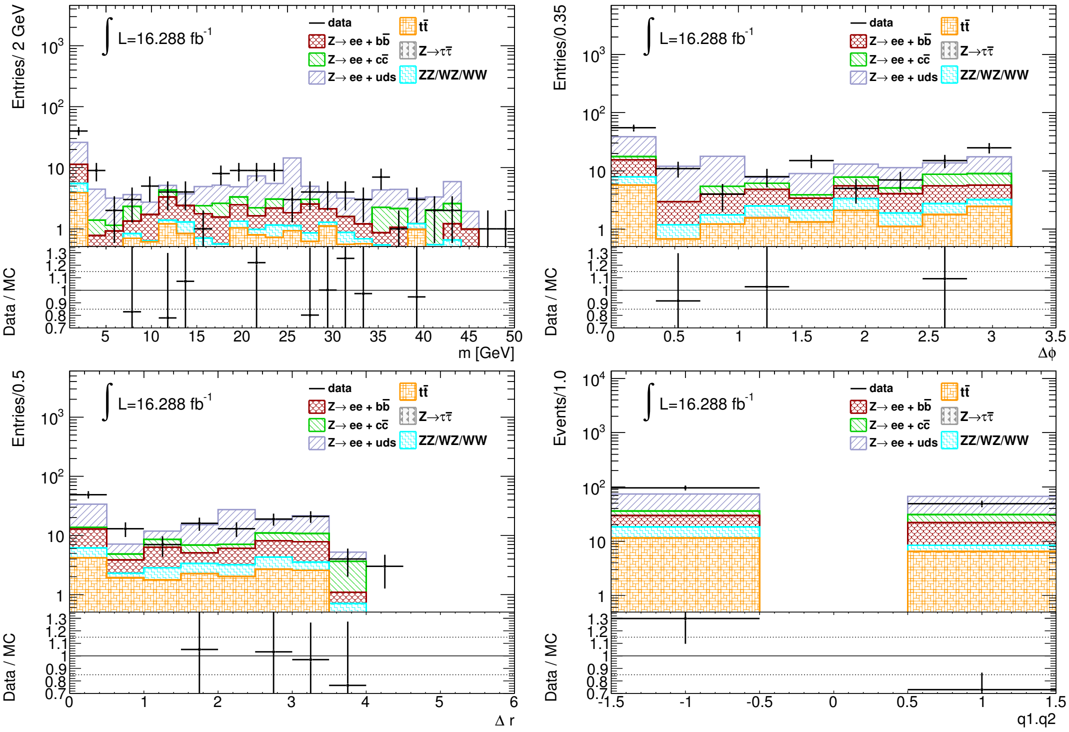

Figure 8.8: Charge combinations and angular separation distribution for non-Z electron candidates which pass a cut of 0.1 on soft electron response distribution.

Flavour creation: In this process, the heavy quark pair originates in the hard interaction from either quark-anti-quark annihilation or gluon-gluon fusion ($qq \to QQ$ or $gg \to QQ$). The process $Z + b\bar{b}$ at leading order is a pair creation process with one of the b-quark radiating a Z-boson.

Flavour excitation: The heavy quark comes from the sea of the initial state. One of the

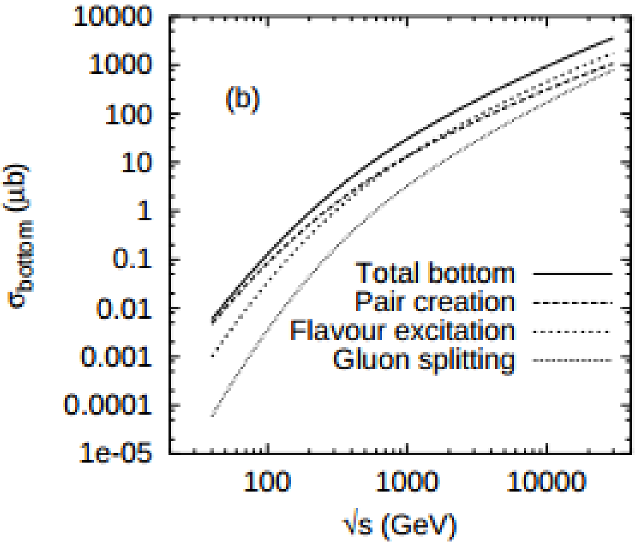

Figure 8.9: Total bottom cross section for *pp* collisions as a function of center of mass energy $\sqrt{s}$. The contribution from gluon splitting becomes substantial at the LHC energies [63].

excited heavy quarks interact with the parton from the other proton. $qQ \to qQ$ or $gQ \to gQ$. Leading order diagram contributing to the $Z + b$ production is flavor excitation process with a subsequent emission of Z-boson [64].

"gluon splitting": In this process heavy flavor quarks are produced through the process $g \to Q\bar{Q}$. It occurs in the initial state or final state radiation and none of the heavy flavor quarks undergo the hard scattering.

Figure 8.9 shows the perturbative QCD prediction for the total cross section of beauty production in proton-proton collisions as a function of center of mass energy. At lower energies flavor creation is the dominant process. Flavor excitation and "gluon splitting" becomes the dominant contribution to heavy flavor production at high energy collisions at LHC [65] in contrast to HERA [56]

8.6 Conclusion

Soft electron tagger along with sophisticated cuts on electron candidate distributions were studied to tag events with a Z-boson decaying into an electron positron pair in association with a $b\bar{b}$ pair decaying into another pair of electrons. After the Z-boson candidate selection, the $Z + b\bar{b}$ yield was 14538 events and the $Z+$ light jets yield was 402432 events in the selected invariant mass region corresponding to signal to background ratio (S/B) of 0.032. Using the soft-electron tagger along with sophisticated cuts to reduce photon conversions and hadron fakes, the S/B ratio

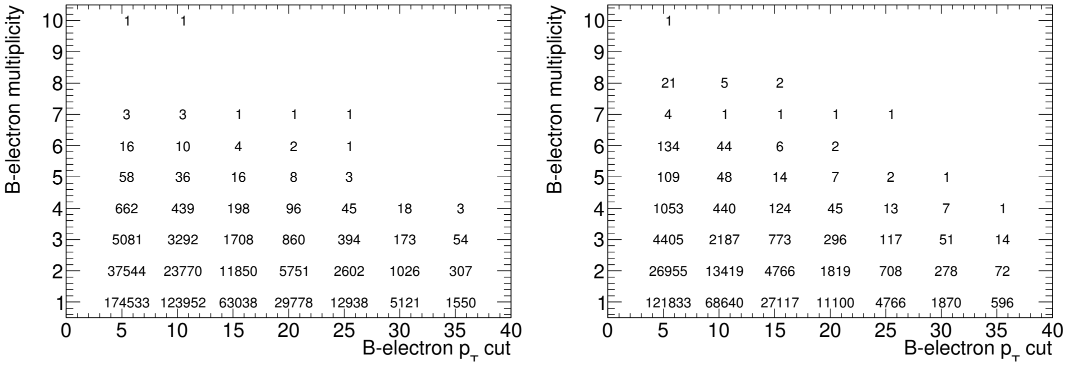

(a) Signal (b) Background

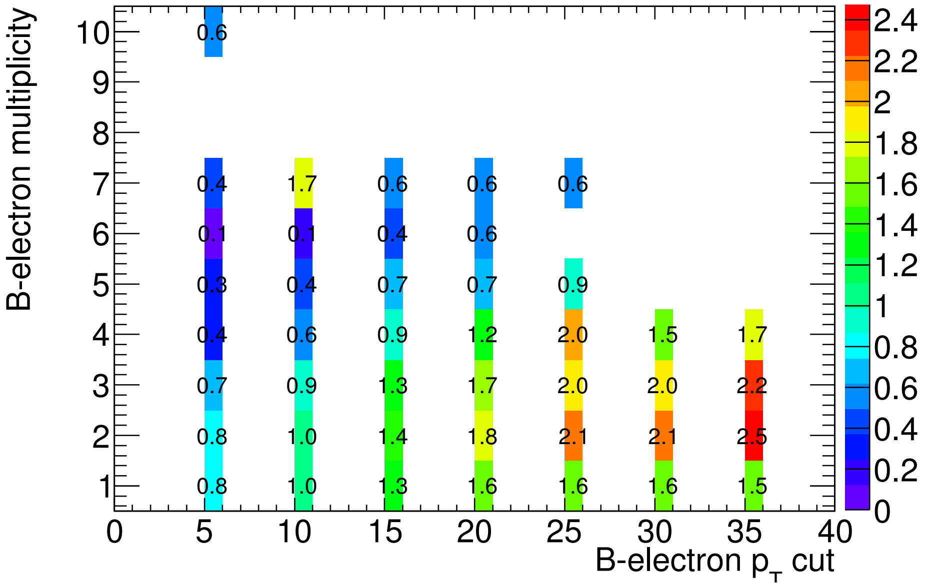

(c) Signal/Background

Figure 8.10: Truth Matched B-electron from (a) an exclusive signal sample ($Z \to e^+e^-$) + ($b\bar{b} \to e^+ + e^-$) and (b) Z+light jets background sample plotted as a function of the low p_T cut in respective multiplicity bins. The B-electron contribution from Z+ light jets sample is due to B-hadrons produced in parton shower. At low p_T such contaminations are present even in the $Z + b\bar{b}$ sample. (c) shows the ratio of normalized (a) and (b). The signal to noise ratio increases as we scan through the p_T cut bins.

was increased to 0.17. However the method is limited by B-electron contributions from Z+ light jets, $Z + c\bar{c}$ and $t\bar{t}$ background contributions. Monte Carlo studies were carried out using high statistics $Z(e^+e^-) + b\bar{b}(e^+e^-)$ exclusive sample to study if the process is ever measurable using the fully leptonic method.

Figure 8.10a and 8.10b shows B-electrons in bins of multiplicities and minimum

$\mathrm{p_T}$ cuts. As we scan from low $\mathrm{p_T}$ to high $\mathrm{p_T}$ cut bins, electrons which have soft B-hadron parents that are produced in parton shower are progressively removed and as result the number of electrons in high multiplicity bins also decreases. Figure 8.10c shows the normalized ratio of signal and background in multiplicity low $\mathrm{p_T}$ cut bins. The parton shower or “gluon splitting” component is progressively reduced in both the signal and background samples. What remains is B-electrons from the decay of the hard B-hadron. In the high-$\mathrm{p_T}$ cut bins, the S/B values are significantly increased and reach a value of 2.2 for a multiplicity of 2.

With currently available statistics, it is impossible to do a measurement with such high $\mathrm{p_T}$ electrons. However in future LHC runs, when more data becomes available, this method can potentially be used to measure the hard scattering process $pp \rightarrow Z + b\bar{b}$

Summary

Using the $\sqrt{S} = 7\,\mathrm{TeV}$ data recorded by ATLAS in 2011, a software was developed and tested for monitoring the timing stability of the Level-1 calorimeter trigger system. Any sudden or gradual monotonous shift in timing can be immediately observed and experts can intervene so that potential data loss is minimized. Analysis shows that the Level-calorimeter trigger had a stable operation during the physics runs in the year 2011, when the author carried out the analysis.

A soft electron tagger for identifying the semileptonic decay of heavy flavor hadrons has been developed and tested using $\sqrt{s} = 8\,\mathrm{TeV}$ data recorded by ATLAS in 2012. Signal and background electron identification variables were obtained from Monte Carlo simullations and verified using data. A multivariate boosted decision tree classifier, was trained using these samples to separate signal and background. The new tagger has been found to have 50% less background at the same efficiency compared to the *tight*++ standard electron cut menu operating point. The efficiency of the tagger has been verified in data using a J/ψ tag & probe method. The efficiency of the soft electron tagger has been found to be around 73% (which is comparable to the *tight*++ menu). The systematic uncertainty on soft electron identification has also been studied using the same J/ψ enriched data sample.

A feasibility study for the measurement of the associated production of a Z-boson in association with $b\bar{b}$ quarks using the new soft electron tagger has been carried out. Using the standard electron cuts menu, events with Z-bosons decaying into electron positron pairs have been selected. The signal could be further enriched by applying the soft electron identification on the additional electron candidates which are not associated to the Z-boson. Due to limited statistics and B-hadron background from "gluon splitting" processes, the signal could not be extracted. Monte Carlo studies show that with higher statistics at higher electron energies, the presented fully leptonic method to measure $pp \to Z + b\bar{b}$ process could work . With more data in the future LHC Run II, a measurement of this process might be possible.

Appendices

Soft electron variables

1 Signal and Background distributions of Electron identification Variables

The distributions of electro identification variables and various background contributing to the shape in Monte Carlo is shown in the following plots

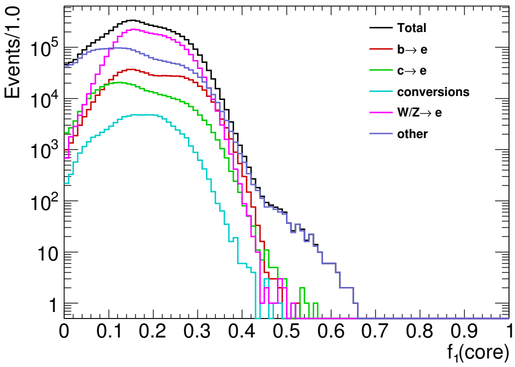

(a)

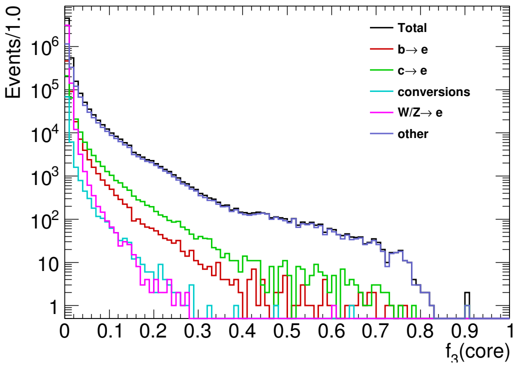

(b)

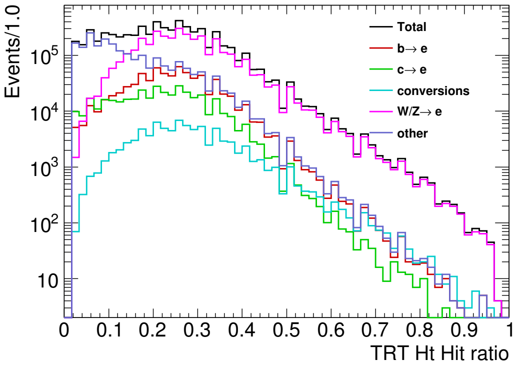

(c)

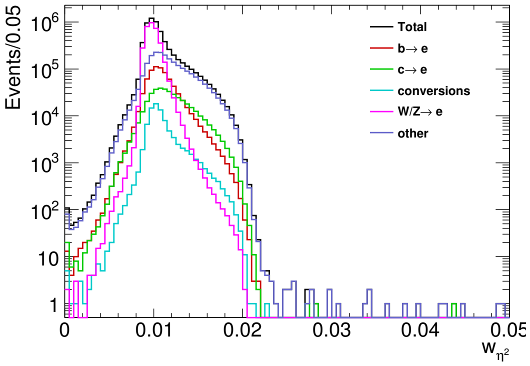

(d)

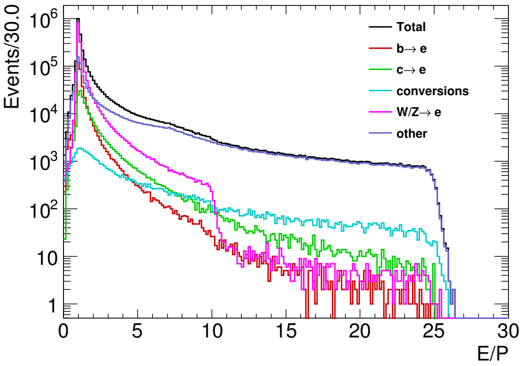
Events/30.0
10^6
10^5
10^4
10^3
10^2
10
1
0
5
10
15
20
25
30
E/P
Total
b→ e
c→ e
conversions
W/Z→ e
other

(a)

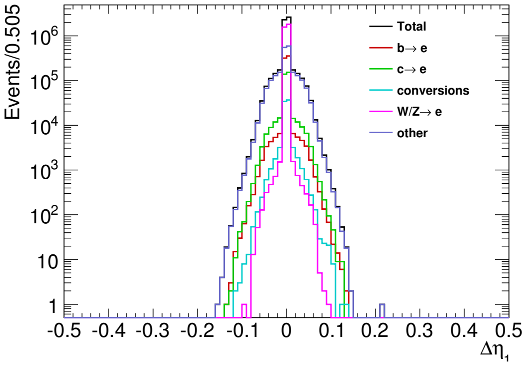
Events/0.505
10^6
10^5
10^4
10^3
10^2
10
1
-0.5
-0.4
-0.3
-0.2
-0.1
0
0.1
0.2
0.3
0.4
0.5
$\Delta\eta_1$
Total
b→ e
c→ e
conversions
W/Z→ e
other

(b)

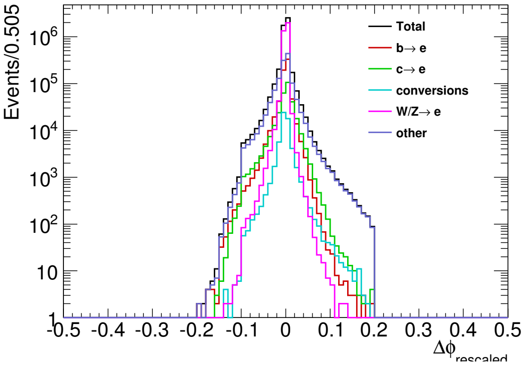
Events/0.505
10^6
10^5
10^4
10^3
10^2
10
1
-0.5
-0.4
-0.3
-0.2
-0.1
0
0.1
0.2
0.3
0.4
0.5
$\Delta\phi_{rescaled}$
Total
b→ e
c→ e
conversions
W/Z→ e
other

(a)

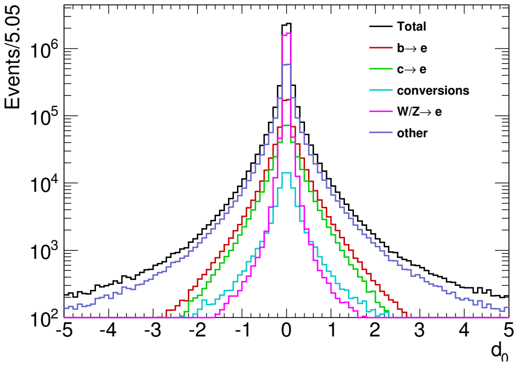
Events/5.05
10^6
10^5
10^4
10^3
10^2
-5
-4
-3
-2
-1
0
1
2
3
4
5
d_0
Total
b→ e
c→ e
conversions
W/Z→ e
other

(b)

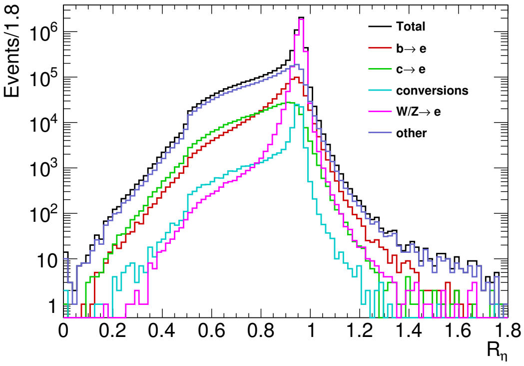
Events/1.8
10^6
10^5
10^4
10^3
10^2
10
1
0
0.2
0.4
0.6
0.8
1
1.2
1.4
1.6
1.8
R_η
Total
b→ e
c→ e
conversions
W/Z→ e
other

(c)

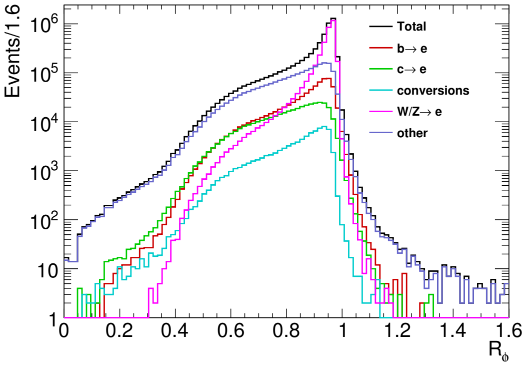
Events/1.6
10^6
10^5
10^4
10^3
10^2
10
1
0
0.2
0.4
0.6
0.8
1
1.2
1.4
1.6
R_ϕ
Total
b→ e
c→ e
conversions
W/Z→ e
other

(d)

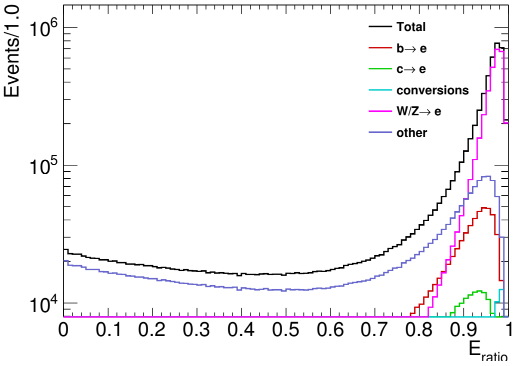
Events/1.0
10^6
10^5
10^4
0
0.1
0.2
0.3
0.4
0.5
0.6
0.7
0.8
0.9
1
E_{ratio}
Total
b→ e
c→ e
conversions
W/Z→ e
other

(e)

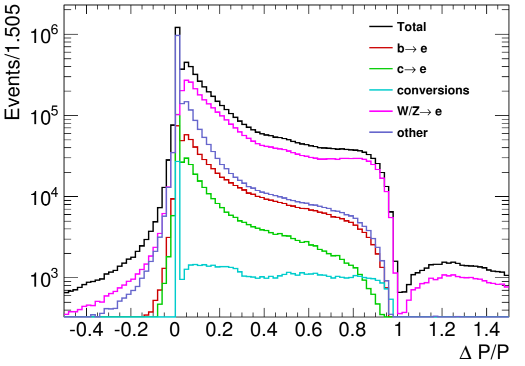
Events/1.505
10^6
10^5
10^4
10^3
-0.4
-0.2
0
0.2
0.4
0.6
0.8
1
1.2
1.4
Δ P/P
Total
b→ e
c→ e
conversions
W/Z→ e
other

(f)

2 Electron identification Variables Validated over Data

The electron identification variables for signal electrons which comes from B-hadron decays have been identified using Monte Carlo samples. These variables were validated over data using a J/ψ enriched data sample. In the following plots, all the variables which are validated over data using the sideband subtraction method is shown.

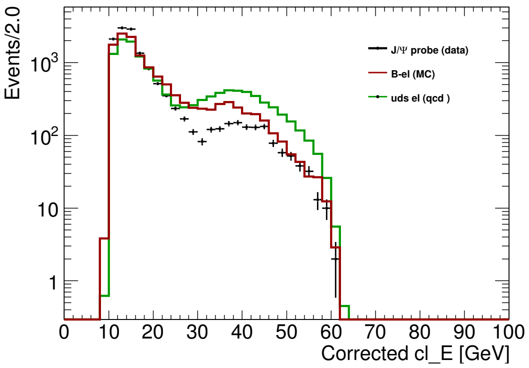

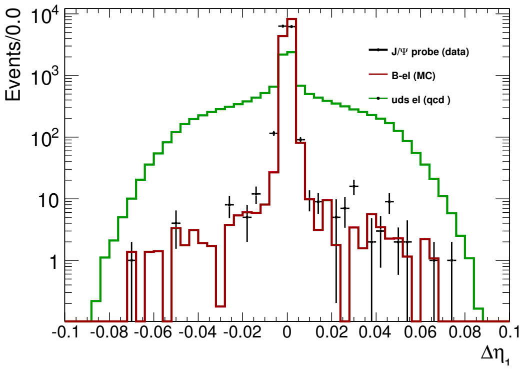

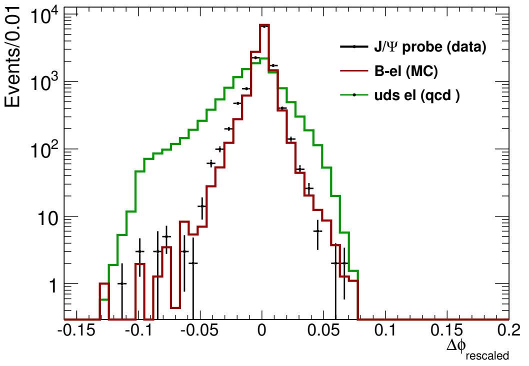

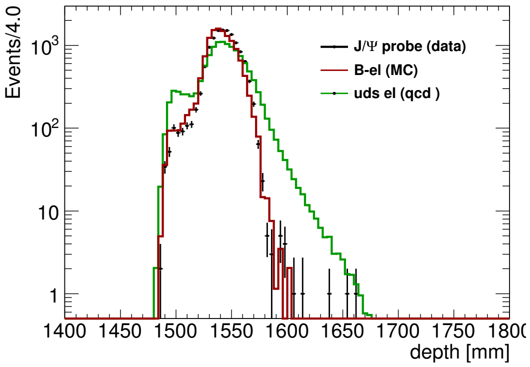

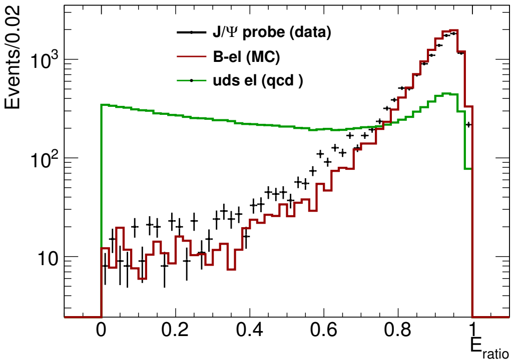

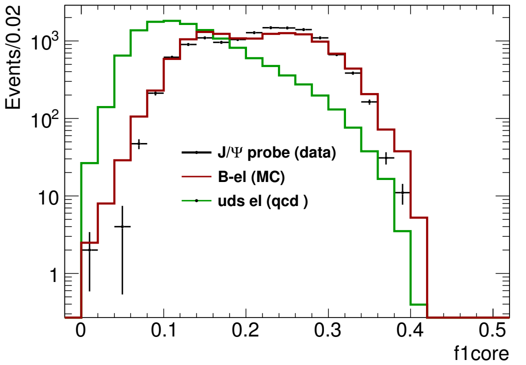

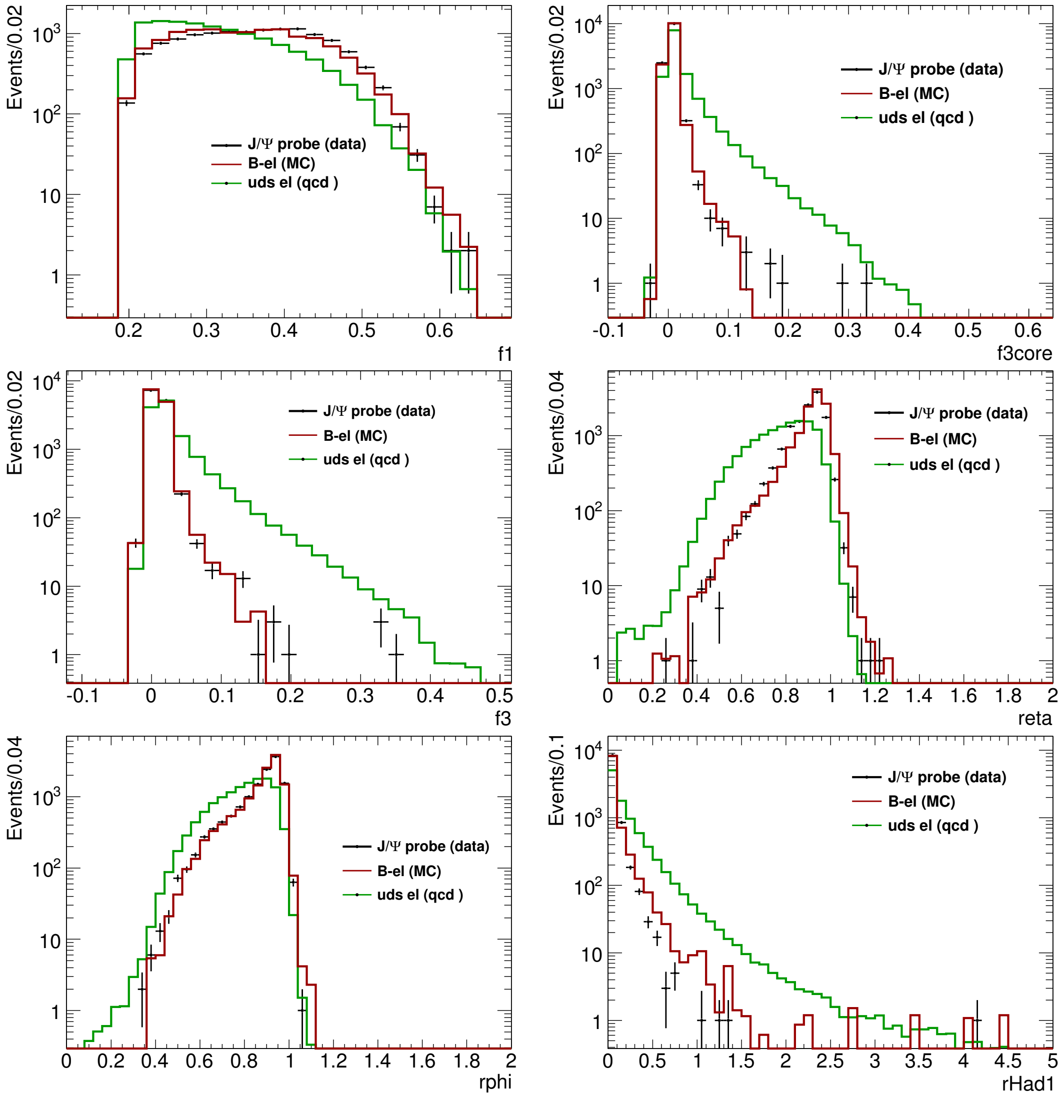
Events/0.02
f1
f3core
Events/0.02
f3
Events/0.04
reta
Events/0.04
rphi
Events/0.1
rHad1
J/Ψ probe (data)
B-el (MC)
uds el (qcd)

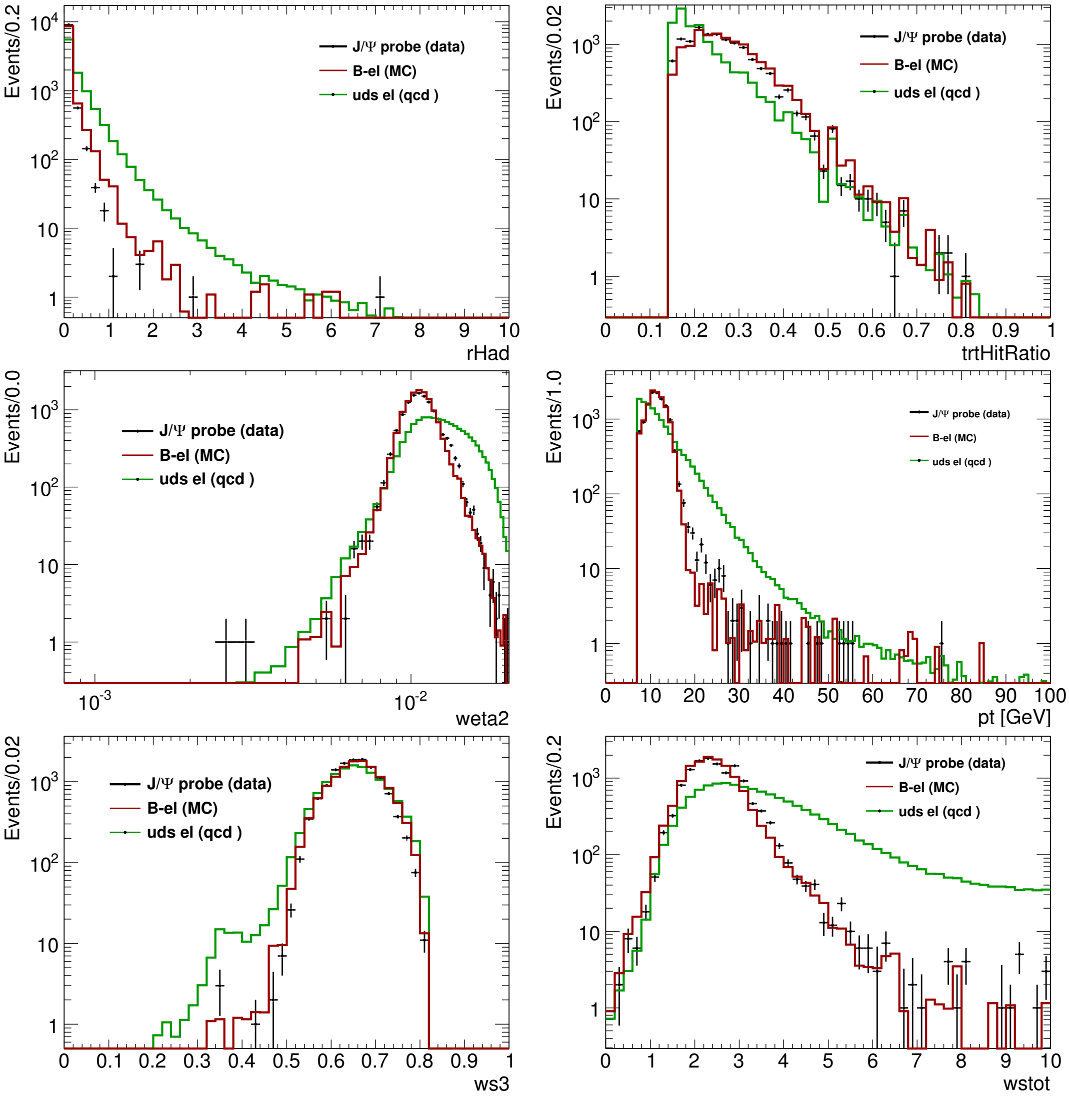
Events/0.2
rHad
J/Ψ probe (data)
B-el (MC)
uds el (qcd)
Events/0.02
trtHitRatio
Events/0.0
weta2
Events/1.0
pt [GeV]
Events/0.02
ws3
Events/0.2
wstot

3 Toy Monte Carlo study to verify the sideband substraction method

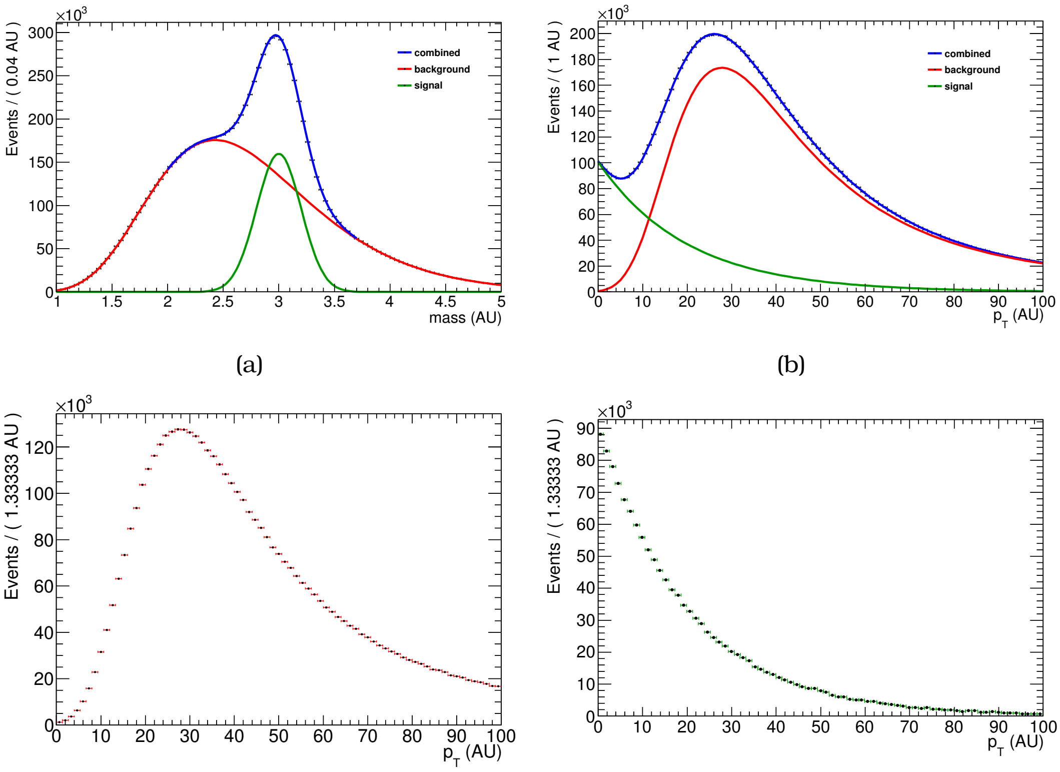

(a)

(b)

(c)

(d)

Figure 17: Results of a toy Monte Carlo to demonstrate the effectiveness of side-band method. In (a) the invariant mass distribution of a composite model is shown, figure (b) shows the transverse momentum distributions of the components. Figure (c) and (d) shows the extracted p_T distributions for signal and background respectively. It should be noted that the side-band subtraction method is able to effectively separate the two components

A toy Monte Carlo was written with composite invariant mass as well as p_T models. The invariant mass model is constructed as convolution of a Crystal Ball function and log-normal function. The p_T model is a convolution of an exponential function and a Landau function Figure 17a and 17b. Using the side-band subtraction method signal and background distributions of p_T were extracted. As it can be seen in Figure 17, the extracted distribution closely resembles the input model.

Bibliography

[1] K. S. Thorne, *John Archibald Wheeler (1911-2008)*, Science **320** no. 5883, (2008) 1603, `http://www.sciencemag.org/content/320/5883/1603.full.pdf`. `http://www.sciencemag.org/content/320/5883/1603.short`.

[2] S. L. Glashow, *Partial-symmetries of weak interactions*, Nuclear Physics **22** no. 4, (1961) 579 – 588. `http://www.sciencedirect.com/science/article/pii/0029558261904692`.

[3] S. Weinberg, *A Model of Leptons*, Phys. Rev. Lett. **19** (1967) 1264–1266. `http://link.aps.org/doi/10.1103/PhysRevLett.19.1264`.

[4] W. Commons, *Standard Model of Elementary Particles*, 2014. `http://commons.wikimedia.org/wiki/File:Standard_Model_of_Elementary_Particles.svg`.

[5] F. Halzen and A. Martin, *Quark & Leptons: An Introductory Course In Modern Particle Physics*. Wiley India Pvt. Limited, 2008. `http://books.google.de/books?id=ITQy9G62H0gC`.

[6] Gargamelle Collaboration, F. J. Hasert et al., *Observation of neutrino-like interactions without muon or electron in the Gargamelle neutrino experiment*, Phys. Lett. **B46** (1973) 138–140.

[7] S. Sherif. Personal communication.

[8] ATLAS Collaboration, *Measurements of Higgs boson production and couplings in diboson final states with the {ATLAS} detector at the {LHC}*, Physics Letters B **726** no. 1-3, (2013) 88 – 119. `http://www.sciencedirect.com/science/article/pii/S0370269313006369`.

[9] ATLAS Collaboration, G. Aad et al., *Observation of a new particle in the search for the Standard Model Higgs boson with the {ATLAS} detector at the {LHC}*, Physics Letters B **716** no. 1, (2012) 1 – 29. `http://www.sciencedirect.com/science/article/pii/S037026931200857X`.

[10] CMS Collaboration, S. Chatrchyan et al., *Observation of a new boson at a mass of 125 GeV with the {CMS} experiment at the {LHC}*, Physics Letters B **716**

no. 1, (2012) 30 – 61. `http://www.sciencedirect.com/science/article/pii/S0370269312008581`.

[11] ATLAS Collaboration Collaboration, G. Aad et al., *Measurement of the Higgs boson mass from the $H \rightarrow \gamma\gamma$ and $H \rightarrow ZZ^* \rightarrow 4\ell$ channels with the ATLAS detector using 25 fb^{-1} of pp collision data*, `arXiv:1406.3827 [hep-ex]`.

[12] ATLAS Collaboration, “Standard model results.” `https://twiki.cern.ch/twiki/bin/view/AtlasPublic/StandardModelPublicResults`.

[13] J. Barrow and D. Shaw, *The value of the cosmological constant*, General Relativity and Gravitation **43** no. 10, (2011) 2555–2560. `http://dx.doi.org/10.1007/s10714-011-1199-1`.

[14] ZEUS Collaboration, H1 Collaboration Collaboration, A. Cooper-Sarkar, *PDF Fits at HERA*, PoS **EPS-HEP2011** (2011) 320, `arXiv:1112.2107 [hep-ph]`.

[15] T. Ahmed et al., *A measurement of the proton structure function F2(x, Q2)*, Nuclear Physics B **439** no. 3, (1995) 471 – 502. `http://www.sciencedirect.com/science/article/pii/055032139598236U`.

[16] J. Campbell, R. K. Ellis, F. Maltoni, and S. Willenbrock, *Production of a Z boson and two jets with one heavy-quark tag*, Phys. Rev. D **73** (2006) 054007. `http://link.aps.org/doi/10.1103/PhysRevD.73.054007`.

[17] Particle Data Group Collaboration, J. Beringer et al., *Review of Particle Physics (RPP)*, Phys.Rev. **D86** (2012) 010001.

[18] LHC Study Group Collaboration, T. S. Pettersson and P. Lefévre, *The Large Hadron Collider: conceptual design*, Tech. Rep. CERN-AC-95-05 LHC, CERN, Geneva, Oct, 1995.

[19] ALICE Collaboration, K. Aamodt et al., *The ALICE experiment at the CERN LHC*, JINST **3** (2008) S08002.

[20] ATLAS Collaboration, G. Aad et al., *The ATLAS Experiment at the CERN Large Hadron Collider*, JINST **3** (2008) S08003.

[21] CMS Collaboration, S. Chatrchyan et al., *The CMS experiment at the CERN LHC*, JINST **3** (2008) S08004.

[22] LHCb Collaboration, J. Alves, A. Augusto et al., *The LHCb Detector at the LHC*, JINST **3** (2008) S08005.

[23] J.-L. Caron, “Overall view of LHC experiments.. Vue d’ensemble des experiences du LHC..” AC Collection. Legacy of AC. Pictures from 1992 to 2002., May, 1998.

[24] M. Bajko et al., *Report of the Task Force on the Incident of 19th September 2008 at the LHC*, Tech. Rep. LHC-PROJECT-Report-1168. CERN-LHC-PROJECT-Report-1168, CERN, Geneva, Mar, 2009.

[25] K. Desler and D. Edwards, *Accelerator physics of colliders*, The European Physical Journal C-Particles and Fields **15** no. 1, (2000) 157–159.

[26] *ATLAS Public Results*, 2014. `https://twiki.cern.ch/twiki/bin/view/AtlasPublic`.

[27] ATLAS Collaboration Collaboration, *ATLAS inner detector: Technical Design Report, 1.* Technical Design Report ATLAS. CERN, Geneva, 1997.

[28] ATLAS Collaboration Collaboration, N. Wermes and G. Hallewel, *ATLAS pixel detector: Technical Design Report.* Technical Design Report ATLAS. CERN, Geneva, 1998.

[29] A. Abdesselam, T. Akimoto, P. Allport, J. Alonso, B. Anderson, et al., *The barrel modules of the ATLAS semiconductor tracker*, Nucl.Instrum.Meth. **A568** (2006) 642–671.

[30] The ATLAS TRT Collaboration, *The ATLAS TRT Barrel Detector*, Journal of Instrumentation **3** no. 02, (2008) P02014. `http://stacks.iop.org/1748-0221/3/i=02/a=P02014`.

[31] ATLAS Collaboration, G. Aad et al., *Expected Performance of the ATLAS Experiment - Detector, Trigger and Physics*, `arXiv:0901.0512 [hep-ex]`.

[32] C. W. Fabjan and F. Gianotti, *Calorimetry for particle physics*, Rev. Mod. Phys. **75** (2003) 1243–1286. `http://link.aps.org/doi/10.1103/RevModPhys.75.1243`.

[33] K. Nakamura, P. D. Group, et al., *Review of particle physics*, Journal of Physics G: Nuclear and Particle Physics **37** no. 7A, (2010) 075021.

[34] ATLAS Collaboration, *ATLAS liquid argon calorimeter: Technical design report*, (1996).

[35] ATLAS Collaboration, *ATLAS muon spectrometer: Technical design report*, (1997).

[36] O. S. Bruning, P. Collier, P. Lebrun, S. Myers, R. Ostojic, J. Poole, and P. Proudlock, *LHC Design Report.* CERN, Geneva, 2004.

[37] R. Achenbach et al. Journal of Instrumentation **3** no. 03, (2008) P03001. `http://stacks.iop.org/1748-0221/3/i=03/a=P03001`.

[38] G. V. Andrei, *The data path of the ATLAS Level-1 calorimeter trigger preprocessor,*. `http://nbn-resolving.de/urn/resolver.pl?urn=urn:nbn:de:bsz:16-heidok-112215`.

[39] K. Ellis, *TRAPS, Topological Reconstruction Algorithm for Parton Scatters*, (2012).

[40] V. Lang and R. Stamen, *Precision Synchronization of the ATLAS Level-1 Calorimeter Trigger with Collision Data in 2010 and 2011*, Tech. Rep. ATL-DAQ-PUB-2012-001, CERN, Geneva, Jun, 2012.

[41] W. Lampl, S. Laplace, D. Lelas, P. Loch, H. Ma, et al., *Calorimeter clustering algorithms: Description and performance,*.

[42] *Electron efficiency measurements with the ATLAS detector using the 2012 LHC proton-proton collision data*, Tech. Rep. ATLAS-CONF-2014-032, CERN, Geneva, Jun, 2014.

[43] ATLAS Collaboration Collaboration, *Improved electron reconstruction in ATLAS using the Gaussian Sum Filter-based model for bremsstrahlung*, Tech. Rep. ATLAS-CONF-2012-047, CERN, Geneva, May, 2012.

[44] ATLAS Collaboration, G. Aad et al., *Electron performance measurements with the ATLAS detector using the 2010 LHC proton-proton collision data*, Eur.Phys.J. **C72** (2012) 1909, `arXiv:1110.3174 [hep-ex]`.

[45] T. A. T. collaboration and others", *The ATLAS Transition Radiation Tracker (TRT) proportional drift tube: design and performance*, Journal of Instrumentation **3** no. 02, (2008) P02013. `http://stacks.iop.org/1748-0221/3/i=02/a=P02013`.

[46] ATLAS Collaboration Collaboration, *ATLAS detector and physics performance: Technical Design Report, 1.* Technical Design Report ATLAS. CERN, Geneva, 1999. Electronic version not available.

[47] *Calibration of b-tagging using dileptonic top pair events in a combinatorial likelihood approach with the ATLAS experiment*, Tech. Rep. ATLAS-CONF-2014-004, CERN, Geneva, Feb, 2014.

[48] M. L. Mangano, M. Moretti, F. Piccinini, R. Pittau, and A. D. Polosa, *ALPGEN, a generator for hard multiparton processes in hadronic collisions*, JHEP **0307** (2003) 001, `arXiv:hep-ph/0206293 [hep-ph]`.

[49] T. SjÃűstrand, S. Mrenna, and P. Skands, *A brief introduction to {PYTHIA} 8.1*, Computer Physics Communications **178** no. 11, (2008) 852 – 867. `http://www.sciencedirect.com/science/article/pii/S0010465508000441`.

[50] S. Agostinelli et al., *Geant4 a simulation toolkit*, Nuclear Instruments and Methods in Physics Research Section A: Accelerators, Spectrometers, Detectors and Associated Equipment **506** no. 3, (2003) 250 – 303. `http://www.sciencedirect.com/science/article/pii/S0168900203013688`.

[51] *McTruthClassifier*, 2014. `https://twiki.cern.ch/twiki/bin/view/Main/MCTruthClassifierD3PD`.

[52] A. Hoecker, P. Speckmayer, J. Stelzer, J. Therhaag, E. von Toerne, and H. Voss, *TMVA: Toolkit for Multivariate Data Analysis*, PoS **ACAT** (2007) 040, `arXiv:physics/0703039`.

[53] B. P. Roe, H.-J. Yang, J. Zhu, Y. Liu, I. Stancu, and G. McGregor, *Boosted decision trees as an alternative to artificial neural networks for particle identification*, Nuclear Instruments and Methods in Physics Research Section A: Accelerators, Spectrometers, Detectors and Associated Equipment **543** no. 2âĂŞ3, (2005) 577 – 584. `http://www.sciencedirect.com/science/article/pii/S0168900205000355`.

[54] O. Behnke, K. Kröninger, G. Schott, and T. Schörner-Sadenius, *Data Analysis in High Energy Physics: A Practical Guide to Statistical Methods*. Wiley, 2013. `http://books.google.de/books?id=KZgSAAAAQBAJ`.

[55] CDF Collaboration Collaboration, D. Acosta et al., *Measurement of the J/ψ meson and b-hadron production cross sections in $p\overline{p}$ collisions at* $\sqrt{s} = 1960$ GeV, Phys. Rev. D **71** (2005) 032001. `http://link.aps.org/doi/10.1103/PhysRevD.71.032001`.

[56] F. Aaron et al., *Measurement of beauty photoproduction near threshold using di-electron events with the H1 detector at HERA*, The European Physical Journal C **72** no. 10, (2012). `http://dx.doi.org/10.1140/epjc/s10052-012-2148-1`.

[57] G. Aad and others., *The ATLAS Simulation Infrastructure*, The European Physical Journal C **70** no. 3, (2010) 823–874. `http://dx.doi.org/10.1140/epjc/s10052-010-1429-9`.

[58] ATLAS Collaboration, *Heavy Flavor Overlap Removal*, 2014. `https://twiki.cern.ch/twiki/bin/view/Main/HforToolD3PD`.

[59] Y. Levinsen, R. Appleby, and H. Burkhardt, *Beam gas loss rates in the LHC*, no. CERN-ATS-2010-060, (2010) 3 p.

[60] ATLAS Collaboration Collaboration, G. Aad et al., *Electron and photon energy calibration with the ATLAS detector using LHC Run 1 data*, `arXiv:1407.5063 [hep-ex]`.

[61] *Expected electron performance in the ATLAS experiment*, Tech. Rep. ATL-PHYS-PUB-2011-006, CERN, Geneva, Apr, 2011.

[62] B. Andy. Private communication.

[63] E. Norrbin and T. Sjöstrand, *Production and hadronization of heavy quarks*, The European Physical Journal C - Particles and Fields **17** no. 1, (2000) 137–161. `http://dx.doi.org/10.1007/s100520000460`.

[64] J. Campbell, R. K. Ellis, F. Maltoni, and S. Willenbrock, *Associated production of a Z boson and a single heavy-quark jet*, Phys. Rev. D **69** (2004) 074021. `http://link.aps.org/doi/10.1103/PhysRevD.69.074021`.

[65] T. Lagouri, *Study of b-bbar correlations with ATLAS at the LHC*, no. ATL-COM-PHYS-2004-063, (2004) 14 p.

Acknowledgement

I would like to express my gratitude to Prof. Dr. André Schöning, my thesis supervisor, for his patient guidance and support.

I am grateful to the fruitful discussions with Sebastian Schäetzel, Tatsiana Klimkovich during the some critial instances in the course of the thesis. I also thank Christoph Anders for patiently reading through the critical sections of my thesis and giving me suggestions to improve. I thank Prof. Dr. Hans-Christian Schultz-Coulon for acting as the second referee.

I am truly grateful to all my colleagues for the great time we had in Heidelberg. I say a big thank you in chronological order to Sebastian Schmitt, Gregor Kasieczka, David Sosa, Maddalena Giulini and Mathis Kolb.

During the first year of my thesis, I was working with the KIP ATLAS group as part of my service task. I thank Rainer Stamen and John Taylor Childers for helping me in developing the monitoring software. I also thank Yuriy Davygora and Florian Lepold who made my association with L1Calo quite memorable.

During this occasion I also remember my parents, my father Thampilali Narayanan and mother Shylaja Cheroth who couldn't be fortunate enough to see me finishing my thesis. I thank my sister Dwithi Surej for supporting me during the tough times.

Last but not the least, I thank you Deepa for all the love and support, emotionally and professionally which greatly helped and inspired me in both my professional and personal life.